

High-resolution multi-temporal analysis of geomorphic change on the
Sandy Pond spit, eastern shore of Lake Ontario, NY

Megan A. Kopp

A thesis

submitted to the faculty of the department of Earth and Environmental Sciences
in partial fulfillment of the requirements for the degree of
Master of Science

Boston College

Morrissey Graduate College of Arts and Sciences

December 2022

High-resolution multi-temporal analysis of geomorphic change on the Sandy Pond spit, eastern shore of Lake Ontario, NY

Megan A. Kopp

Advisor: Noah P. Snyder

Abstract

Multi-temporal elevation (MTE) analysis is used to study topographic changes at specific intervals. Barrier-island complexes are often studied using this MTE analysis to quantify changes to the environment after hurricanes to understand how dynamic landscapes respond to different forcings. The Sandy Pond spit (SPS) is a north-south trending barrier island on the eastern shore of Lake Ontario, New York, which responds dynamically to fluctuations in water levels, ice cover, and storms. Prior research reconstructed the geomorphic history of the SPS from 1878-2013, determining that the most significant factor affecting decadal change is the lake-water elevation. In the summers of 2017 and 2019, anomalously high precipitation and lake levels resulted in increased erosion along the SPS, and flooding in neighboring communities.

In this study I used shoreline position, foredune crest position and elevation and volume of deposition and erosion to determine the dominant force of geometric change on the SPS before, during and after the high water events in 2017 and 2019, using the study period 2001-2020. Lidar data and small uncrewed aerial system images are used to generate digital elevation models (DEMs) and DEMs of difference (DoDs) from surveys conducted in May 2001, July 2007, June 2011, October 2015, May 2018, September 2018, July 2020 and August 2020.

Results indicated water level was the most significant factor altering the topography of the SPS. Large storm events although erosive, were not as destructive to the shore environment as the long duration elevated summer water levels. From 2001-2015 the shoreline advanced an average of 0.25 m/year. From 2015-2018 and 2018-2020 the shoreline retreated 0.62 m/year, and 3.27 m/year respectively. The foredune position and elevation altered due to erosion of the dune toe caused by wave action and shoreline retreat from 2015-2020 compared to 2001-2015. To study volumetric changes, the SPS was split into seven ecogeomorphic zones that characterize the barrier-spit system at large. From 2007-2015 net deposition was recorded at five of the seven zones when applying a 95% confidence interval. The zones recording erosion were characterized by high dune complexes with sparse vegetation to anchor sand. From 2015-2018 net erosion was recorded in all seven zones, indicating water level had a statistically significant effect on the rate and volume of geomorphic change to this ecosystem.

Acknowledgements

To my advisor, Noah: Thank you for everything. Your unwavering support, enthusiasm and passion provided me with a challenging, and welcoming learning environment and master's experience. It never went unnoticed. Thank you for providing the opportunity to create and complete a self-directed thesis project during a global pandemic, with fieldwork and GIS components. Thank you for coaching me through each piece of the process. Words cannot express my gratitude for your time.

To Gail and Mark: Thank you for your interest and support in my work. Gail, thank you for sharing your interest in beaches, careful attention to detail, and inquisitive questions. I thoroughly enjoyed researching, learning and TAing with you. Mark, thank you for supporting the graduate student community and taking the time to participate on my committee. I always enjoyed our chats in room 320.

To the Surface Processes Lab Group: Thank you Sarah Johnathan, Xinyi Zeng, Aleks Ostojic, Audrey Turcotte, Ian Dulin, Maya Rich, Claire Hines, and Lisa Kumpf for providing guidance, friendship, and support throughout my graduate experience. Thank you also to the rest of the graduate student community for providing camaraderie and fun the last two years.

Thank you to the Geological Society of America (GSA) Graduate Student Research Grant, which supported field work in the summer of 2020 and provided me the opportunity to share my work at the 2020 national conference and the 2021 northeast section meeting. Thank you to the Boston College Morrisey Graduate School of Arts and Science for providing summer funding and the means to attend the 2019 national GSA meeting. Without your support, I would not have been able to provide myself with this enriching educational experience.

To my family: Thank you Dad, Mom, Casey, and Tyler for your steadfast care and love. I would not be here without you. Thank you for encouraging my excitement for geology and the many Best Days Ever throughout my time as a master's student. A special thanks to each of you for assisting me in the field in the summer of 2020 when most field work was suspended as well as my many cousins, aunts and uncles that joined in for drone flights and boat rides. Thank you, Eileen, Kevin, Caroline, Matt, Claire Bob, and Aileen Kopp and Ellie and Hannah Reck.

Table of Contents

<i>Abstract</i>	
<i>Acknowledgements</i>	<i>i</i>
<i>List of Figures</i>	<i>iv</i>
<i>List of Tables</i>	<i>viii</i>
<i>1. Introduction</i>	<i>1</i>
<i>1.1 Multi-temporal elevation analysis</i>	<i>1</i>
<i>1.2 Barrier islands</i>	<i>3</i>
<i>2. Background</i>	<i>6</i>
<i>2.1 Lake Ontario</i>	<i>6</i>
<i>2.2 Human Management</i>	<i>11</i>
<i>3. The Sandy Pond spit</i>	<i>12</i>
<i>3.1 Geomorphic Context</i>	<i>12</i>
<i>3.2 Previous Work</i>	<i>16</i>
<i>4. Motivation</i>	<i>17</i>
<i>5. Objectives and Hypotheses</i>	<i>19</i>
<i>6. Methods</i>	<i>22</i>
<i>6.1 Lidar datasets</i>	<i>22</i>
<i>6.2 Fieldwork</i>	<i>26</i>
<i>6.3 DEM generation: Lidar</i>	<i>30</i>
<i>6.4 DEM generation: Structure-from-Motion</i>	<i>32</i>
<i>6.5 DEM Error</i>	<i>33</i>
<i>6.6 DoD Computation and Error Analysis</i>	<i>35</i>
<i>6.7 Metrics</i>	<i>37</i>
<i>6.7.1 Shoreline position</i>	<i>37</i>
<i>6.7.2 Foredune crest position and elevation</i>	<i>39</i>
<i>6.7.3 Volume of erosion and deposition</i>	<i>42</i>
<i>7. Results</i>	<i>45</i>
<i>7.1 Shoreline analysis</i>	<i>45</i>
<i>7.2 Foredune crest position and elevation</i>	<i>51</i>

7.3 Volumetric change.....	58
7.3.1 Zone 1 North.....	63
7.3.2 Zone 1 South.....	65
7.3.3 Zone 2.....	67
7.3.4 Zone 3.....	67
7.3.5 Zone 4.....	71
7.3.6 Zone 5.....	71
7.3.7 Zone 6.....	74
7.3.8. Zone 7.....	74
8. Discussion.....	77
8.1 2001-2015: Pre-high-water event.....	77
8.2 2015-2018: Including summer 2017.....	80
8.3 2018-2020: Including summer 2019 and November 2019 storm.....	83
8.4 Hypothesis testing.....	84
8.5 Limitations.....	86
8.6 Implications for management of the SPS.....	87
9. Conclusion.....	88
References.....	91

List of Figures

Figure 1. The parts of a barrier island system. A) Annotated cross section of a barrier island complex (from Reinson, 1992); B) Cross section profile of a barrier island defining the boundaries of the shoreface, beach, foredune, and backbarrier zones.

Figure 2. Examples of barrier island systems situated on the passive eastern margin of the United States. A) Galveston, Texas; B) Gulf Islands National Seashore, Mississippi; C) Ocean City, Maryland; D) Fire Island National Seashore, New York (from Google Earth, 2022).

Figure 3. Map of Great Lakes watershed. Red dot indicates where the SPS is located, and the Moses Saunders Dam is highlighted yellow (Modified from Great Lakes, 2022).

Figure 4. Mean monthly water level of Lake Ontario from January 1860 to August 2021 recorded by Station OSGN6 9052030 in Oswego, NY. The Ordinary Mean High-Water (OMHW) lake level of 75.4 m is included for reference (NOAA, 2021a).

Figure 5. Lake level from January to December for all years included in the study (2001-2020). Exceptionally high water summers are colored red (2017 and 2019). The Ordinary mean high water (OMHW) level is included for reference. Data were collected from the NOAA buoy Station OSGN6 9052030 in Oswego, NY located at the red diamond. The black pin shows the location of the study site (NOAA, 2021a).

Figure 6. Time series of significant wave heights recorded an offshore buoy (Station 45135 – Prince Edward Point; marked by the yellow diamond) located in the eastern part of the basin (see inset). Wave height is recorded from the spring through fall seasons. The buoy is removed in the beginning of the winter and thus no data are collected during this season. The black marker is the location of the SPS (NOAA, 2021b).

Figure 7. Annotated satellite image of the Sandy Pond spit (inset: Lake Ontario) (from Google Earth, 2022).

Figure 8. Geomorphic evolution of the SPS from 1878-2006. “R” refers to the formation of recurved ridges surrounding the inlet, and “Fan” refers to the subaqueous fans developing as a result of inlet formation (from Mattheus et al., 2016).

Figure 9. Photographic evidence of destruction caused by the high-water summers in the region surrounding the SPS. a-c): shoreline erosion on the SPS (from personal collection); d-e): flooded yards and sandbag walls placed in Hamlin, NY near Sandy Pond from the 2019 high water summer (Democrat and Chronicle, 2019); f) flooding from the 2017 high water summer isolating homes (Brederland, 2017).

Figure 10. Illustration demonstrating how point density effects DEM resolution. When there are fewer points in the dataset, there it is more likely that some cells of the grid will

be empty, without data, the higher the point density is, the more likely it is a data point is within the grid cell of the DEM. If one data point lies within a cell, the cell value will equal that of the data point. If there are multiple datapoints within a cell, the cell will be assigned a value equal to the average of that of the data points which fall in the cell.

Figure 11. Map and description of the seven ecogeomorphic zones identified for sUAS data collection and analysis.

Figure 12. Map of checkpoints used for lidar interpolation error.

Figure 13. Extent of lidar coverage for all study datasets. a) 2001; b) 2007; c) 2011; d) 2015; e) May 2018; f) September 2018. The base map is a 2016 aerial image.

Figure 14. DEM generation workflow for lidar and SfM data. a) Lidar DEM workflow; steps highlighted in yellow were only used for high resolution point cloud data from the 2015 and 2018 surveys. b) SfM DEM generation workflow.

Figure 15. Summary of the components of the DSAS analysis.

Figure 16. Summary of the foredune crest identification procedure. a) slope map with inset describing the location of the foredune; b) Hillshade and DEM with inset of the foredune crest location; c) aerial photograph showing vegetation line.

Figure 17. Example of identified foredune crests in Zone 5 from 2007-2020.

Figure 18. Extent of DoDs used to determine the region used for volume calculation of each individual zone. The pre-high water DoD coverage heavily impacted the area included in volumetric analysis depending on coverage. Coverage from the more recent DoD is much higher at Zone 1 South (left) while there is little difference in the coverage of the two DoDs at Zone 4 (right).

Figure 19. DSAS results for the rate of shoreline change (RSC) during the 2001-2015, 2015-2018, and 2018-2020 intervals.

Figure 20. Summary of alongshore DSAS analysis results. Positive change indicates deposition, and negative, erosion. The inlet region, shaded gray, represents transects surrounding the channel.

Figure 21. Illustration of scenario 1 (S1) showing a decrease in elevation and landward movement of the foredune.

Figure 22. Illustration of scenario 2 (S2) showing a decrease in the elevation and lakeward movement of the foredune.

Figure 23a-h. Cross-barrier topographic profiles of the barrier at each zone for each dataset within the study period. One representative transect is used to represent each of the eight flight zones. Continues on the next two pages (a-h). The monthly high water

levels for the summer of 2017, 2019, and the OMHW elevation are provided for reference and to demonstrate the effect of water level on the beach profile.

Figure 24. Alongshore horizontal and vertical migration of the foredune crest plotted with the rate of shoreline change (RSC) calculated during DSAS analysis during the 2007-2015, 2015-2018, and 2018-2020 intervals. The inlet region is shaded in grey. Zero change is displayed as a reference. More variation in the foredune position is measured from 2015-2018 compared to 2007-2015.

Figure 25. August 2020 orthophotograph of Zone 2 showing over wash fans. The 2020 and 2018 OMHW shorelines are shown in orange and red, respectively.

Figure 26. Zone 1 North 2011-2015 and 2015-2018 DoDs with volumetric change calculations. Volumetric change with in the LOD_{min} is shaded grey and is not statistically significant. Histograms show the volume of change measured and the associated error.

Figure 27. Zone 1 South 2011-2015 and 2015-2018 DoDs with volumetric change calculations. Volumetric change with in the LOD_{min} is shaded grey and is not statistically significant. Histograms show the volume of change measured and the associated error.

Figure 28. Zone 2 2007-2015 and 2015-2018 DoDs with volumetric change calculations. Volumetric change with in the LOD_{min} is shaded grey and is not statistically significant. Histograms show the volume of change measured and the associated error.

Figure 29. Zone 3 2007-2015 and 2015-2018 DoDs with volumetric change calculations. Volumetric change with in the LOD_{min} is shaded grey and is not statistically significant. Histograms show the volume of change measured and the associated error.

Figure 30. Zone 4 2007-2015 and 2015-2018 DoDs with volumetric change calculations. Volumetric change with in the LOD_{min} is shaded grey and is not statistically significant. Histograms show the volume of change measured and the associated error.

Figure 31. Zone 5 2007-2015 and 2015-2018 DoDs with volumetric change calculations. Volumetric change with in the LOD_{min} is shaded grey and is not statistically significant. Histograms show the volume of change measured and the associated error.

Figure 32. Zone 6 2007-2015 and 2015-2018 DoDs with volumetric change calculations. Volumetric change with in the LOD_{min} is shaded grey and is not statistically significant. Histograms show the volume of change measured and the associated error.

Figure 33. Zone 7 2011-2015 and 2015-2018 DoDs with volumetric change calculations. Volumetric change with in the LOD_{min} is shaded grey and is not statistically significant. Histograms show the volume of change measured and the associated error.

Figure 34. 2007-2015 raw and thresholded DoD across the whole study area.

Figure 35. Schematic of typical swell and storm beach profiles (modified from Friends of IBSP, 2022).

Figure 36. 2015-2018 raw and thresholded volumetric change across the whole study area.

List of Tables

Table 1. Ten highest significant wave heights recorded by Station OSGN6 9052030 in the eastern basin of Lake Ontario (NOAA, 2021b).

Table 2. Minimum and maximum lake levels for Lake Ontario permitted under Plan 2014 (IJC, 2014).

Table 3. Synopsis of dredging history during study period (Hart and Steadman, 2017; SPCMA, 2022).

Table 4. List of hypotheses and their respective tests.

Table 5. Summary table of lidar datasets available from NOAA data access viewer (NOAA, 2020). Point density is calculated over the entire survey area. (Abbreviations: USACE: United States Army Corps of Engineers; JALBTCX: Joint Bathymetry Technical Center of Expertise; SHOALS: Scanning Hydrographic Operational Airborne Lidar Survey; NCMP: National Coastal Mapping Program; CHARTS: Compact Hydrographic Airborne Rapid Total Survey; ACA: Aerial Cartographics of America; FEMA: Federal Emergency Management Agency; NYS OITS: New York State Office of Information Technology Services).

Table 6. Procedure for sUAS field surveys.

Table 7. Summary of error calculations for Lidar and SfM derived DEMs. The term n refers to the number of RTK GPS measurements used to determine the accuracy of the interpolated DEM.

Table 8. Summary of DoDs generated from lidar data and their corresponding resolution and error.

Table 9. Summary of the average rate of shoreline including (net) and omitting (adjusted) the inlet region. The uncertainty calculation used a 95% confidence interval.

Table 10. Summary of DSAS analysis results describing shoreline migration. Three statistics are included in DSAS summary reports: shoreline change envelope (SCE), net shoreline movement (NSM), and end point rate (EPR) (Himmelstoss et al., 2018). SCE refers to the net change in the shoreline distance at a transect regardless of time and direction. NSM is the net shoreline movement between the earliest shoreline and the most recent shoreline. EPR uses the NSM and computes a rate in m/year to describe the rate at which the shoreline is moving. Three shorelines are used in the analysis below: 2001, 2015, and September 2018.

Table 11. Summary of DSAS analysis results describing lateral foredune crest migration. Three statistics are included in DSAS summary reports: horizontal foredune change

envelope (FCE), net foredune horizontal movement (NFM), and rate of foredune horizontal migration (RFM) (Himmelstoss et al., 2018). FCE refers to the net change in the horizontal position of the foredune crest. NFM is the net foredune crest movement between the earliest and the most recent foredune crest position in the studied interval. RFM uses the NFM and computes a rate in m/year to describe the rate the foredune crest has moved.

Table 12. Summary of volumetric changes measured by DoDs at each zone including deposition, erosion and net change. Thresholded volume measurements use a 95% confidence interval to isolate significant change.

1. Introduction

1.1 Multi-temporal elevation analysis. Multi-temporal elevation (MTE) analysis is regularly used in geomorphic studies to quantify changes in topography over a series of intervals (Lentz and Hapke, 2011). The first MTE studies relied on laborious ground-based surveys resulting in sparse datasets, often ineffective at recognizing changes over large areas (Thom and Hall, 1991). In the 1970s, with the advent of lidar and global positioning system (GPS) technology, automated air-based data acquisition replaced manual-ground data collection, providing more complete, accurate datasets for MTE analysis (Brock and Purkis, 2009). Since then, lidar and GPS technology have continued to advance, resulting in increasingly dense, high-resolution datasets allowing opportunity to understand how landscapes respond to forcings over time.

Roughly 40 years after the development of lidar, Structure-from-Motion (SfM) photogrammetry was developed and used for MTE analysis, as a cheaper, more accessible alternative to lidar (Westoby et al., 2012). SfM is most ideal for low-budget operations in remote places, over small swaths of land. Because SfM data are collected by small uncrewed aerial systems (sUAS) or other consumer grade cameras, it is often used to measure landscapes immediately after change has occurred. SfM data additionally may be used in conjunction with lidar data to analyze additional intervals (Sherwood et al., 2018).

MTE analysis uses a sequence of digital elevation models (DEMs) to identify and quantify two and three-dimensional patterns of change over time. Researchers use MTE

surveys study dynamic landscapes experiencing change on short timescales. Previous studies use repeat elevation surveys to quantify metrics of change regarding mass movements and geohazards, glacial geomorphology, seismology and surface deformation, volcanology, and coastal systems (Williams, 2012).

MTE analysis was previously used in coastal settings to study: the impact of hurricanes (Zhang et al., 2005; Sherwood et al., 2018); the effect of humans and human made structures (Lentz and Hapke, 2011); eustatic sea level rise (Houser et al., 2018); inlet migration (Zainescu et al., 2019); barrier island transgression (Johnson et al., 2019) and more. Metrics of change quantified to describe such processes include: shoreline position (Zhang et al., 2005; Houser et al., 2008; Le Mauff et al., 2018); dune crest position and elevation (Johnson et al., 2019); volume of subaqueous and subaerial erosion and deposition (Eisemann et al., 2018; Nagarajan et al., 2019); beach width, and foredune slope (Lentz and Hapke, 2011). By measuring geomorphic processes, it is possible to identify and understand the effect of driving forces in order to prepare for and mitigate against natural disasters.

1.2 *Barrier islands*. Barrier island systems are one of the most dynamic coastal environments on Earth, producing measurable changes over periods of days, months, and

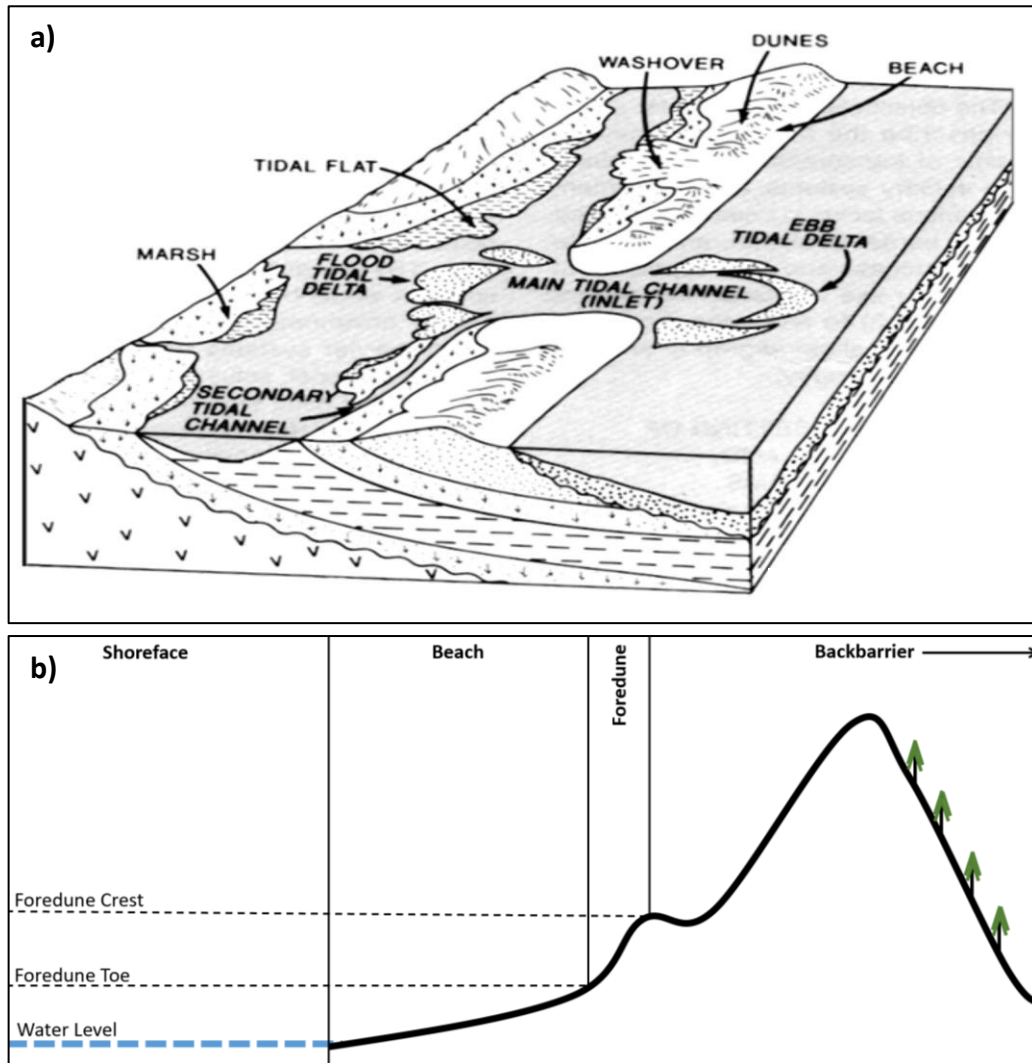


Figure 1. The parts of a barrier island system. A) Annotated cross section of a barrier island complex (from Reinson, 1992); B) Cross section profile of a barrier island defining the boundaries of the shoreface, beach, foredune, and backbarrier zones.

years and are thus ideal locations for MTE analysis (Ritter et al., 1978; Barrineau et al., 2015). Barrier islands are narrow bodies of sand parallel to the shoreline, situated between a landward lagoon or bay and the ocean (Fig. 1). Barriers are predominately

located on the coast of passive margins, formed from terrestrial deltas and oceanic bars deposited during a period of significantly lower eustatic sea level. As sea level rises, bars and deposits accumulate into subaerial islands of sand as a result of wind and longshore transport in a low energy setting (Ritter et al., 1978). Examples of barrier islands include Galveston, Texas; Ocean City, Maryland; Gulf Islands National Seashore, Mississippi; and Fire Island National Seashore, New York (Fig. 2).

Defining features of a barrier island include the beach, dunes, washover fans, back-barrier marshes, channel inlets, and vegetated low-lying forests (Fig. 1). Each feature functions differently to ensure the long-term stability and resilience of the island. For example, marsh, high dunes, and vegetation protect from flooding and transgression by trapping sediment in place. In contrast, dune blowouts allow increased erosion and channels for overwash of the barrier system (Davis Jr., 1983). Changes on barrier islands are naturally driven by sea level rise, storm surges, and sediment availability (Johnson et al., 2019). Fluctuations in these forcings cause measurable changes used to assess the necessity of anthropogenic intervention and human risk.

Lacustrine barrier systems offer a unique opportunity to study these dynamic features without the influence of tides. The major hydrologic forcings acting on a lacustrine barrier system are changes in water level, storm surges, and winter ice cover (Mattheus et al., 2016). Water level, when higher than normal, allows processes such as waves to act farther landward on the beach and can enhance undercutting or dune collapse due to saturation. The following studies the geomorphic effects of high-water events on the Sandy Pond spit (SPS), a barrier-spit on the eastern shore of Lake Ontario (LO).



Figure 2. Examples of barrier island systems situated on the passive eastern margin of the United States. A) Galveston, Texas; B) Gulf Islands National Seashore, Mississippi; C) Ocean City, Maryland; D) Fire Island National Seashore, New York (from Google Earth, 2022).

2. Background

2.1 Lake Ontario. LO has the smallest surface area of the Great Lakes and is situated farthest to the east, bordering New York and Ontario (Fig. 3). It sits at the lowest base level of the Great Lakes, which are connected by a series of locks and dams encompassing a 246,463 km² watershed (Fig. 3; Great Lakes, 2022). The combination of small surface area, low base level, and extensive watershed leaves LO and its shoreline hyper-sensitive to fluctuations in lake elevation which vary over annual, seasonal, and episodic (storms) periods (Fig. 4).



Figure 3. Map of Great Lakes watershed. Red dot indicates where the SPS is located, and the Moses Saunders Dam is highlighted yellow (Modified from Great Lakes, 2022).

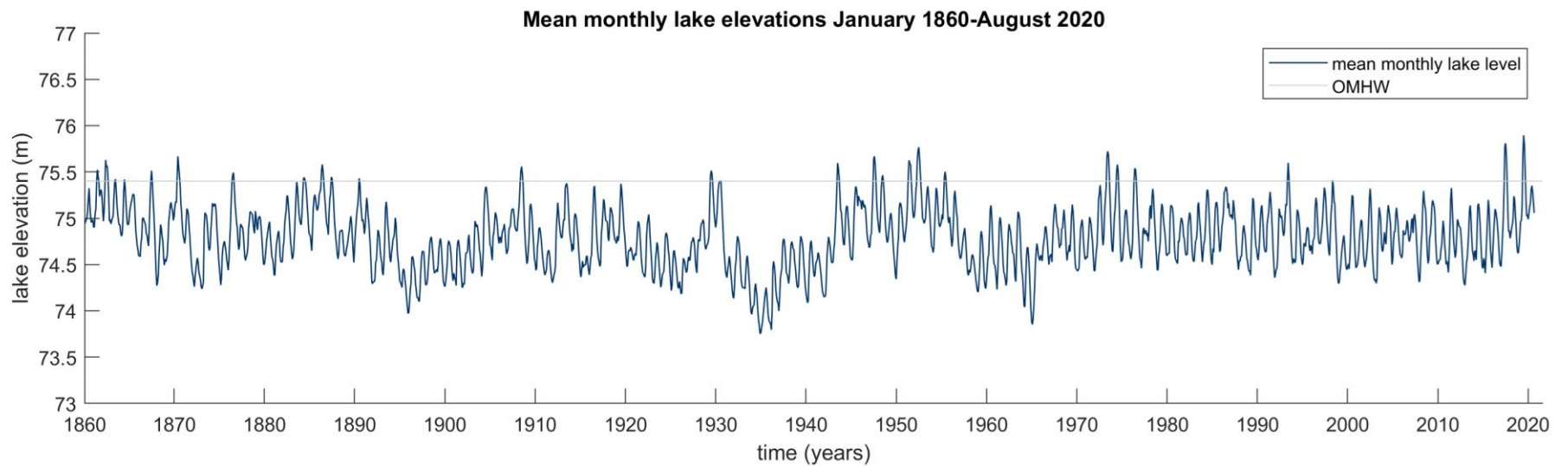


Figure 4. Mean monthly water level of Lake Ontario from January 1860 to August 2021 recorded by Station OSGN6 9052030 in Oswego, NY. The Ordinary Mean High-Water (OMHW) lake level of 75.4 m is included for reference (NOAA, 2021a).

Typically, the maximum lake elevation occurs between May 20 and June 15 as winter and spring runoff drains into the basin (Fig. 5; Mattheus et al., 2016). A typical summer peak water level, calculated by the average June monthly water level from 1918-2020, is 75.01 m (NOAA, 2021b). From peak water level to the end of the summer, the surface water may drop as much as 0.85 m (NOAA, 2020b). The fall season is most variable, and the lowest level typically occurs in November-January as snowpack and ice begin to develop on the margin of the lake. The monthly mean lake level in December from 1918-2020 was 74.53 m resulting in a 0.48 m decrease in lake level from June to December on average (NOAA, 2021b). LO rarely completely freezes over in the winter.

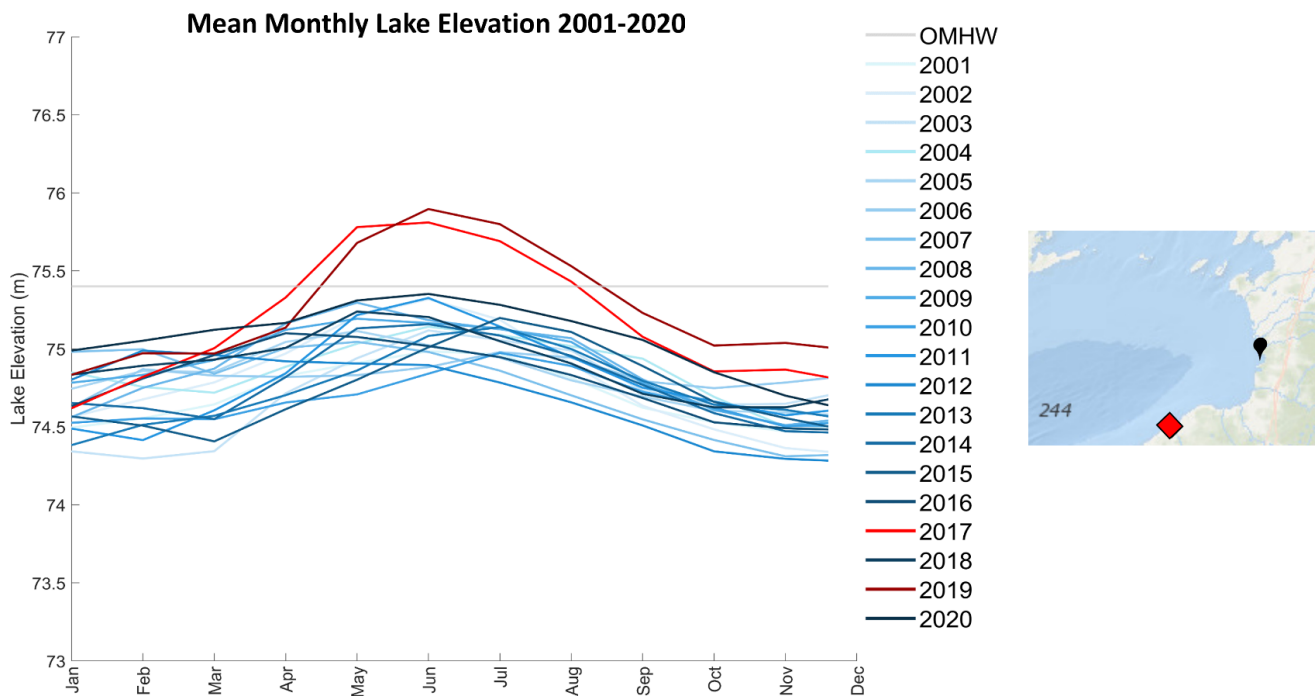


Figure 5. Lake level from January to December for all years included in the study (2001-2020). Exceptionally high water summers are colored red (2017 and 2019). The Ordinary mean high water (OMHW) level is included for reference. Data were collected from the NOAA buoy Station OSGN6 9052030 in Oswego, NY located at the red diamond. The black pin shows the location of the study site (NOAA, 2021a).

The Ordinary Mean High Water (OMHW) for Lake Ontario is 75.4 m and was defined by the International Great Lakes Datum of 1985 to describe the upper limit of the lake level before concern for natural hazards is warranted (IGLD 1985, 1992; Fig. 4 and 5). The datum is periodically updated to accommodate the isostatic rebound of the Canadian side which tilts the surface towards the east (IGLD 1985, 1992).

Storm-derived waves on LO are most often formed by strong west winds driving increased wave heights within the local and broader region. The eastern shore of LO is particularly vulnerable to storm surges and high wave heights because of its alignment with the long axis of the lake and prevailing wind direction (Fig. 3). Wave heights recorded in the basin and on the shore can exceed 6 m and approach the coast as storm surges or seiches (Table 1; Fig. 6). Storm events are most common from late fall and early winter to spring (Grieco and DeGaetano, 2019).

Table 1. Ten highest significant wave heights recorded by Station 45135 in the eastern basin of Lake Ontario (NOAA, 2021b).

Storm Date	Wave Height (m)
1. November 5, 2004	7.69
2. November 1, 2019	6.17
3. April 22, 2006	5.34
4. October 29, 2006	5.31
5. November 19, 2014	5.08
6. November 13, 2003	5.04
7. October 16, 2011	4.78
8. May 20, 2006	4.62
9. November 10, 2018	4.59
10. November 17, 2010	4.49

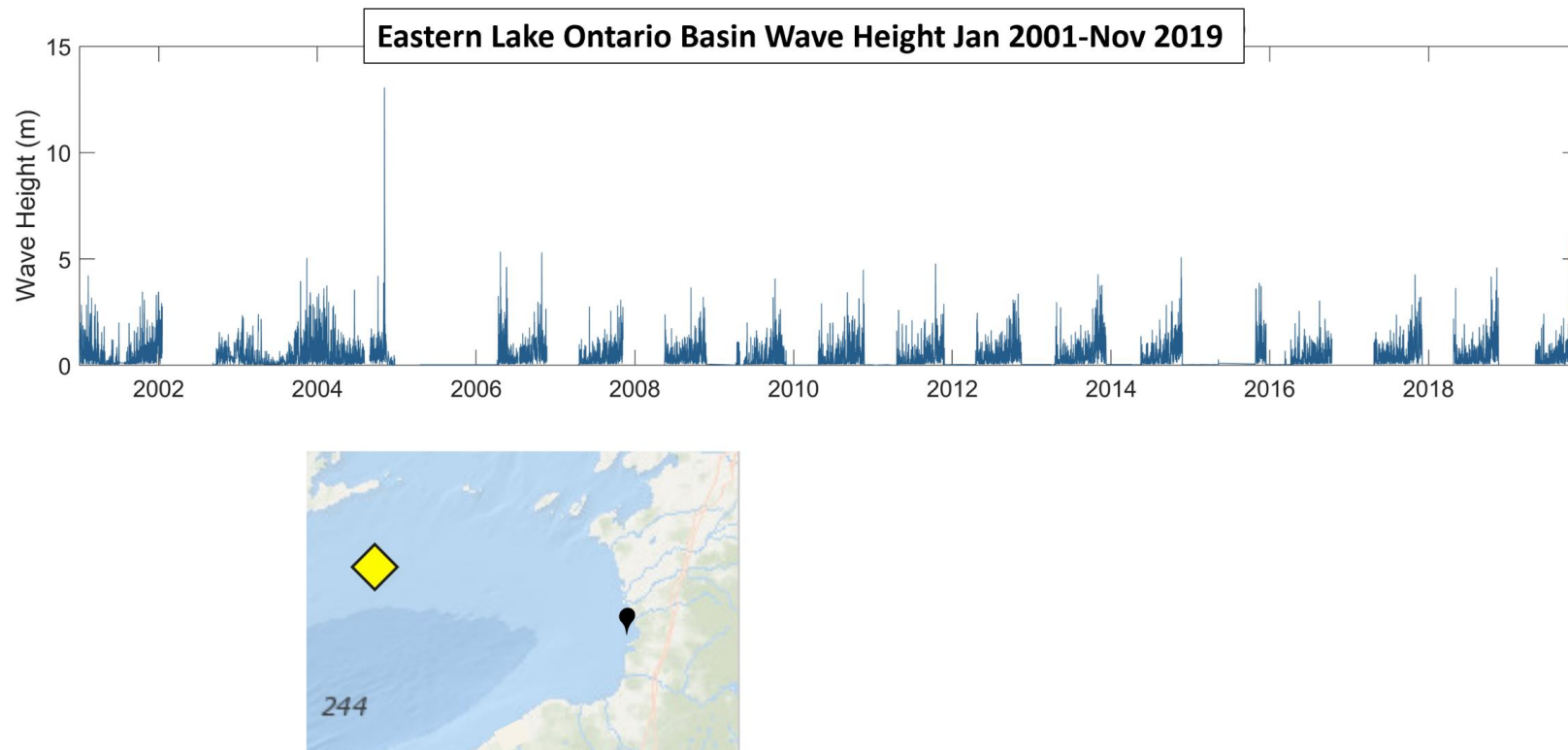


Figure 6. Time series of significant wave heights recorded an offshore buoy (Station 45135 – Prince Edward Point; marked by the yellow diamond) located in the eastern part of the basin (see inset). Wave height is recorded from the spring through fall seasons. The buoy is removed in the beginning of the winter and thus no data are collected during this season. The black marker is the location of the SPS (NOAA, 2021b).

2.2 Human Management. In addition to the natural LO water budget, lake level is managed anthropogenically by the controlled release of water at the Moses-Saunders Power Dam, built in 1958 on the St. Lawrence River near Massena, NY (roughly 108 km SW from Montreal, Quebec; Fig. 3). International regulation of LO began in 1956 with the Order of Appeal, designed to control the lake level according to eleven criteria. These criteria include: regulating outflows to prevent flooding in the city of Montreal; providing economic growth through power generation and shipping; preserving natural shoreline habitats in the watershed; allowing recreational activity; and managing anomalously high or low water supplies (IJC, 2014). The Order of Appeal was approved and in 1963 the accompanying management plan (Plan 1958-D) was implemented. Two major changes in management legislation have occurred since: first, with Plan 1958-DD (allowing minimal deviations); and second, in 2017 with Plan 2014, still in place today (IJC, 2014).

The objective of Plan 2014 is to accommodate for modern climate change while restoring natural flow levels diminished under Plan 1958-DD and the 1963 Order of Appeals (Table 2). Many property owners and recreational users were not in favor of this policy; however, environmental groups strongly supported practices to restore riparian zones and wetlands destroyed under previous management (IJC, 2014).

Table 2. Minimum and maximum lake levels for Lake Ontario permitted under Plan 2014 (IJC, 2014).

Month	Minimum (m)	Maximum (m)
January	73.56	75.26
February	73.62	75.37
March	73.78	75.33
April	73.97	75.60
May	74.22	75.73
June	74.27	75.69
July	74.26	75.63
August	74.15	75.49
September	74.04	75.24
October	73.83	75.25
November	73.67	75.18
December	73.57	75.23

3. *The Sandy Pond spit*

3.1 Geomorphic Context. The Sandy Pond spit (SPS) is a north-south trending barrier-spit system on the eastern shore of Lake Ontario (LO), New York, separating North Sandy Pond from the lake (Fig. 7). It is part of a larger 30 km long sandy shoreline varying from 30-300 m wide. The spit is primarily composed of fine-medium quartz sand and is vegetated by dune grass, cottonwood, sugar maple, white birch, and beech trees. It is fringed by a large back barrier freshwater marsh (Mattheus et al., 2016). The prevailing west winds, in combination with the large fetch of the lake, allow transport and accretion of sand, forming high relief dunes reaching a maximum 15 m in height (Sutton et al., 1972). There is no significant input of sediment into the lake from surrounding streams and rivers and thus all sediment distributed by wave action is from the eastern shore region (Mattheus et al., 2016). Deposited sediment on the beach is from longshore transport to the north. Limited shoreline obstructions include riprap and fencing used to stabilize high-elevation dunes (Mattheus et al., 2016). The barrier originally formed

roughly 5 ka after the pro-glacial Lake Iroquois began receding 12 ka (Sutton et al., 1972; Weir, 1977; Woodrow et al., 2002).

One inlet connects North Sandy Pond to Lake Ontario which has migrated several times since 1900 (Fig. 7; Mattheus et al., 2016). Currently, the inlet is located west of Carl Island, the only island within Sandy Pond and has maintained this location since 1983 (Fig. 8). The channel is used recreationally in the summer, giving boaters access to the lake and beaches of the local state park and is dredged semi-annually to allow access to the lake, as the inlet is naturally filled by the longshore current. Dredging is permitted through the state and the material removed is used to replenish and stabilize various parts of the spit (Table 3).

Table 3. Synopsis of dredging history during study period (Hart and Steadman, 2017; SPCMA, 2022).

Date of dredging	Estimated volume of sand permitted for removal	Description of the project
August 6-9, 2003	6,120 m ³	Sand placed in the “littoral zone” and placed 1000’ north and south of the channel
August 1-8, 2008	6,120 m ³	Placed in the littoral zone; Helped keep the channel open for two summer seasons
September 8, 2010	3,050 m ³	North side of the channel and shoreline
August 15, 2012	3,268 m ³	Placed on the north side of the channel
Unknown date 2013	12,230- 13,000 m ³	N/A
August 8, 2016	4,590-5,350 m ³	September storm filled in much of the inlet where it was dredged closing the channel
August 29- September 6, 2018	9,130 m ³	N/A
September 23- November 4, 2020	8,640-9,170 m ³	Sand removed from the region between Carl Island and the channel inlet
April 20-26, 2021	Not known; dredging was halted by the return of endangered birds; approximately 6,120 m ³ will be dredged this fall	Cleared channel did not remain there through to the spring; sand was used to reinforce the breached region (Zone 2)

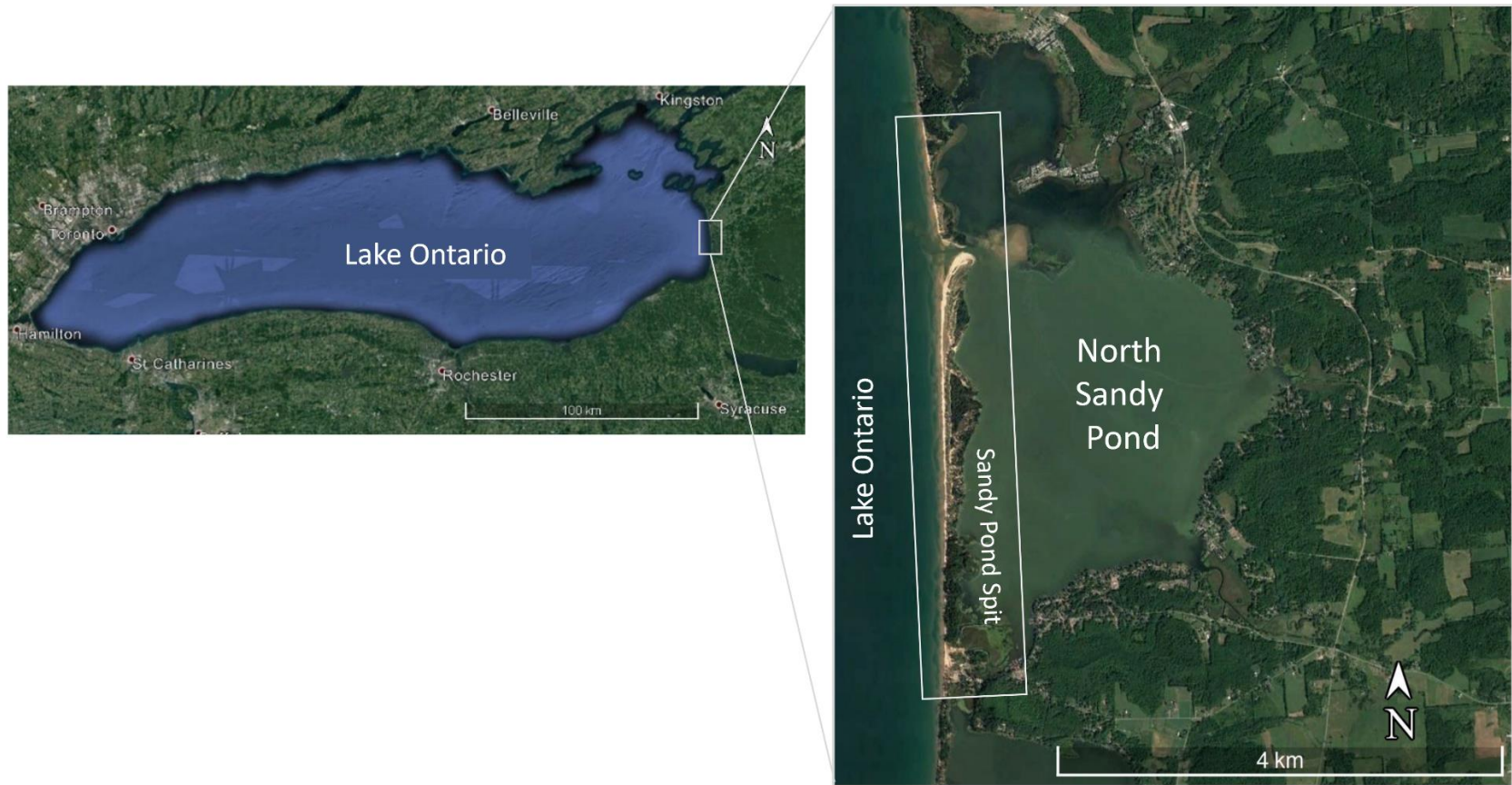


Figure 7. Annotated satellite image of the Sandy Pond spit (inset: Lake Ontario) (from Google Earth, 2022).

3.2 *Previous Work.* Previous work describing geomorphic change in this remote location is limited. Mattheus et al. (2016) analyzed the subsurface sedimentation record, historical images, and maps to understand the overall structure and evolution of the barrier-spit system from 1878 to 2013 (Fig. 8). They concluded that at decadal time scales, lake level is the most influential forcing altering the morphology of the SPS stating, "...the degree of coastal inundation, predominately a function of fluctuating lake levels and antecedent topography, represent strong controls on the overall barrier geomorphology over decadal time-scales" (Mattheus et al., 2016 page 41). The low-

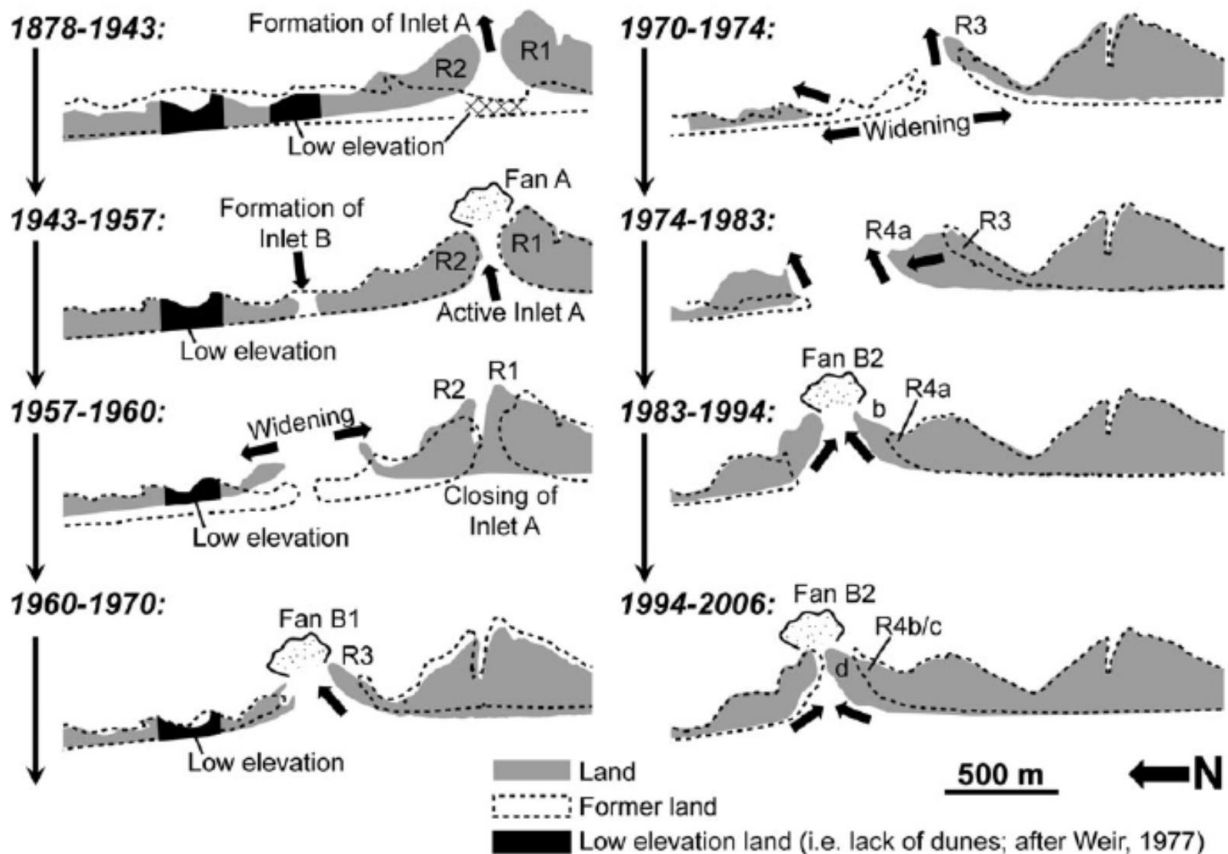


Figure 8. Geomorphic evolution of the SPS from 1878-2006. “R” refers to the formation of recurved ridges surrounding the inlet, and “Fan” refers to the subaqueous fans developing as a result of inlet formation (from Mattheus et al., 2016).

gradient, central portion is subjected to the most change over time and is most vulnerable. High lake levels are directly correlated to lateral migration of spits and inlet channels (Mattheus et al., 2016).

More recently, Hart and Steadman (2017) prepared a report to describe the changes to the inlet and shoreline in an effort to attract attention, support, and funding for preservation of the SPS and dredging in the inlet. Their project titled, “The North Sandy Pond Resiliency Project,” is ongoing. In the initial report, Hart and Steadman (2017) provided a comprehensive description of the history of management, recreation, and dredging as well as first order analysis of shoreline and volume change from the late 1800s to 2015.

4. Motivation

The SPS has received considerable attention for wetland restoration as it is located within and adjacent to multiple Wildlife Management Areas and state parks, composing the Eastern Lake Ontario Barrier Beach Wetland Complex Natural Heritage Area (NHA). As part of an NHA, the SPS and its surrounding waters provide habitat to diverse biota including birds, fish, insects, and plants, some of which are endangered or threatened (NYS DEC 2020).

Two abnormally high-water summers in 2017 and 2019 surpassed the OMHW mark and the maximum monthly water level mandated by Plan 2014 with maximum monthly mean water levels of 75.87 m and 75.92 m, respectively (Table 2; Figure 5; NOAA, 2020a). Both summers resulted in record-setting lake levels that caused shoreline

erosion and destructive flooding along the entire coast of LO (Fig. 9). Floods inundated homes and businesses, placing eight New York counties in a state of emergency, and total damage was valued at hundreds of millions of dollars (Lake Ontario, 2019). Flooding was largely attributed to an abnormally wet spring and winter prior, overwhelming the LO watershed.

In 2017, precipitation in the LO basin was 46.52% higher than the long-term average (1981-2010), while evaporation was 14.62% more than long term average (GLISA, 2017). In 2019, the LO basin received 21.67% more precipitation and 1.01% more evaporation than the long-term average (GLISA, 2019). Climate change is increasing the frequency of storms and thus precipitation in the LO basin, resulting in elevated water levels and increased erosion along the shoreline (Carter and Steinschneider, 2018). High magnitude flooding can alter the stability and resiliency of a barrier system like the SPS, and its fragile ecosystems (Ritter et al., 1978).



Figure 9. Photographic evidence of destruction caused by the high-water summers in the region surrounding the SPS. a-c): shoreline erosion on the SPS (personal collection); d- e): flooded yards and sandbag walls placed in Hamlin, NY near Sandy Pond from the 2019 high water summer (Democrat and Chronicle, 2019); f) flooding from the 2017 high water summer isolating homes (Breederland, 2017).

5. Objectives and Hypotheses

The objective of this study is to quantify morphologic changes on the SPS from 2001-2020 to quantify and describe the geomorphic impact of high-water and storm events at the SPS. To do this I compared three intervals: (1) 2001-2015; (2) 2015-2018; and (3) 2018-2020. The first interval is prior to the high-water summer events, when the lake level was variable, but average. The second and third intervals include the high-water summers of 2017 and 2019, respectively. No significant storms occurred in the second interval, however the second highest wave height event was recorded during the third interval on November 1, 2019, when waves greater than 6 m high struck the barrier-spit (Table 1).

High-resolution lidar data were analyzed in conjunction with sUAS photographs to generate DEM and DEMs of difference (DoDs). Geomorphic change was described using three metrics: (1) shoreline position; (2) dune crest position and elevation; and (3) subaerial volume of erosion and deposition, at both alongshore and whole barrier-spit spatial scales. The subaerial zone is defined by elevations greater than the OMHW elevation of 75.4 m. The analysis will test the following six hypotheses (Table 4):

- H1.** The SPS system is transgressive.
- H2.** The rate of eastward shoreline migration increased from 2015-2020 compared to 2001-2015.
- H3.** The net change in volume of sediment of the subaerial SPS system was negative during the high-water summers; the SPS system lost a significant amount of subaerial sediment from 2015-2020.
- H4.** The volumetric erosion is concentrated on the beach during high lake level summers.
- H5.** The alongshore average change in dune crest position and elevation is eastward and negative, respectively from 2007-2020.
- H6.** Lake levels are the most important erosional forcing impacting the SPS.

Table 4. List of hypotheses and their respective tests.

Hypothesis	Metric Used in Test	Test
H1. The SPS system is transgressive.	Shoreline; Foredune crest	Shoreline position and elevation were studied using OMHW of 75.4 m. The Digital Shoreline Analysis System (DSAS) was used for computing the lateral rate of shoreline movement in meters per year using the 2001, 2015, 2018, and 2020 contours (m/year). Lateral foredune crest movement was measured using the identified foredunes and the DSAS algorithm to quantify the rate of movement between 2007-2015, 2015-2018, and 2018-2020.
H2. The rate of eastward shoreline migration increased from 2015-2020 compared to 2001-2015.	Shoreline	Using the DSAS and OMHW elevation contours, rate of shoreline movement (m/year) was computed from the rate of shoreline change for 2001-2015, 2015-2018, and 2015-2020.
H3. The net change in volume of sediment of the subaerial SPS system was negative during the high-water summers; the SPS system lost a significant amount of subaerial sediment from 2015-2020.	Volume of erosion and deposition	For each DoD, the net change in subaerial volume of erosion was computed and compared at each of the seven geomorphic zones during the 2007-2015 and 2015-2018 intervals. Cross-shore topographic profiles are generated to interpret volumetric changes from 2018-2020.
H4. The volumetric erosion is concentrated on the beach during high lake level summers.	Volume of erosion and deposition	The location of statistically significant geomorphic change on the DoDs generated for 2007-2015, 2011-2015, and 2015-2018 are compared determine where along the barrier-spit erosion is most common.
H5. The alongshore average change in foredune crest position and elevation is eastward and negative, respectively from 2015-2020.	Foredune crest	Transects generated from the DSAS analysis will be used to measure alongshore variation in the foredune crest position and height. The alongshore change in foredune crest position was computed for the 2007, 2011, 2015, and May 2018, September 2018, and August 2020 data were calculated to determine the mean change in position across the study area during the 2007-2015, 2015-2018 and 2018-2020 intervals. Foredune crest height was analyzed qualitatively based on the type of geomorphic change occurring.
H6. Lake level is the most important erosional forcing impacting the SPS.	Volume of erosion and deposition; Shoreline; Foredune crest	All analyses will be used to compare the 2001-2015, 2015-2018, and 2018-2020 intervals to describe the erosive impact water-level has on the SPS and how it drives geomorphic change to the barrier-spit.

6. Methods

The following methods describe the workflow used for collecting and processing data into DEMs, quantifying metrics, and extracting results.

6.1 Lidar datasets. Six lidar surveys from 2001-2018 were downloaded from the NOAA Data Access Viewer as pre-classified point cloud data (Table 5; NOAA, 2021c). The ground and water returns were isolated for processing to generate bare earth DEMs. Data were projected onto the horizontal North American Datum of 1983 (NAD83) State Plane New York Central and vertical North American Vertical Datum of 1988 (NAVD88) coordinate systems, both in meters.

Table 5. Summary table of lidar datasets available from NOAA data access viewer (NOAA, 2021c). Point density is calculated over the entire survey area. (Abbreviations: USACE: United States Army Corps of Engineers; JALBTCX: Joint Bathymetry Technical Center of Expertise; SHOALS: Scanning Hydrographic Operational Airborne Lidar Survey; NCMP: National Coastal Mapping Program; CHARTS: Compact Hydrographic Airborne Rapid Total Survey; ACA: Aerial Cartographics of America; FEMA: Federal Emergency Management Agency; NYS OITS: New York State Office of Information Technology Services).

Date		Source	Data Type	Approx. Point Cloud Density (pts/m ²)	Accuracy		DEM resolution (m)
Start	End				Horizontal	Vertical (E_{sur})	
5/9/2001	8/1/2001	USACE/JALBTCX/ SHOALS	Topobathy	0.048	3 m	0.15 m	4
7/14/2007	7/30/2007	USACE/NCMP/ CHARTS/JALBTCX	Topo and hydrographic	0.226	0.75 m	0.20 m	1
6/6/2011	9/23/2011	USACE/JALBTCX/ CHARTS	Topobathy	0.250	0.75 m	0.20 m	1
10/27/2014	10/27/2015	USGS/ACA/FEMA	Topographic	2.041	0.843 m	0.290 m	0.5
5/2/2018	5/5/2018	USGS/NYS OTIS	Topographic	2.041	0.03 m	0.0486 m	0.5
9/15/2018	9/18/2018	USACE/NCMP/ JALBTCX	Topobathy	7.98	< 1 m	< 19.6 cm	0.5

The 2001 lidar survey was conducted by the United States Army Corps of Engineers (USACE) in two separate surveys, one for topographic returns, the second for bathymetric returns in water up to 10 m deep (Table 5). This dataset was previously used to generate a 4 m DEM and had a point density of 0.048 pts/m² (Hart and Steadman, 2017). The reported horizontal and vertical accuracy of the dataset are 3 m and 0.15 m, respectively (NOAA, 2021c).

The 2007 topobathymetric dataset is from a Compact Hydrographic Airborne Rapid Total Survey (CHARTS) system conducted in partnership with the USACE National Coastal Mapping Program (NCMP) along the entire New York coast of Lake Ontario. The dataset includes unclassified, ground, and bathymetric points with a density of 0.226 pts/m² (Table 5). Metadata reported the horizontal and vertical accuracy are 0.75 m and 0.20 m, respectively (NOAA, 2021c).

The 2011 topobathymetric survey was collected by the USACE using the CHARTS system along the shore of Michigan and New York Great Lakes. The data are tiled into 5 km long swaths of data for simpler download and have a point density of 0.25 pts/m² (Table 5; NOAA, 2021c).

The 2015 survey was collected in an effort by the Aerial Cartographics of America (ACA) and the Federal Emergency Management Agency to acquire lidar in seven New York State counties including Oswego and Jefferson of which SPS lies within. Horizontal and vertical accuracy were 0.843 m and 0.290 m, respectively. Point density was 2.041 pts/m² and data were tiled into 1.5 km² tiles for more manageable processing (Table 5; NOAA, 2021c).

There are two 2018 surveys encompassing the SPS. The first is a USGS survey collected in partnership with the New York State Office of Information Technology Services (NYS OITS) focusing on Cayuga and Oswego counties for flood analysis following the summer of 2017 (Table 5; NOAA, 2021c). This topographic dataset is tiled into 1.5 km² tiles with an average point density of 2.041 pts/m². The reported vertical accuracy is 0.049 m (NYS OITS, 2019). The horizontal error is not explicitly reported in the metadata but meets the standards designating an average and maximum error of 0.03 m and 0.15 m, respectively (NYS OITS, 2019).

The second 2018 survey focuses on the New York coastline along Lake Ontario with the USACE NCMP collected by the Coastal Zone Mapping and Imaging Lidar (CZMIL) system. It is divided into 1 km² tiles for download and consists of classified ground and bathymetric data. The horizontal and vertical error are not explicitly stated in the metadata, but again met standards of less than 1 m and 0.196 cm, respectively (Table 5; NOAA, 2021c).

Woolard and Colby (2002) recommend a maximum resolution of 1 m for DEMs measuring volumetric change in dunes, although some studies used finer resolution DEMs to measure such changes (Johnson et al. 2018; Lallias-Tacon et al. 2014). The resolution of a DEM is directly related to the point density of the lidar survey (Fig. 10). That is, increased point density produces higher resolution DEMs because there is more data to assign a value to a particular cell. Due to improvements in technology, more recent studies and surveys have the higher density point clouds.

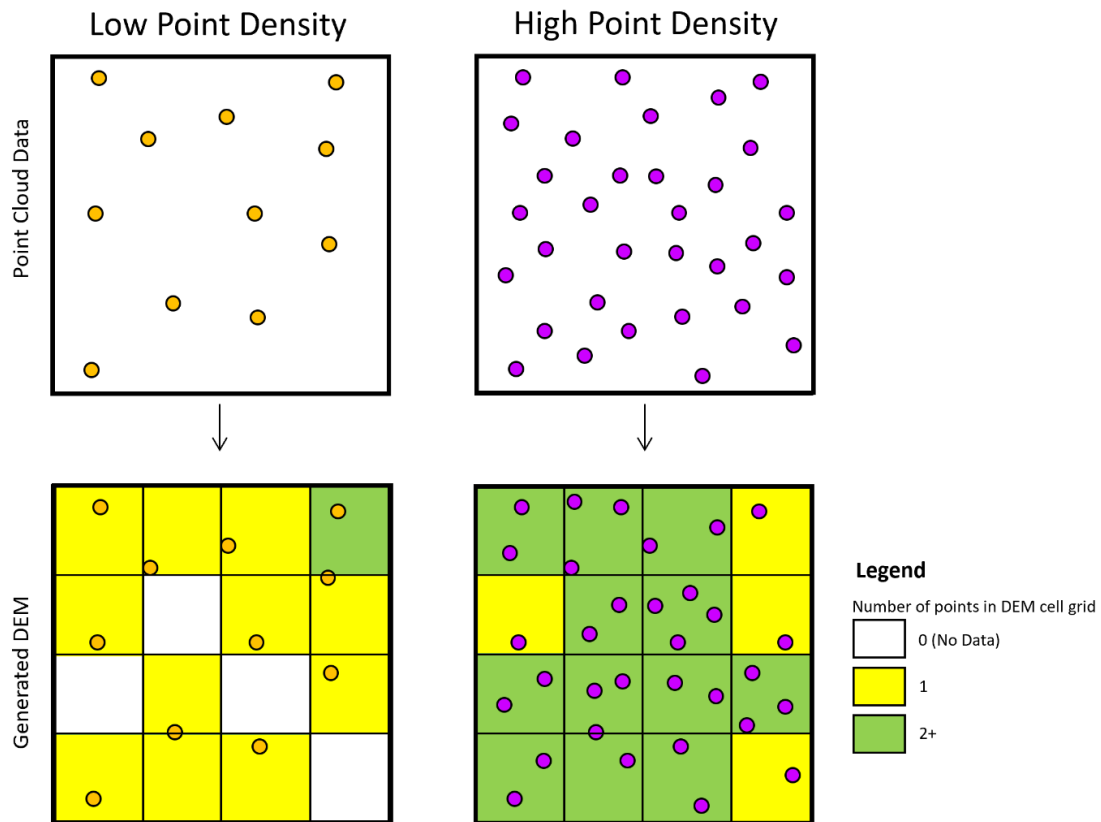


Figure 10. Illustration demonstrating how point density effects DEM resolution. When there are fewer points in the dataset, there it is more likely that some cells of the grid will be empty, without data, the higher the point density is, the more likely it is a data point is within the grid cell of the DEM. If one data point lies within a cell, the cell value will equal that of the data point. If there are multiple datapoints within a cell, the cell will be assigned a value equal to the average of that of the data points which fall in the cell.

With roughly 20 years of lidar datasets for the SPS system, it was important to consider the point density of each dataset and determine if it met the suggested 1 m DEM resolution guideline. Detailed examination of the 2001 dataset indicated it was not dense enough to meet this requirement; all other datasets were satisfactory. For this reason, the 2001 dataset was only used for shoreline position analysis. The 2015-2018 datasets were especially high resolution and accurately rendered a 0.5 m resolution DEM (Table 5).

6.2 Fieldwork. Fieldwork was conducted during the summer of 2020 to measure change after the storm and high-water event of 2019. To adequately capture the geomorphic change on the whole barrier spit, seven ecogeomorphic zones were identified and studied for analysis. Ecogeomorphic zones were identified based on topography and vegetation density and type (Fig. 11). The seven geomorphic zones were surveyed by 10 sUAS flights and numerous GPS surveys. Together, these zones characterized the entire SPS system and barrier islands in general (Brantley et al., 2014).

sUAS flight surveys used a DJI Phantom Advanced 4 vehicle, a Leica Viva GS14 Real-Time-Kinematic GNSS system, and aerial targets to mark ground control points (GCPs). The sUAS was equipped with a 9 mm focal length and 2.97 maximum aperture DJI FC6310 camera. Autonomous flight courses planned in the DroneDeploy iOS application were used to direct the sUAS during flight. Eight aerial targets were dispersed in the survey area, all photographed 67.0 m above ground, apart from Zone 5 (76.2 m above ground). Photographs had an estimated 75% side lap and overlap. Each zone was surveyed once per field campaign from June 29-July 3, 2020, and August 4-8, 2020. The total area covered by surveys is approximately 0.68 km² (Fig. 11). A consistent procedure was used to execute each flight and minimize human error (Table 6).

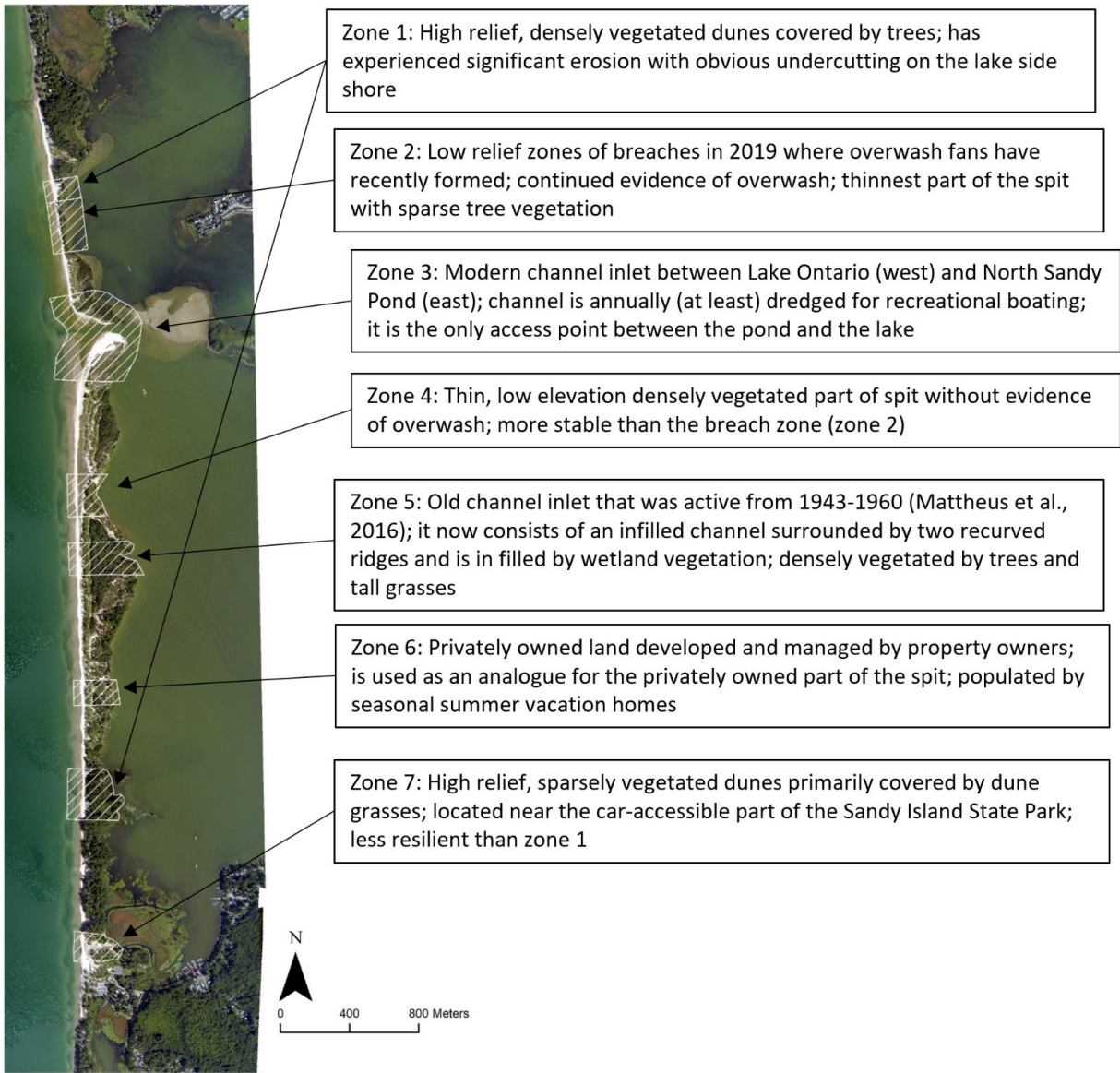


Figure 11. Map and description of the seven ecogeomorphic zones identified for sUAS data collection and analysis.

Table 6. Procedure for sUAS field surveys.

sUAS field survey procedure:
1. Place 8 ground control points (GCP) markers evenly throughout the entire study area. GCPs must be placed in open air locations so the sUAS will capture them in photographs taken. It is best to place GCPs on a variety of types of topographic areas. They must be placed so they will not move during flight.
2. Ready the sUAS for flight. Turn on the drone and controller and connect it to the Drone Deploy application on an iOS device. Load the flight plan and complete the pre-flight check.
3. Conduct the sUAS flight. During flight it is necessary to keep the sUAS in view at all times. Flights last 8-15 minutes.
4. Once the flight is complete assemble the RTK GPS. This includes placing the antenna on the pole and attaching the controller.
5. While taking notes, the RTK GPS is used to measure the horizontal and vertical position of the center of the GCP markers. Additional measurements throughout the study area are calculated for use in error analysis.
6. A transect between two GCPs is placed in line with each other on the shore and is measured at 1-2 m intervals for error analysis. After finishing notes and recording all GPS data, the survey is complete.

GPS surveys were essential to quantify error of DEMs and georeference photographic data. Error analysis is detailed in section 6.5. All measurements were recorded in the NAD83 Universal Transverse Mercator (UTM) Zone 18N and NAVD88 horizontal and vertical coordinate systems. Two types of GPS surveys were collected for analysis: the first with sUAS flights, and the second for lidar data. All measurements used a targeted vertical accuracy of 0.030 m or less. Data with vertical accuracy greater than or equal to 0.060 m were omitted. GPS surveys collected in conjunction with each sUAS flight were used to georeference images and assess the survey error of SfM DEMs. For each sUAS survey, GPS data were collected along a transect connecting two GCPs and extended into the water for additional measurements; these data were used to compute the interpolation error (see section 6.5).

GPS measurements collected at three additional checkpoints were used to compute the interpolation error of lidar DEMs (Fig. 12). The checkpoints were located in different parts of the study area on paved roads that have not experienced vertical change between lidar surveys (Zhang et al., 2005; Mitasova et al., 2009). A minimum of 60 measurements at each checkpoint were recorded each spaced roughly a meter apart from each other.



Figure 12. Map of checkpoints used for lidar interpolation error.

6.3 DEM generation: Lidar. Lidar DEMs were generated from point cloud data using the LAS toolbox in ArcGIS (Fig. 13 and 14a). Point cloud data were clipped to the study area and filtered to extract only ground and water returns, when available. After determining the appropriate resolution for the DEM, the filtered point cloud data were used to generate a triangular irregular network (TIN). Then, the TIN was used to linearly interpolate a DEM raster. Once complete, the DEM was ready for error analysis. The tiled 2015 and 2018 datasets were higher resolution than the others and thus tiled again in DEM generation. To prevent coarsening the resolution of the data, a DEM was generated for 28 tiles with at least 50 m of overlap. The DEMs tiles were then merged to form a single raster.

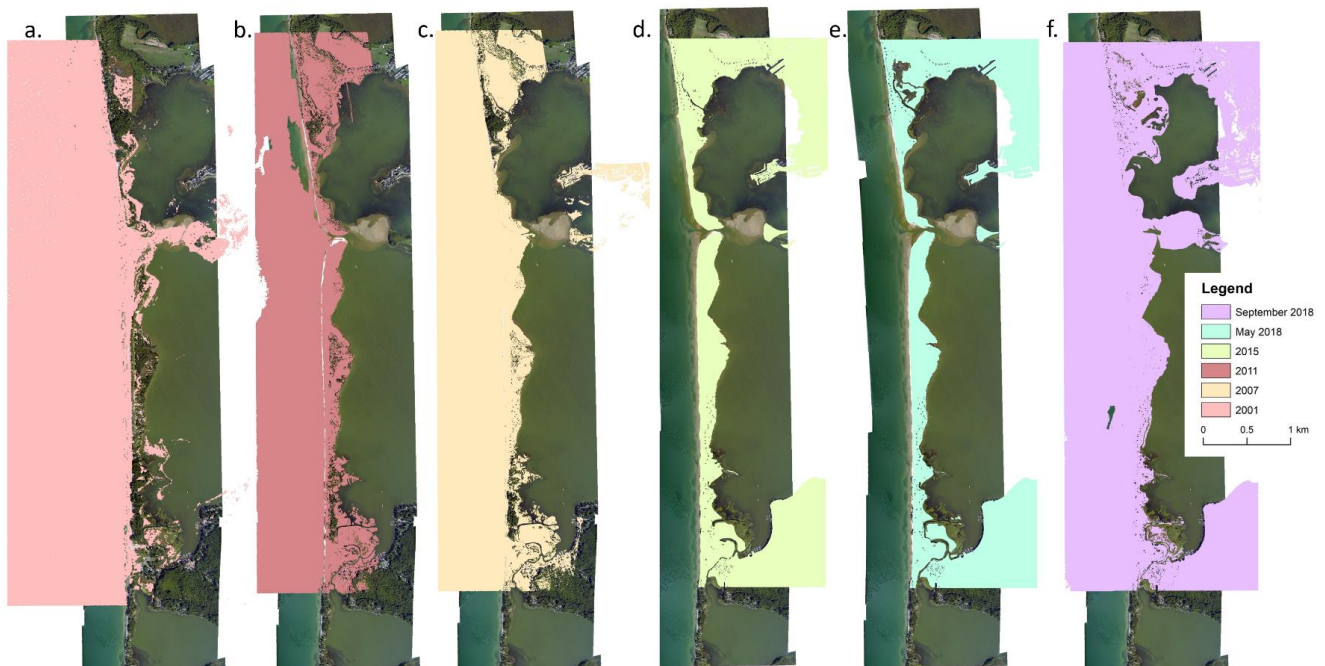


Figure 13. Extent of lidar coverage for all study datasets. a) 2001; b) 2007; c) 2011; d) 2015; e) May 2018; f) September 2018. The base map is a 2016 aerial image.

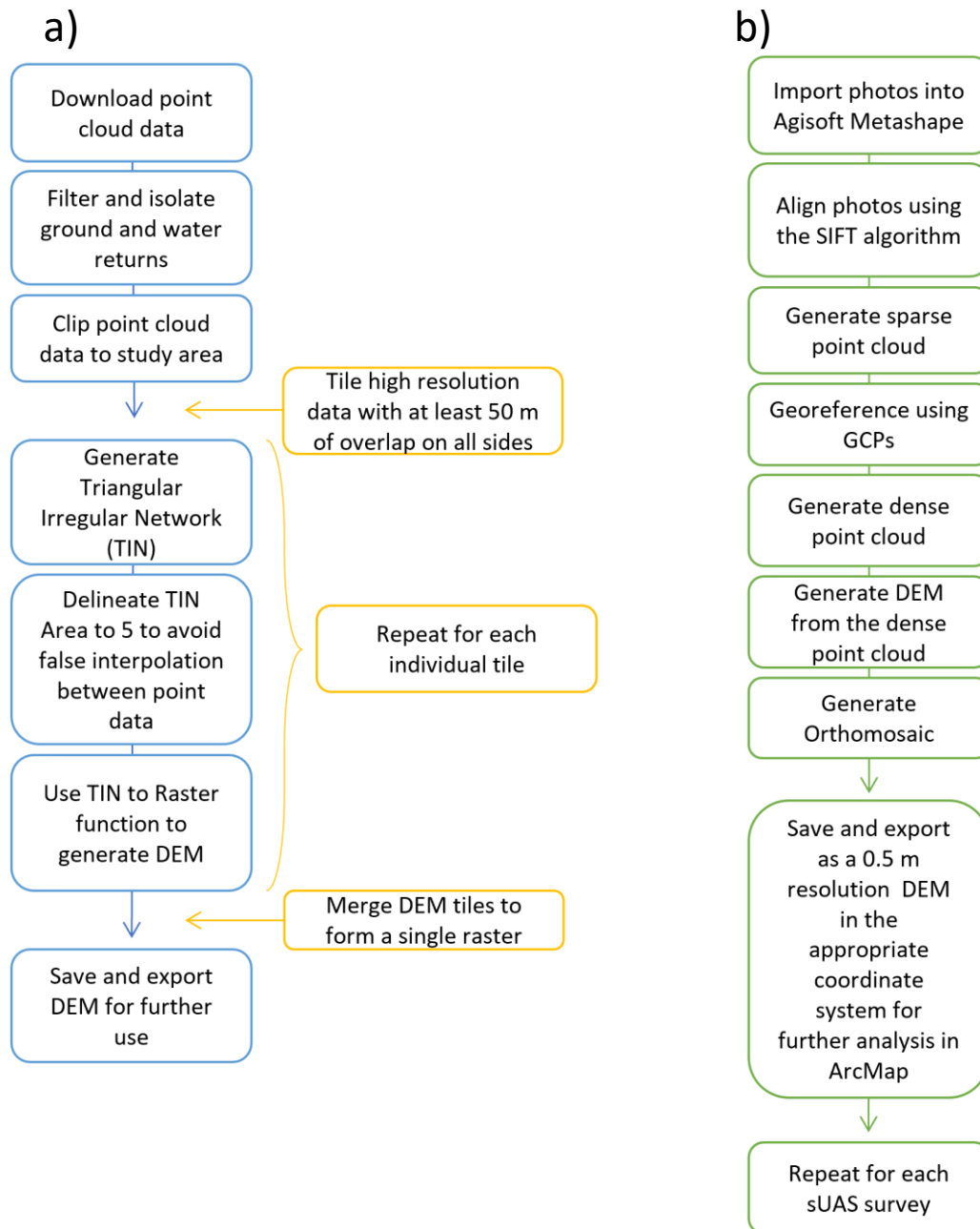


Figure 14. DEM generation workflow for lidar and SfM data. a) Lidar DEM workflow; steps highlighted in yellow were only used for high resolution point cloud data from the 2015 and 2018 surveys. b) SfM DEM generation workflow.

6.4 DEM generation: Structure-from-Motion. sUAS images collected in the field were used to generate a point cloud and DEM using SfM techniques adapted from the methods of Westoby et al. (2012) and Shervais and Dietrich (2016). Agisoft Metashape software was used to process all data collected during the August 2020 surveys. An individual DEM was generated for each geomorphic zone (Fig. 14b).

After importing survey images into the Metashape workspace, images were aligned using a Scale-Invariant Feature Transform (SIFT) algorithm. This identifies the same features within overlapping photographs and stitched the images together (Shervais and Dietrich, 2016). Because the survey captured the surface at different angles, the SIFT algorithm aligned photographs in 3D space. A point recognized in two or more images used to mosaic photographs together was called a ‘tie point.’ A minimum of 4,000 tie points was recommended for high accuracy alignment (Kim, 2018). This produced a ‘sparse point cloud’.

The sparse point cloud was manually georeferenced using the GCPs collected in the field by locating the aerial targets in the individual images with the GPS-measured horizontal and vertical coordinates. Once georeferencing was complete, error statistics were calculated as a root mean square error (RMSE). This defined the survey error (E_{sur}) used in subsequent error analysis (see section 6.5).

After georeferencing, a dense point cloud was generated from the sparse point cloud. The dense cloud function used ‘high’ quality reconstruction with ‘mild’ depth filtering settings (Shervais and Dietrich, 2016). The dense point cloud filled vacancies in sparse cloud and provided the data needed to generate 0.5 m resolution DEMs.

Dense point clouds included vegetation and buildings, modeling what was captured in the photographs and not exclusively the bare earth. The dense point cloud was not edited before being used to generate a DEM and thus, the resulting model included vegetated surfaces and water. Vegetation is not easily filtered from SfM point cloud data and as such was included in the models (Sherwood, 2021). The DEM generated from SfM was used to create an orthophotograph of each survey. Map products created in Agisoft Metashape were exported as .TIF files projected using the NAD83 State Plane New York Central and North American Vertical Datum of 1988 coordinate systems to match the projected coordinate system of all lidar data. Further analysis of these products was conducted in the ArcGIS workspace.

6.5 DEM Error. It was necessary to consider the error of individual DEMs when interpreting geomorphic change. The RMSE statistic is reliably used to identify and isolate statistically significant change in coastal settings measured by MTE analyses (Balaguier-Puig et al., 2017; Le Mauff et al., 2018). DEM error was calculated by:

$$E_{DEM} = E_{sur} + E_{int} \quad , \quad (1)$$

where E_{DEM} equaled the total error of a DEM, E_{sur} was the RMSE of the survey and E_{int} was the RMSE of the interpolation (Balaguier-Puig et al., 2017). Survey error was equivalent to the vertical error provided in the metadata for lidar surveys and the RMSE of georeferencing provided in the report given by Agisoft Metashape for SfM datasets. Interpolation error was calculated using:

$$E_{int} = \sqrt{\frac{\sum_{i=1}^n (I_i - M_i)^2}{n}} \quad , \quad (2)$$

where M_i was the measured elevation value for a horizontal position, I_i was the interpolated elevation for the cell with the same horizontal position, and n was the number of data points used in the error calculation. For lidar derived DEMs, interpolation error (E_{int}) was equal to the RMSE of the GPS data collected at checkpoints (M_i) and the cell value of the DEMs (I_i). Each DEM dataset was assigned its own interpolation error (Table 7). For SfM derived DEMs, interpolation error (E_{int}) was the RMSE calculated using the DEM (I_i) and additional RTK GPS data points (M_i) collected that were not used in georeferencing. E_{int} was calculated for each individual zone and at least 18 data points were used in computation (Table 7). A complete summary of DEM error is provided for all lidar and SfM derived DEMs (Table 7).

Table 7. Summary of error calculations for Lidar and SfM derived DEMs. The term n refers to the number of RTK GPS measurements used to determine the accuracy of the interpolated DEM.

Date	E_{sur} (m)	n	E_{int} (m)	E_{DEM} (m)
May 2001	0.15	42	0.239	0.282
July 2007	0.20	233	0.063	0.210
June 2011	0.20	241	0.083	0.216
October 2015	0.290	241	0.083	0.302
May 2018	0.048	240	0.040	0.063
September 2018	0.196	239	0.065	0.207
August 2020 Zone 1 North	0.016	18	0.037	0.040
August 2020 Zone 1 South	0.010	26	0.069	0.069
August 2020 Zone 2	0.007	36	0.299	0.031
August 2020 Zone 3	0.018	108	0.041	0.045
August 2020 Zone 4	0.008	34	0.032	0.033
August 2020 Zone 5	0.003	26	0.090	0.090
August 2020 Zone 6	0.006	27	0.052	0.053
August 2020 Zone 7	0.012	22	0.088	0.089

6.6 DoD Computation and Error Analysis. To quantify volumetric change, DEMs of Difference (DoD) were created for two intervals, pre-high-water events (2007-2015) and including the summer of 2017 (2015-2018). DoDs must be generated from two DEMs with the same resolution for equal comparison (Wheaton et al., 2010). The raster math tool automatically resampled the input DEMs to the coarsest resolution during subtraction. The 2007-2015 and 2011-2015 DoDs were both 1 m and the 2015-2018 DoD was 0.5 m resolution (Table 8). Three DoDs were generated for analysis (2007-2015, 2011-2015, and 2015-September 2018) using the ArcMap raster math minus function to subtract the recent DEM from the past DEM. This results in negative elevation values corresponding to removal of material, or erosion, and positive values addition or deposition. Both the 2007-2015 and 2011-2015 DoDs were necessary to capture change prior to the high water events because the lidar coverage varied (Fig 13).

Table 8. Summary of DoDs generated from lidar data and their corresponding resolution and error.

DoD	Resolution (m)	Notes	E_{DoD}	LoD_{min} (m)
July 2007- October 2015	1	Prior to high water summers summary	0.368	0.721
June 2011-October 2015	1	Prior to high water summers summary	0.371	0.728
September 2018- October 2015	0.5	High water summer of 2017 (topographic only)	0.366	0.718

The error in individual DEMs used to generate the DoD was propagated into the DoD, so it is necessary to compute the DoD error to define and identify measurable changes in elevation (Wheaton et al., 2010). For this reason, a threshold called the limit of detection (LoD), was used to define and bound noise and error around an elevation

change equal to zero. Elevation changes less than the magnitude of the LoD are considered statistically insignificant.

To compute the LoD, the error of the DoD (E_{DoD}) is needed. This was calculated as the RMSE of the errors of the two individual DEMs:

$$E_{DoD} = \sqrt{E_{new}^2 + E_{old}^2} , \quad (3)$$

where the error of the more recent DEM (E_{new}), and the error of the older DEM (E_{old}) are used (Le Mauff et al, 2018).

The minimum limit of detection (LOD_{min}), was calculated by applying a confidence interval to the error of the DoD. Here, a 95% confidence interval was used to isolate statistically significant change (Le Mauff et al., 2018; Lallias-Tacon et al., 2014; Wheaton et al., 2010). The minimum threshold value computation assumes the error of a DoD is equivalent of the standard deviation of the error of DoD, and is multiplied by the confidence interval t-statistic ($t = 1.96$):

$$LOD_{min} = t \cdot E_{DoD} \quad . \quad (4)$$

If error was deemed spatially uniform, a single LOD_{min} value was applied to the whole DoD (Le Mauff et al., 2018). In this case, a uniform error was assumed and cells in the interval $[-LOD_{min}, LOD_{min}]$ were considered noise and omitted from volumetric calculation. Alternatively, error can be calculated with a non-uniform LOD_{min} in which a separate value is assigned to each individual cell or a group of cells of the DoD (Lallias-Tacon et al., 2014). For the sake of simplicity and first order calculations, error was assumed to be uniform (Table 8). If a cell was within the noise interval, and thus considered non-significant change, it was not included in the 95% confidence interval

volumetric change calculation. After the LOD_{min} threshold was applied the DoD was ready for metric computation.

6.7 Metrics. Methods used to extract and quantify change from DEMs and DoDs were modeled after previous studies to effectively describe geomorphic change on the SPS from 2001-2020 at alongshore and whole-barrier spatial scales. Shoreline position, dune crest position and elevation, and subaerial volumetric change were studied at the three intervals: 2001-2015, 2015- September 2018, and September 2018-2020, to isolate the impact of high-water events and storms on the SPS (Zhang et al., 2005; Nagarajan et al., 2019; Eisemann et al., 2018).

6.7.1 Shoreline position. Shoreline migration was computed using the USGS Digital Shoreline Analysis System (DSAS) toolbox in ArcMap (Himmelstoss et al, 2018). To compare shorelines of equal elevation through time, the OMHW contour (75.4 m) was extracted from all DEMs to study the three intervals. Intermediate shorelines such as 2007, 2011, and May 2018 were used to visually represent changes in position within the intervals. DSAS analysis inputs included the baseline, placed offshore produced by smoothing the shorelines from the study period. Transects were cast perpendicular from this baseline 25 m apart along 5.84 km of the shoreline defining the study area (Fig. 15) (Houser et al., 2008).

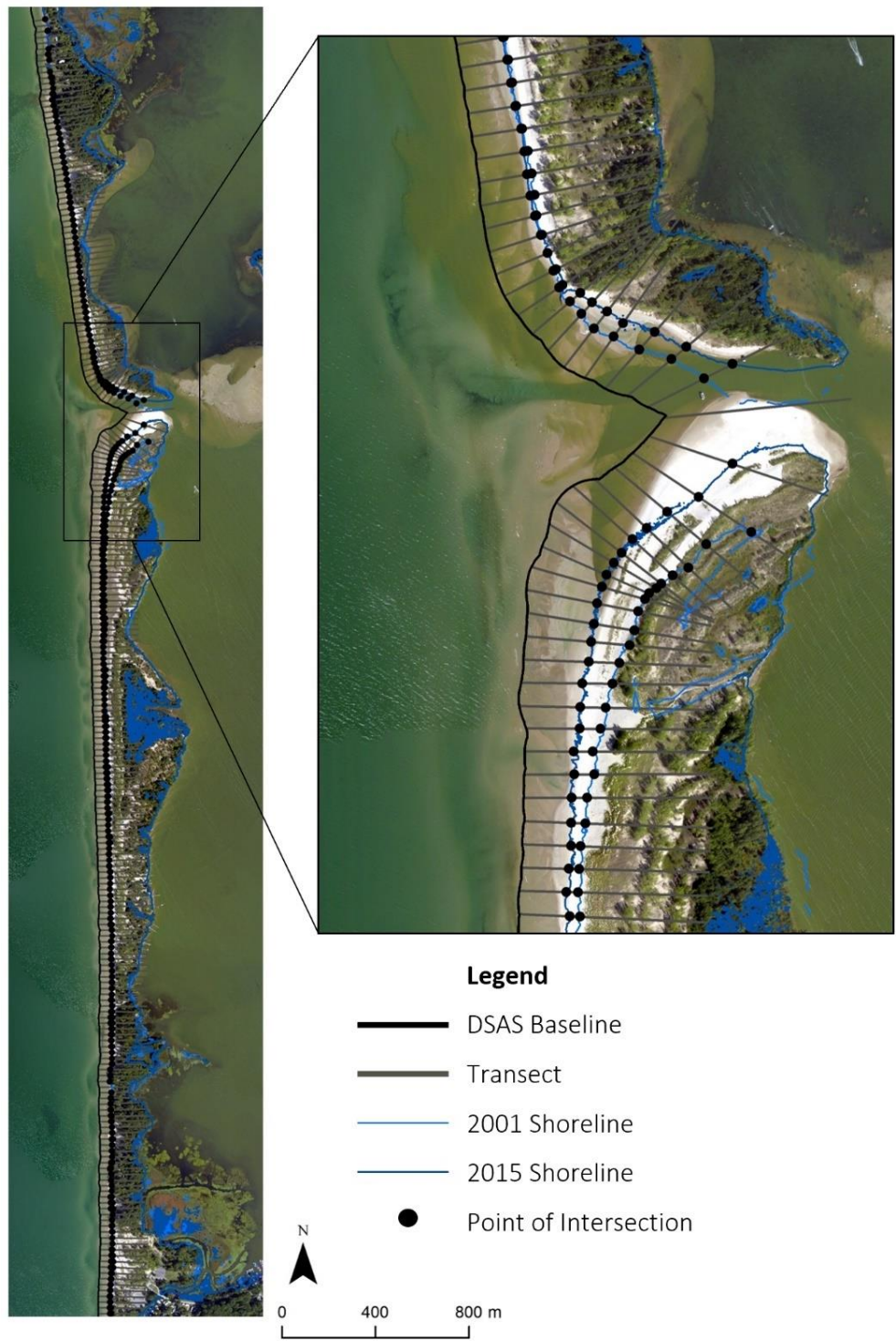


Figure 15. Summary of the components of the DSAS analysis.

Three calculations were made for each interval: the shoreline change envelope (SCE), the net shoreline movement (NSM), and the rate of shoreline change (RSC). The SCE was the total magnitude of shoreline migration measured, indicating no direction of movement. The NSM assigned a direction of retreat or advance to the SCE values, and the RSC calculated a rate of migration in meters per year (m/year) from the NSM values. Negative NSM and RSC values represented shoreline retreat, and positive advance. Because high magnitude fluctuations in the position of the shoreline occurred in the inlet region, an “adjusted mean” was introduced which omitted records influenced by the inlet channel migration.

6.7.2 Foredune crest position and elevation. For the purposes of this study, the foredune crest was defined as the dune crest located closest to the LO shoreline and beach (Fig. 1). Foredunes were manually identified using expert eye interpretation of aerial images and slope, hillshade, and DEMs rasters (Fig. 16). The foredune crest was located at a topographic inflection point, where the profile of the beach alters from lake-facing to pond-facing and the slope is near zero.

The foredune crest location was identified where possible along the same transects cast for shoreline analysis. The 2011, 2007, 2015, September 2018 and August 2020 datasets were used for this analysis to study the 2007-2015, 2015-2018, and 2018-2020 intervals (Fig. 17). In some regions of the spit, the foredune crest could not clearly be determined, and was not recorded for the transect. Due to the varying coverage of the 2007 and 2011 datasets, both were needed to create a complete dataset for describing pre-high-water event change over the 2007-2015 interval (Fig. 13).

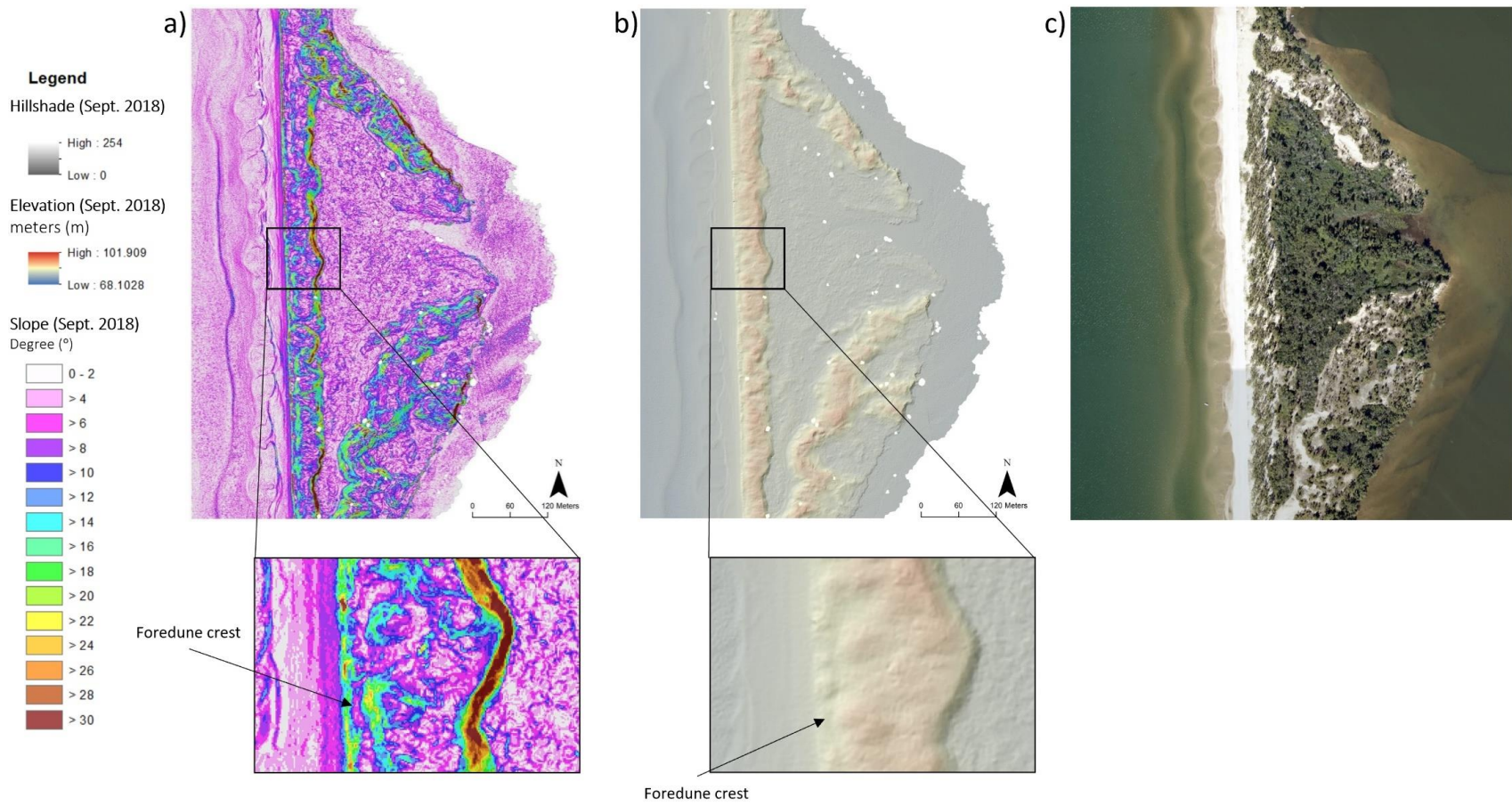


Figure 16. Summary of the foredune crest identification procedure at Zone 5. a) slope map with inset describing the location of the foredune; b) Hillshade and DEM with inset of the foredune crest location; c) aerial photograph showing vegetation line.

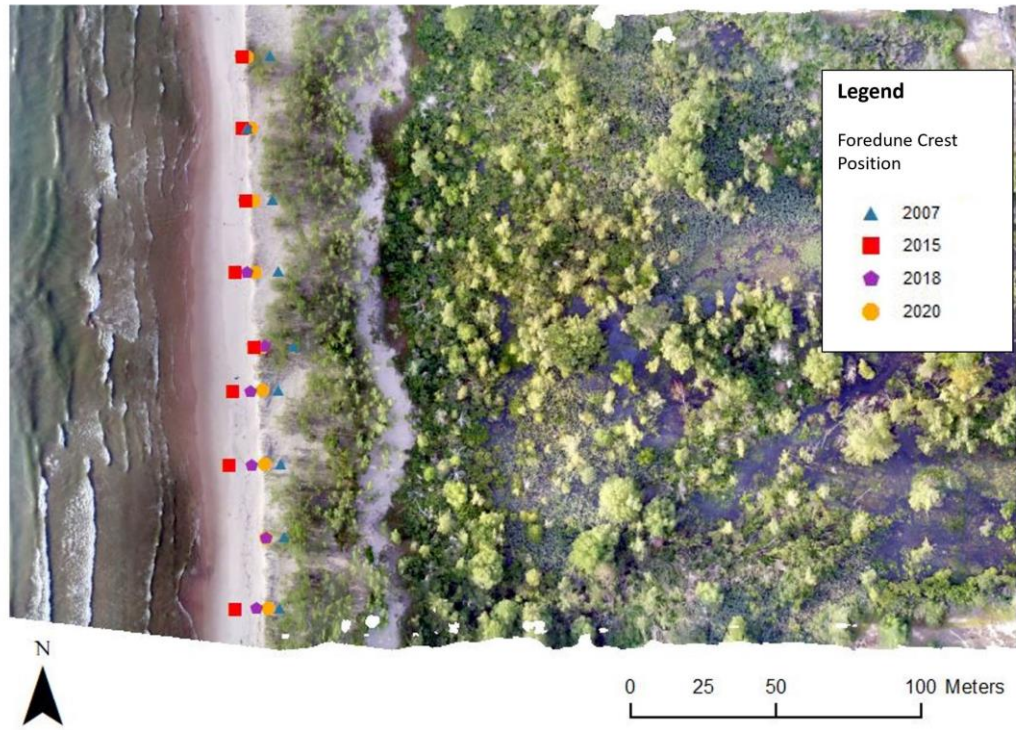


Figure 17. Example of identified foredune crests in Zone 5 from 2007-2020.

Both the vertical and horizontal position of the foredune crest over time were studied. The lateral movement of the foredune crest was computed using the DSAS algorithm with the same baseline and transects used for shoreline. Again, three calculations were made to measure lateral movement: the foredune crest change envelope, net foredune crest movement, and the rate of foredune crest change. Negative values represented eastward movement (landward) and positive values represented westward movement (lakeward).

The elevation of identified foredunes were extracted from their respective DEMs and imported into MATLAB for further analysis. From these data, the alongshore vertical magnitude and rate of change were analyzed. The 2020 dataset was not included in this analysis because the SfM could not filter out vegetation.

Representative cross-section profiles were extracted at each ecogeomorphic zone, to study the cross-shore evolution of the barrier from 2007-2020 (Fig. 11) (Houser et al., 2008; Stockdon et al., 2009). For each, elevation data was extracted imported into MATLAB to generate graphs illustrating the change in topography. The foredune crest was again identified graphically and used to verify previously identified foredune crests.

6.7.3 Volume of erosion and deposition. Volumetric change analysis was limited to the subaerial region of seven ecogeomorphic zones defined during fieldwork (Fig. 11). Because the thresholded error (LoD_{min}) is likely a conservative estimate, both the thresholded and raw DoD elevation changes were computed and analyzed to describe geomorphic change. The boundaries of the ecogeomorphic zones were defined by the extent of the August 2020 orthophotos and the transects used in DSAS analyses. After

defining the zone area, the 2015 OMHW contour was used to separate the subaqueous and subaerial regions. Each DoD was cropped to include only the area measured by the individual DEMs used to generate the DoDs to study that particular zone. For example, if the 2011, 2015 and September 2018 datasets were used in volumetric calculations, only the areas in common between all three surveys were used in measurement to ensure an accurate comparison (Fig. 18).

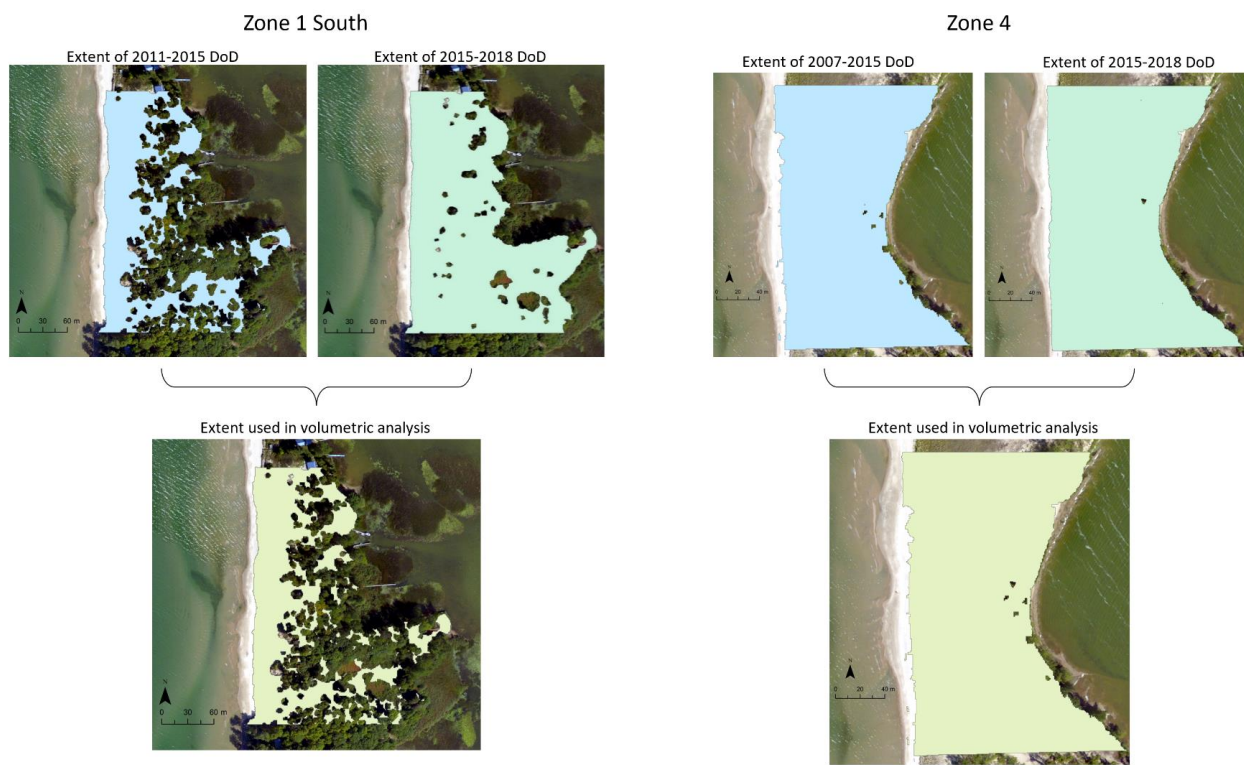


Figure 18. Extent of DoDs used to determine the region used for volume calculation of each individual zone. The pre-high water DoD coverage heavily impacted the area included in volumetric analysis depending on coverage. Coverage from the more recent DoD is much higher at Zone 1 South (left) while there is little difference in the coverage of the two DoDs at Zone 4 (right).

The elevation values of the DoD raster were exported for further analysis in MATLAB to quantify the amount and type (erosion or deposition) of change. Map

products were made from the DoD to show spatial distribution and magnitude of volumetric change. All seven zones were analyzed for the 2007-2015 and 2015-2018 interval. The 2020 dataset was not included because of the inability to filter out vegetation in the SfM DEMs. Cell values of elevation change, once imported into MATLAB were used to calculate six volume values: (1) raw volume of erosion (V_e); (2) raw volume of deposition (V_d); (3) raw net volumetric change (V_n); (4) significant or thresholded volume of erosion (sV_e); (5) thresholded volume of deposition (sV_d); and (6) thresholded net volume change (sV_n).

When calculating the raw volume change (V_e, V_d, V_n), all cell values were included, however when calculating the thresholded volumetric change (sV_e, sV_d and sV_n), values within the interval $[-LOD_{min}, LOD_{min}]$ were excluded to isolate statistically significant change. Calculations for each of the six volume values are included below, where Δ_e is the change in elevation, d is the cell area of the DoD, and N is the number of cells with the defined changes in elevation (Wheaton et al., 2010; Le Mauff et al., 2018; Lallias-Tacon et al., 2014). Erosion and deposition volume values were negative, and positive, respectively:

$$V_e = \sum(\Delta_e < 0) \times d \times N \quad (6)$$

$$V_d = \sum(\Delta_e > 0) \times d \times N \quad (7).$$

Raw net volume change was calculated as the sum of V_e and V_d :

$$V_n = V_e + V_d \quad (8).$$

Statistically significant volume change was calculated using the LOD_{min} :

$$sV_e = \sum(\Delta_e < -LOD_{min}) \times d \times N \quad (9)$$

$$sV_d = \sum(\Delta_e > LOD_{min}) \times d \times N \quad (10)$$

$$sV_n = sV_e + sV_d \quad (11).$$

The margin of error for all six volumetric calculations was calculated as the product of the area covered by the cells used in calculation and the error of said DoD (E_{DoD}) such that:

$$\text{margin of error} = \text{Area} \times E_{DoD} \quad (12).$$

The purpose of applying LOD_{min} is to isolate the statistically significant change, which more accurately describes the amount and type of change to the SPS.

7. Results

7.1 Shoreline analysis. The magnitude and rate of shoreline migration depend on the interval studied and location along the barrier spit (Fig. 19). In terms of location, the largest magnitudes of shoreline migration were located in the inlet region. As the inlet migrates north, the south side of the inlet aggrades and advances, and the shoreline north side of the inlet retreats. This results in high magnitude, positive net shoreline movement (NSM) and rate of shoreline change (RSC) south of the inlet, and negative to the north (Fig. 19 and 20). Because the net mean RSC is easily influenced by outliers such as those in the inlet region, the “adjusted mean” is introduced. The adjusted mean is the RSC for all transects cast outside of the inlet region where the barrier is stable and straight (Table 9).

During the 2001-2015 interval, prior to the high-water events, the SPS was net depositional with a net and adjusted mean RSC of 0.25 ± 0.03 m/year and 0.12 ± 0.03

m/year, respectively (Table 9). On average, the shoreline advanced 3.62 m at a given transect and 55.22% of the transects measured advance (Table 10).

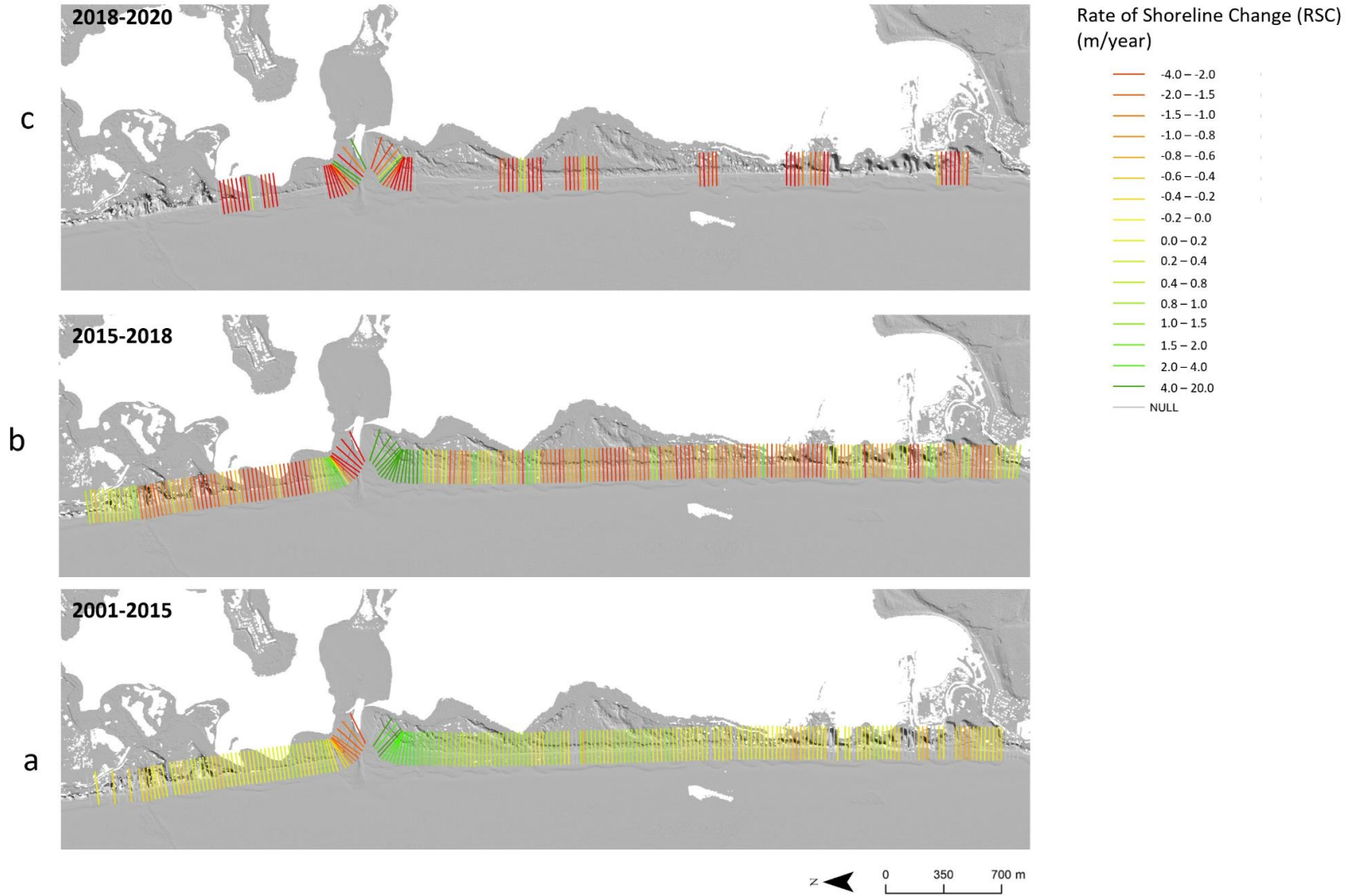


Figure 19. DSAS results for the rate of shoreline change (RSC) during the 2001-2015, 2015-2018, and 2018-2020 intervals.

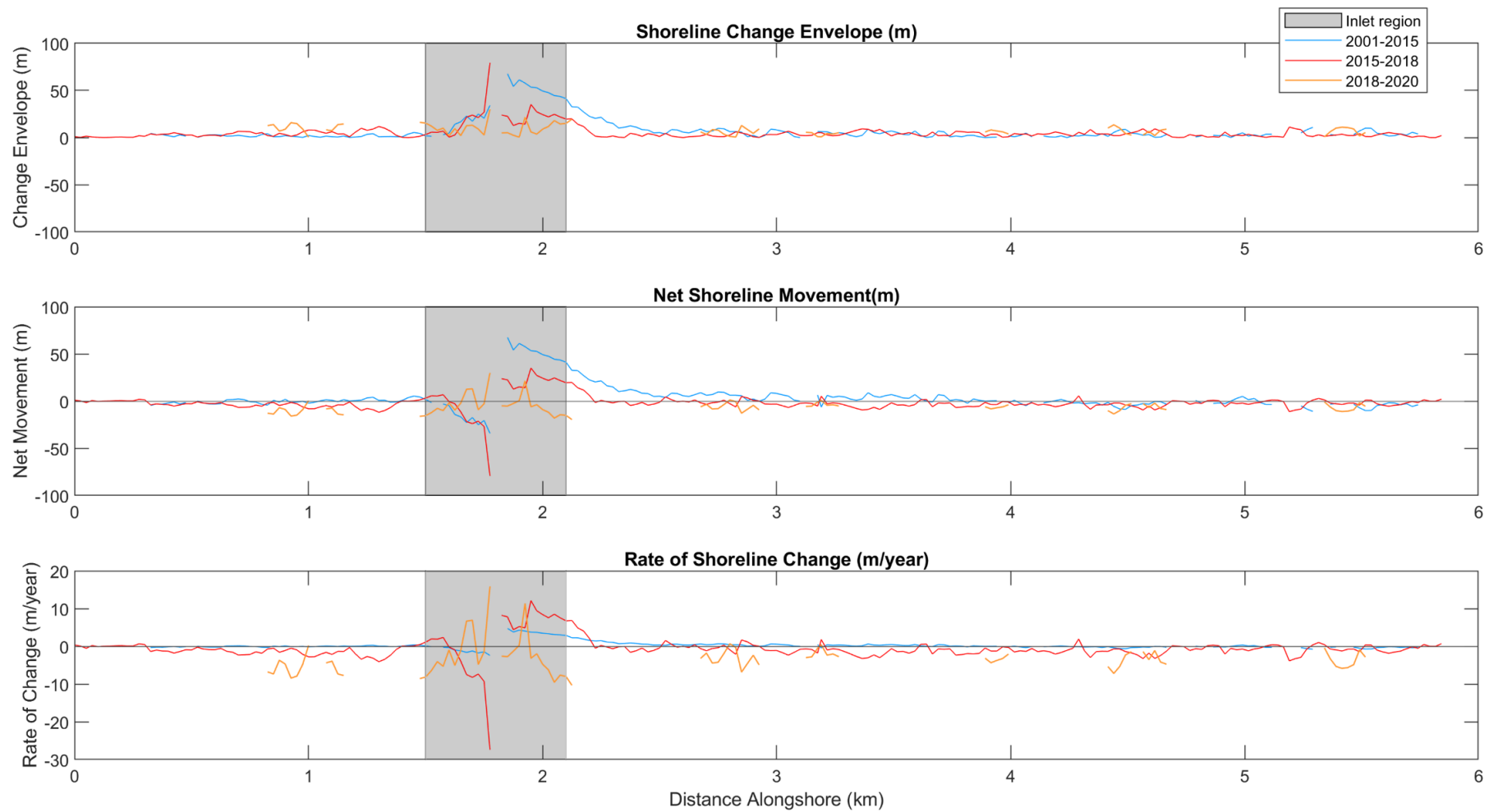


Figure 20. Summary of alongshore DSAS analysis results. Positive change indicates deposition, and negative, erosion. The inlet region, shaded gray, represents transects surrounding the channel and includes data omitted in the adjusted mean calculations.

From 2015- September 2018 the SPS was erosional with a net and adjusted mean RSC of -0.62 ± 0.13 m/year and -0.86 ± 0.13 m/year, respectively (Table 9). The average net shoreline migration was 1.81 m and 72% of the transects measured shoreline retreat (Table 10).

Table 9. Summary of the average rate of shoreline including (net) and omitting (adjusted) the inlet region. The uncertainty calculation used a 95% confidence interval.

	Rate of Shoreline Change (m/year)	
	Net mean	Adj. mean
2001-2015	0.25 ± 0.03	0.12 ± 0.03
2015-2018	-0.62 ± 0.13	-0.86 ± 0.13
2018-2020	-3.27 ± 0.12	-3.79 ± 0.12

The 2018-2020 interval values are computed from fewer transects due to the limited coverage of 2020 surveys. The previous two intervals used 201 and 234 transects in their calculations; the 2018-2020 interval used 81 transects (Table 10). Results are thus influenced by the smaller sampling size. The mean distance of shoreline movement from 2018-2020 was -6.15 m and 90% of the transects recorded erosion (Table 10). The net and adjusted mean RSC were -3.27 ± 0.12 m/year and -3.79 ± 0.12 m/year, respectively (Table 9). Nearly all the transects recorded a rate of more than 2 m/year of shoreline retreat and erosion was predominately recorded on the southern side of the channel inlet (Fig. 19 and 20)

Table 10. Summary of DSAS analysis results describing shoreline migration. Three statistics are included in DSAS summary reports: shoreline change envelope (SCE), net shoreline movement (NSM), and end point rate (EPR) (Himmelstoss et al., 2018). SCE refers to the net change in the shoreline distance at a transect regardless of time and direction. NSM is the net shoreline movement between the earliest shoreline and the most recent shoreline. EPR uses the NSM and computes a rate in m/year to describe the rate at which the shoreline is moving. Three shorelines are used in the analysis below: 2001, 2015, and September 2018.

Shoreline Change Envelope (SCE)			
Time Interval (No. of transects)	Mean dist. (m)	Max dist. (m)	Min dist. (m)
2001-2015 (201)	7.61	67.65	0
2015- Sept 2018 (234)	5.18	79.28	0
Sept 2018-Aug 2020 (81)	8.13	30.01	0.45
2001-Aug 2020 (73)	22.27	93.47	0.19

Net Shoreline Movement (NSM)					
Time Interval (No. of transects)	Mean dist. (m)	No. of erosional transects (%)	Max neg. dist. (m) (mean neg. change in distance (m))	No. of depositional transects (%)	Max pos. dist. (m) (mean pos. change in distance (m))
2001-2015 (201)	3.62	90 (44.78%)	-34.14 (-4.45)	111 (55.22%)	67.65 (10.17)
2015- Sept 2018 (234)	-1.81	169 (72.22%)	-79.28 (-4.83)	65 (27.78%)	35.13 (6.07)
Sept 2018- Aug 2020 (81)	-6.15	73 (90.12%)	-19.46 (-7.93)	8 (9.88%)	30.01 (10.03)
2001- Aug 2020 (73)	-0.43	56 (76.71%)	-83.41 (-14.79)	17 (23.29%)	93.47 (46.88)

Rate of Shoreline Change (RSC)						
Time Interval (No. of transects)	Average rate of change (m/yr)	Max rate of erosion (m/yr)	avg rate of erosion (m/yr)	Max rate of accretion (m/yr)	Average rate of accretion (m/yr)	
2001-2015 (201)	0.25 ±0.03	-2.4	-0.31	4.75	0.71	
2015- Sept 2018 (234)	-0.62 ±0.13	-27.4	-1.67	12.14	2.1	
Sept 2018-Aug 2020 (81)	-3.27 ±0.12	-10.31	-4.21	15.9	5.31	
2001- Aug 2020 (73)	-0.02 ±0.02	-4.39	-0.78	4.91	2.47	

7.2 *Foredune crest position and elevation.* There are two distinct scenarios under which the horizontal and vertical position of the foredune changed throughout the study site after experiencing a high-water summer event. The type and magnitude of foredune change depended on the location along the barrier, antecedent topography, and proximity to the shoreline (i.e., horizontal erosion, dune collapse, etc.). In the first scenario, (S1), the foredune crest moved east, and decreased in elevation due to erosion of the lakeward side of the foredune (Fig. 21). In the second scenario (S2), the foredune crest moved west and decreased in elevation, due to deposition of a new foredune (Fig. 22). Changes in position of the foredune crest were coupled with changes in the shoreline position due to of the beach at the dune toe.

Zone 1 North and Zone 4 are examples of locations where S1 occurred (Fig. 11). Under these conditions, lateral migration of the foredune east was caused by erosion on the western side of the dune, which moved the foredune crest to a position that was previously on the back-barrier side of the dune (Fig. 21). These locations have high

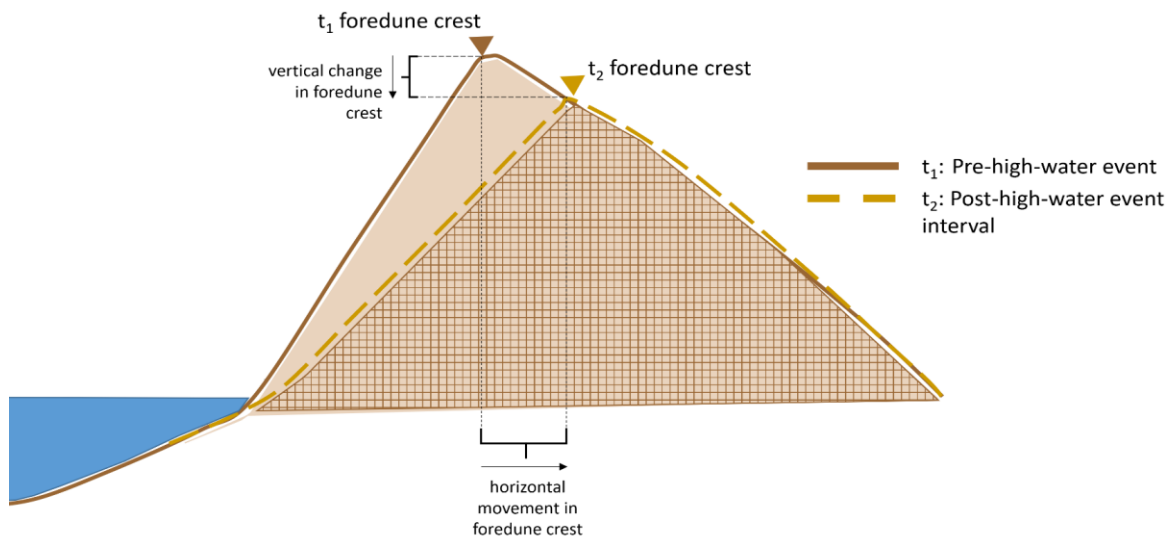


Figure 21. Illustration of scenario 1 (S1) showing a decrease in elevation and landward movement of the foredune.

magnitude rates of shoreline retreat which drove the lateral movement of the foredune due to erosion of the dune toe (Fig. 23a and 23e). The inflection point on the 2020 profile at the dune toe is aligned with the monthly high-water level for 2017 and 2019 before gently sloping lakeward to the 2020 monthly high-water level near the OMHW. Net lateral retreat of the cross-shore profile at the monthly high-water level of 2019 from 2015-Aug 2020 is roughly 15.5 m (Fig. 23a).

Zone 1 South and Zone 3 demonstrate S2, where a new low relief foredune formed lakeward of the previous (Fig. 22 and Fig. 23b). At Zone 3 this was due to new bars suturing to the recurved spits near the channel (Fig. 23d). This additionally occurred at other locations along the spit with higher relief such as Zone 7 (Fig. 23h). Transect profiles extracted at each zone indicate the natural variation in the profile and the change in position of the foredune crest throughout the study period (Fig. 23a-h).

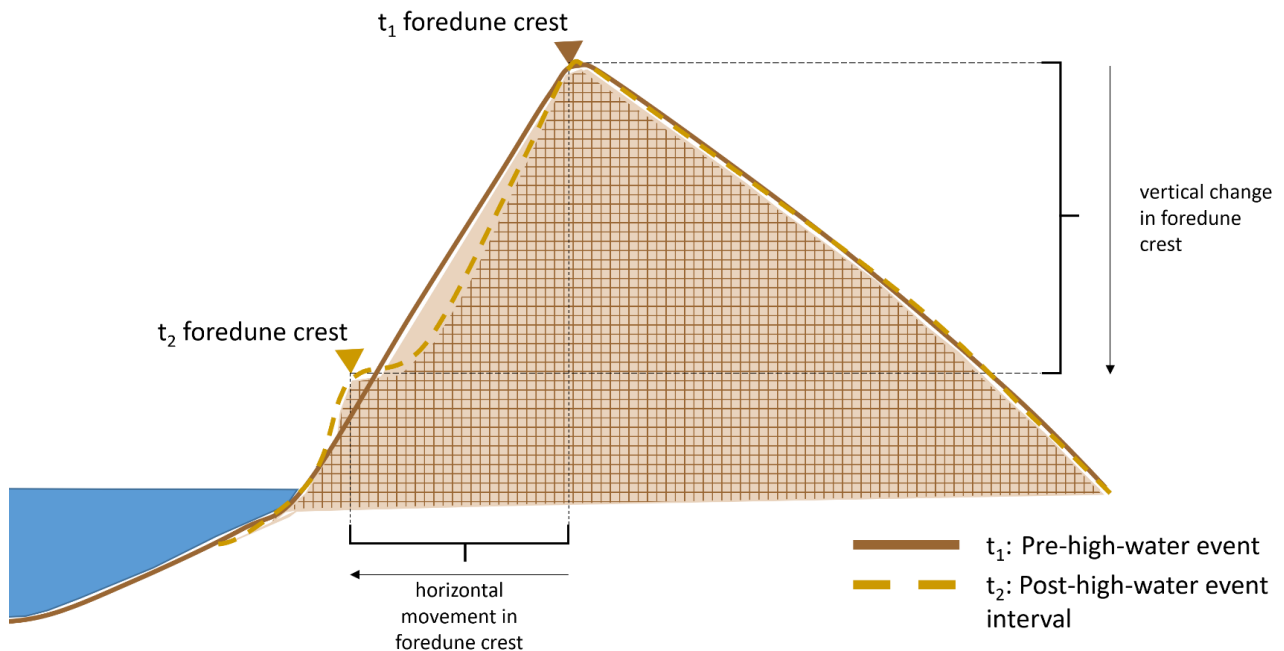


Figure 22. Illustration of scenario 2 (S2) showing a decrease in the elevation and lakeward movement of the foredune.

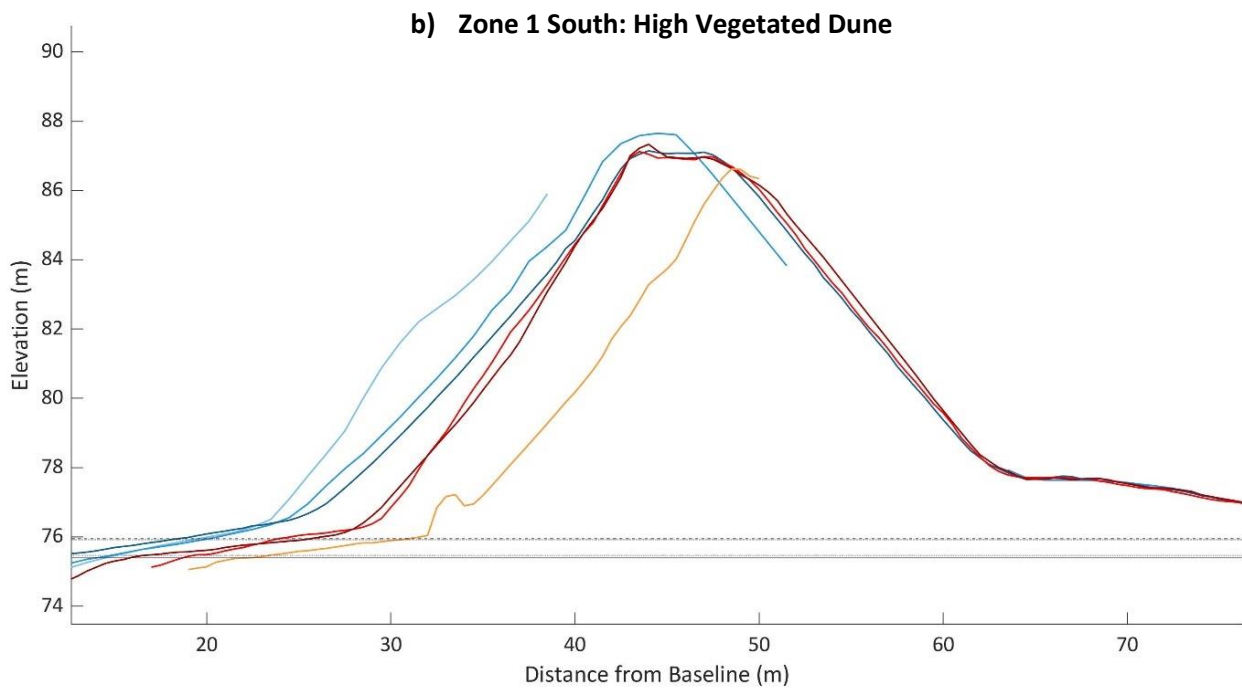
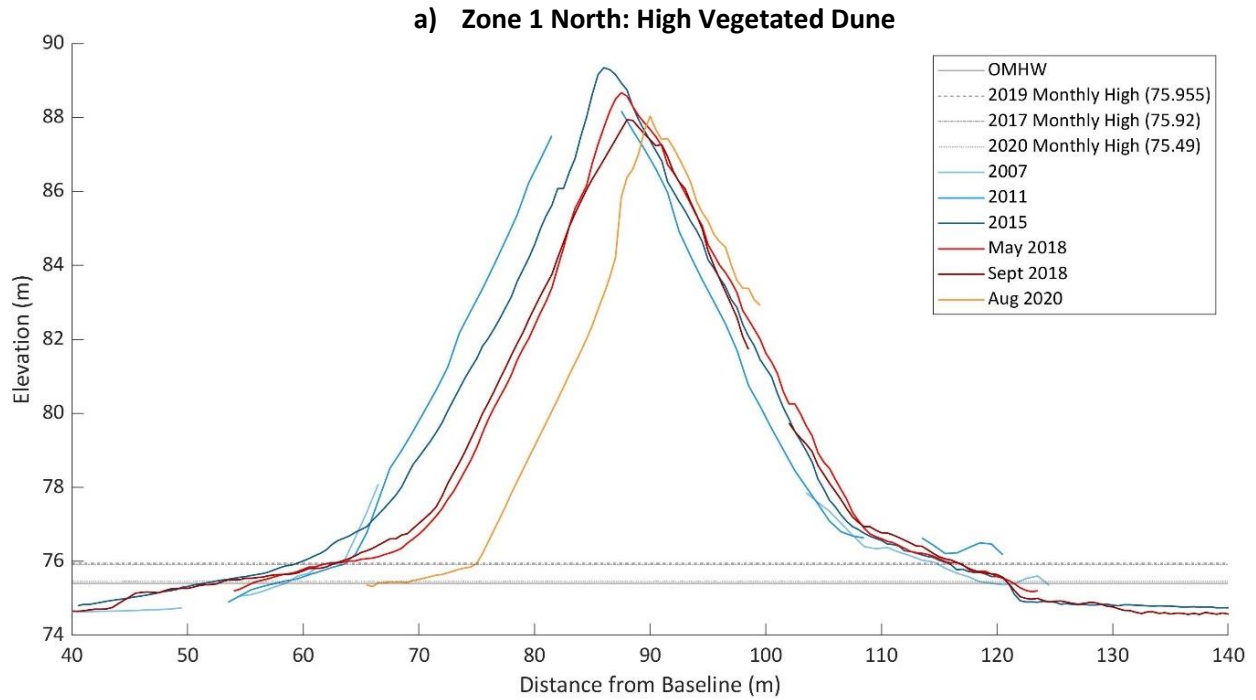
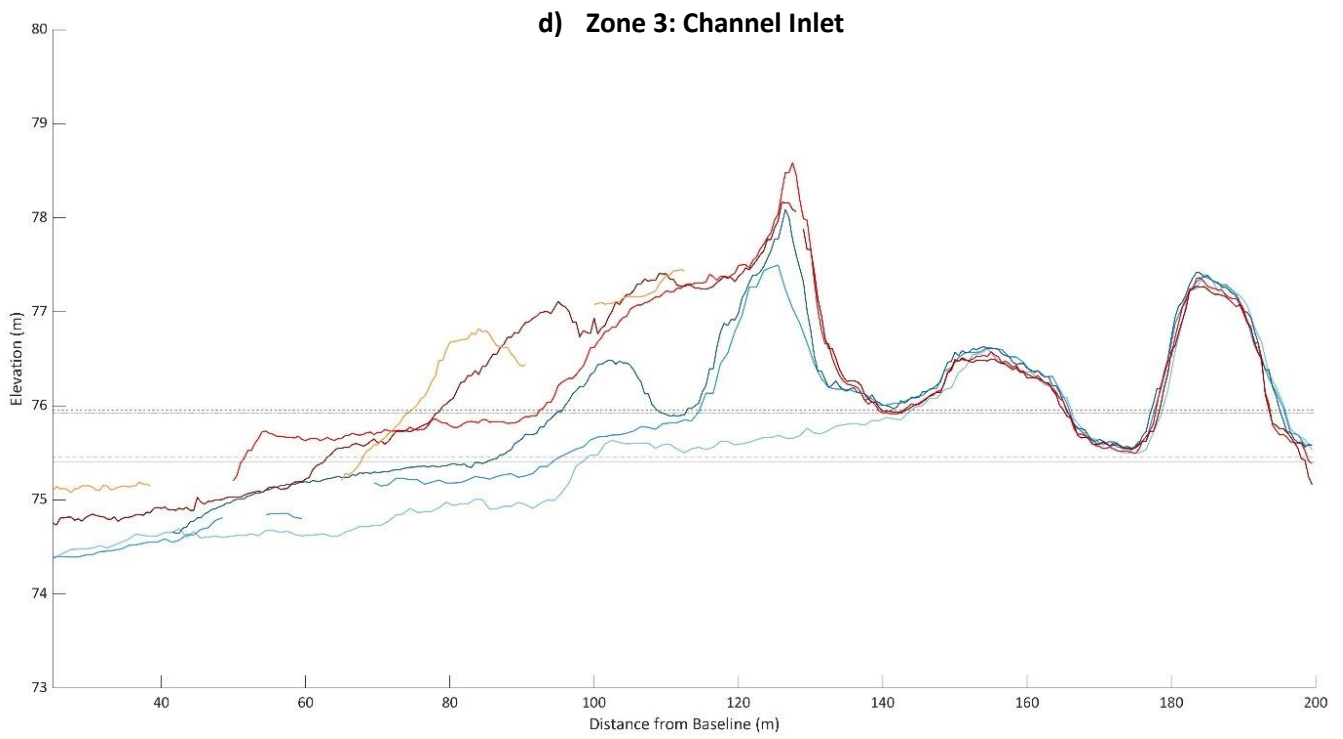
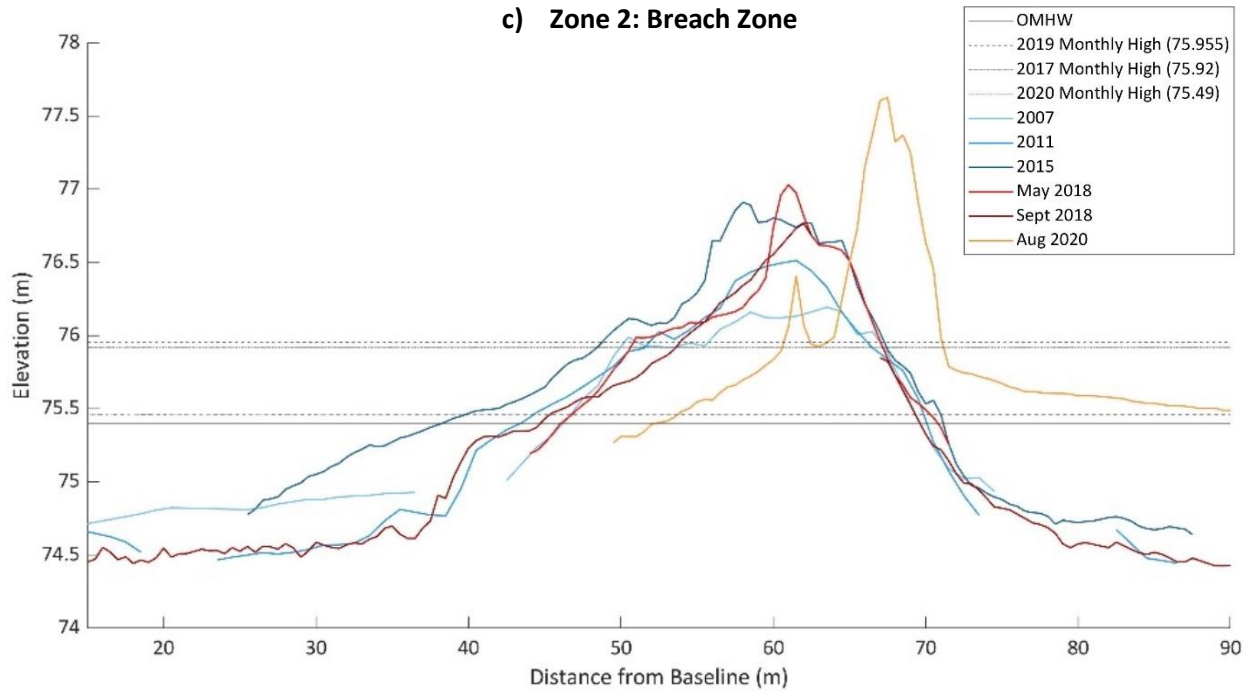
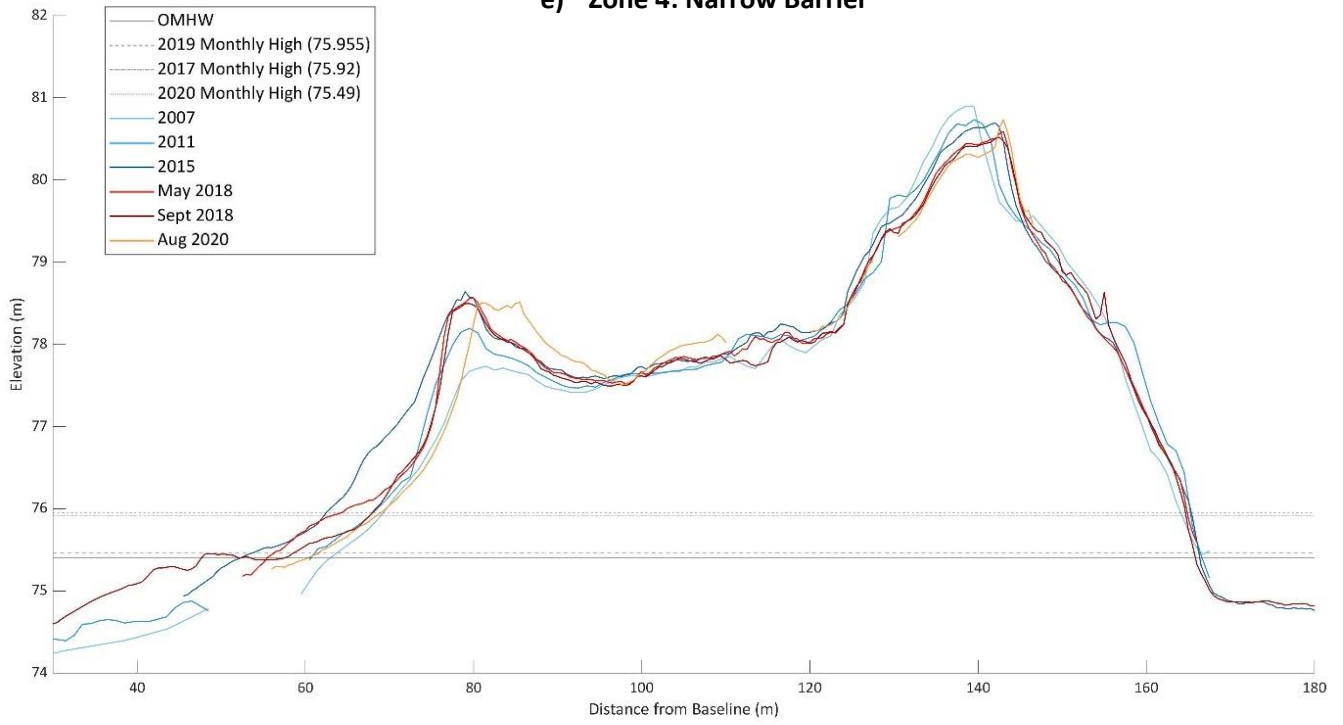


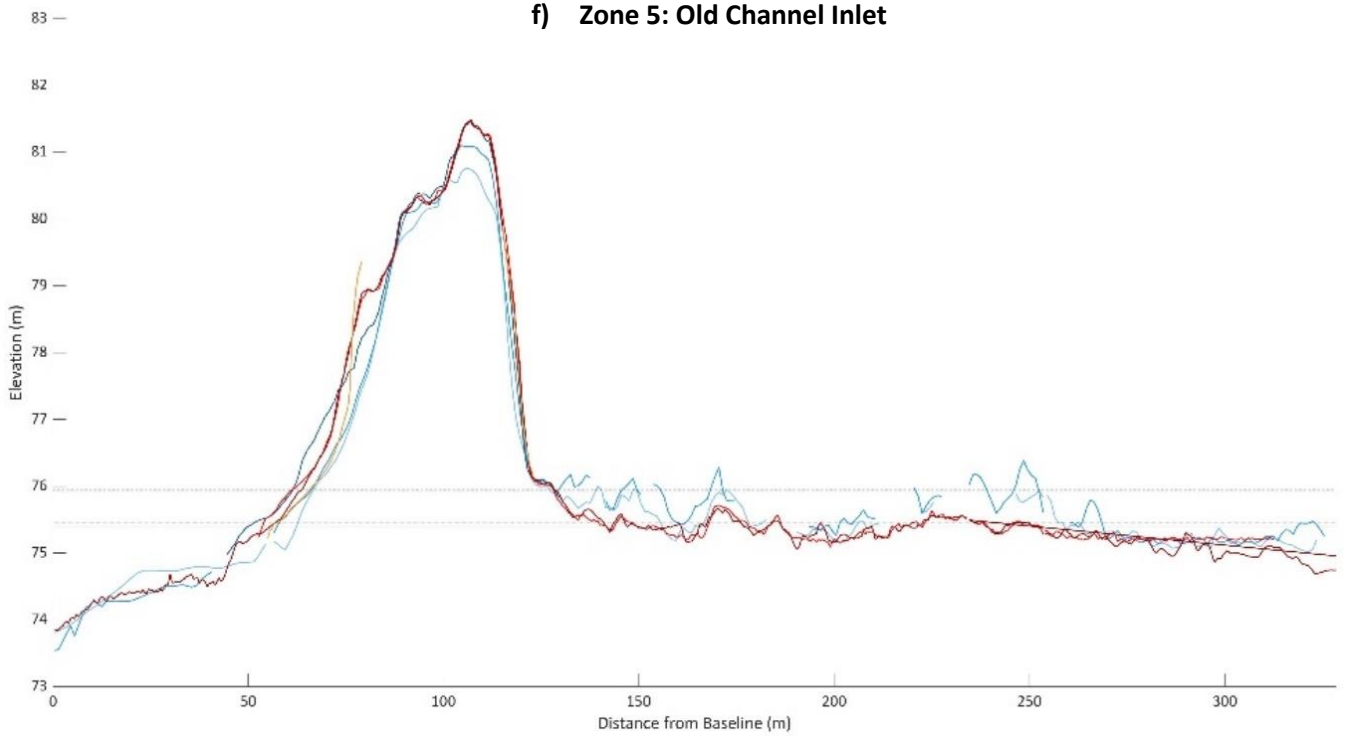
Figure 23 a-h. Cross-barrier topographic profiles of the barrier at each zone for each dataset within the study period. One representative transect is used to represent each of the eight flight zones. Continues on the next two pages (a-h). The monthly high water levels for the summer of 2017, 2019, and the OMHW elevation are provided for reference and to demonstrate the effect of water level on the beach profile.

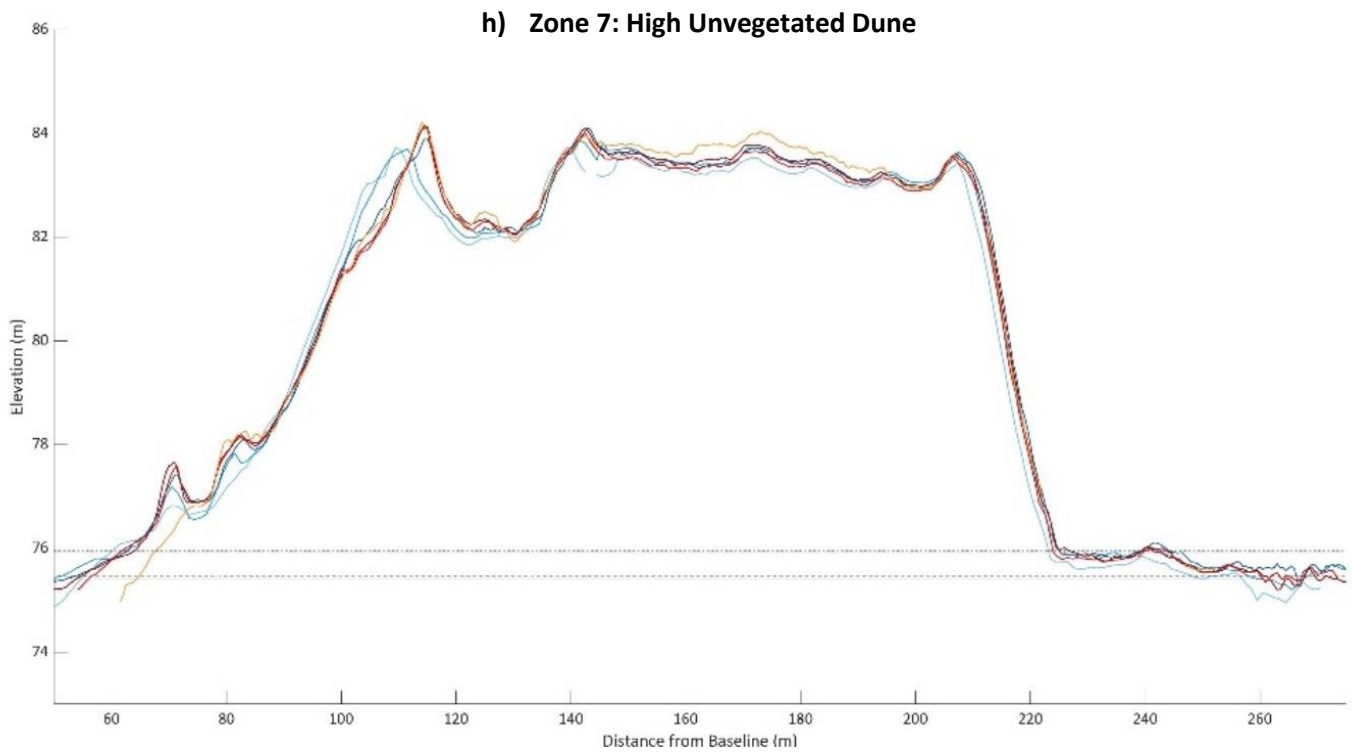
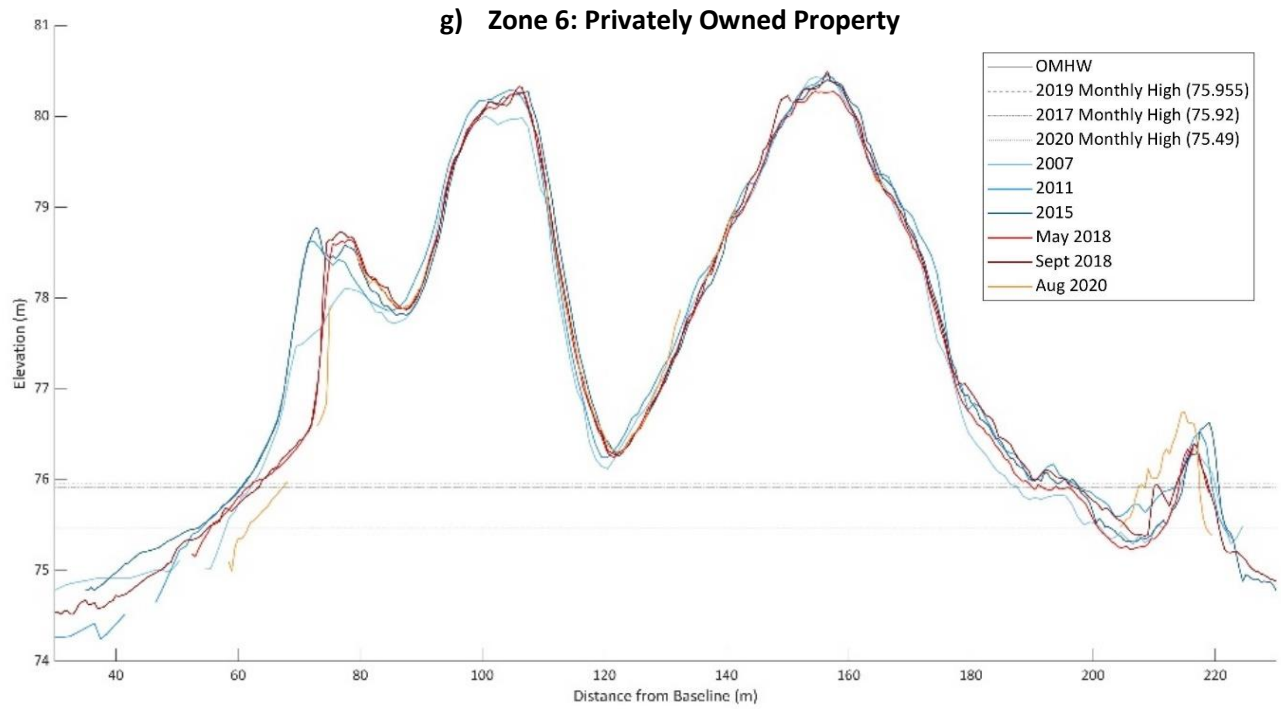


e) Zone 4: Narrow Barrier



f) Zone 5: Old Channel Inlet





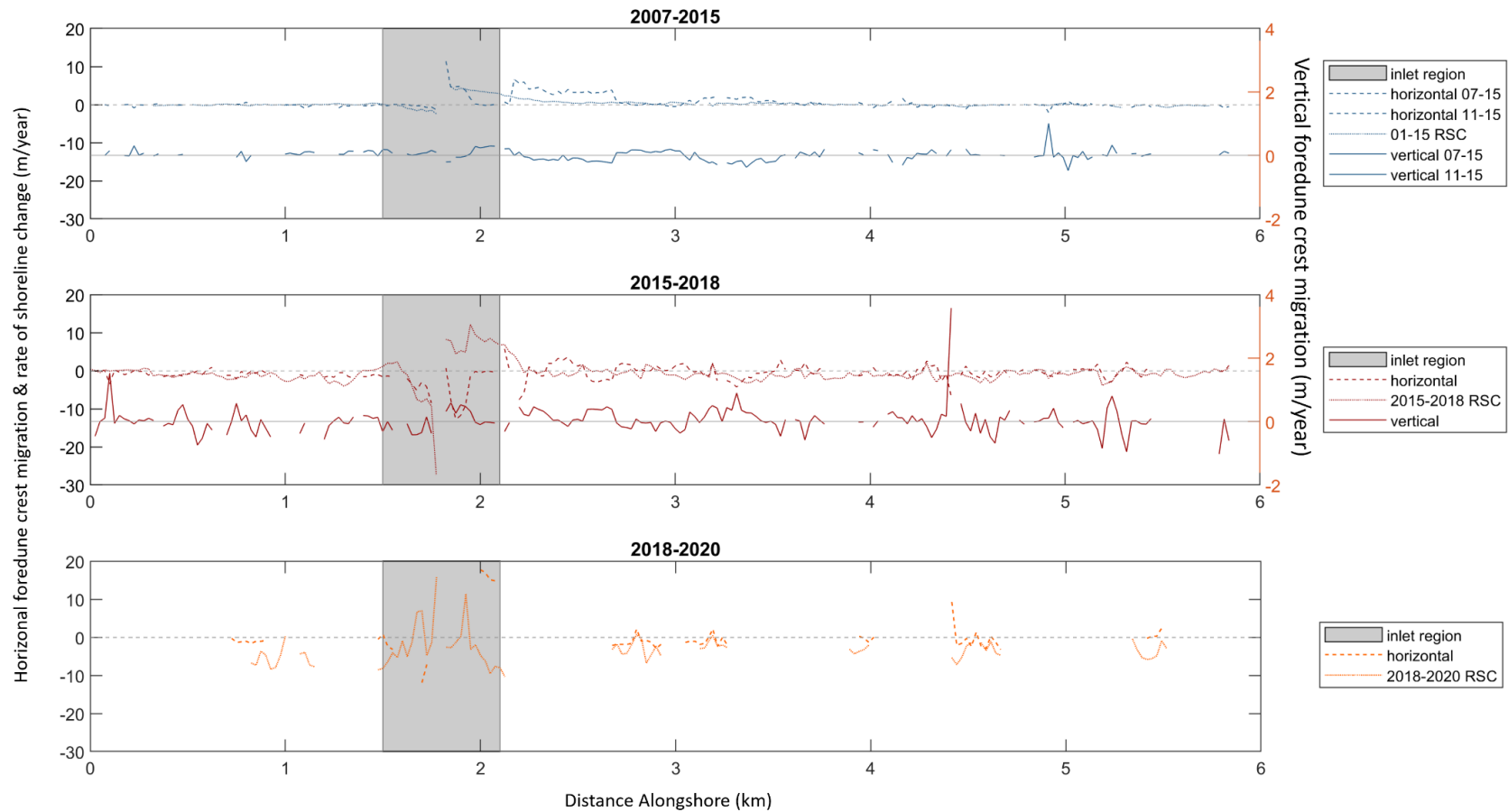
In terms of alongshore variation, the foredune migrated laterally an average of 6.66 m and 1.85 m west during the 2007-2015 and 2011-2015 intervals, respectively (Table 11). A little over half of the 181 transects measured lakeward movement. The average rate of change for 2007-2015 and 2011-2015 foredunes was 0.81 ± 0.04 m/year and 0.45 ± 0.09 m/year lakeward, respectively (Table 11). From 2015-2018 the mean horizontal migration was 2.33 m east (landward) measured from 191 transects. Two thirds of the transects measured landward migration at a mean rate of change of 0.80 ± 0.13 m/year (Table 11). The 2018-2020 interval recorded 0.18 m of foredune migration west (lakeward) over the 57 transects measured. This interval had the highest (72%) number transects measuring landward foredune crest movement but had an average rate of 0.09 ± 0.12 m/year west (lakeward).

Because the lateral and vertical foredune migration and shoreline migration are closely interrelated and vary throughout the study site, data are combined to study alongshore variation in the position of the shoreline, vertical foredune crest and horizontal foredune crest (Fig. 24). As explained previously, the direction of shoreline and foredune crest migration are the same in most cases, however the rate of varied greatly. Compared to the 2015-2018 interval, the vertical change in foredune crest was lower magnitude and less variable from 2007-2015 (Fig. 24). The 2018-2020 variation in vertical foredune change was not studied because of the inability to generate bare earth DEMs.

Table 11. Summary of DSAS analysis results describing lateral foredune crest migration. Three statistics are included in DSAS summary reports: horizontal foredune change envelope, net foredune horizontal movement, and rate of foredune horizontal migration (Himmelstoss et al., 2018). FCE refers to the net change in the horizontal position of the foredune crest. NFM is the net foredune crest movement between the earliest and the most recent foredune crest position in the studied interval. RFM uses the NFM and computes a rate in m/year to describe the rate the foredune crest has moved.

<i>Foredune Horizontal Change Envelope</i>					
Time Interval (No. of values)	Mean dist. (m)	Max migration distance (m)	Min migration distance (m)		
2007-2015 (138)	9.08	54.5	0		
2011-2015 (42)	3.23	46.5	0		
2015- Sept 2018 (191)	4.35	37.0	0		
Sept 2018-Aug 2020 (57)	5.4	33.5	0		
<i>Net Foredune Horizontal Movement</i>					
Time Interval (No. of values)	Mean dist. (m)	No. of landward transects (%)	Max landward dist. (m) (mean neg. change in distance (m))	No. of lakeward transects (%)	Max lakeward dist. (m) (mean pos. change in distance (m))
2007-2015 (138)	6.66 W	59 (42.75%)	11.00 (2.84)	79 (57.25%)	54.5 (13.75)
2011-2015 (42)	1.85 W	19 (45.24%)	8.5 (1.53)	23 (54.76%)	46.5 (4.63)
2015- Sept 2018 (191)	2.33 E	127 (66.49%)	37 (5.02)	64 (33.51%)	16.5 (3.02)
Sept 2018-Aug 2020 (57)	0.18 W	41 (71.93%)	22.5 (3.63)	16 (28.07%)	33.5 (9.94)
<i>Rate of Foredune Horizontal Migration</i>					
Time Interval (No. of values)	Average rate of change (m/yr)	Max rate of landward migration (m/yr)	Average rate of landward migration (m/yr)	Max rate of lakeward migration (m/yr)	Average rate of lakeward migration (m/yr)
2007-2015 (138)	0.81 ±0.04 Lakeward (W)	1.33	0.34	6.61	1.67
2011-2015 (42)	0.45 ±0.09 Lakeward (W)	2.08	0.37	11.36	1.13
2015- Sept 2018 (191)	0.80 ±0.13 Landward (E)	12.79	1.72	5.7	1.04
Sept 2018-Aug 2020 (81)	0.09 ±0.12 Lakeward (E)	11.92	1.93	17.75	5.27

Figure 24. Alongshore horizontal and vertical migration of the foredune crest plotted with the rate of shoreline change (RSC) calculated during DSAS analysis during the 2007-2015, 2015-2018, and 2018-2020 intervals. The inlet region is shaded in grey. Zero change is displayed as a reference. More variation in the foredune position is measured from 2015-2018 compared to 2007-2015.



7.3 *Volumetric change.* The following describes the volumetric change at each of the seven ecogeomorphic zones using DoDs and cross-shore profiles. From 2007-2015, before the high-water events, the statistically significant and raw net volumetric changes were depositional at all zones except Zone 1 North and South, which contains the highest relief (Table 12). The most deposition occurred at Zone 3, the inlet region, and the least in Zone 7, the sparsely vegetated high relief dunes (Table 12). From 2015-2018, the SPS was net erosional for all thresholded volumetric calculations in all seven zones. The highest magnitudes of erosion occurred in Zone 1 South and the lowest in Zone 5 (old channel location) (Table 12). Erosion was concentrated on the lakeward facing beach slope. The erosion of the foredune appeared to coincide with the maximum lake level of each summer (Fig. 23).

Because SfM did not allow for reliable DoDs of the 2018-2020 interval, the cross-shore profiles and orthoimages are used to interpret volumetric change during this interval. Zones 1 and 4-6 show extensive, ongoing erosion of the west side of the foredune (Fig. 23).

Orthoimages of Zone 2 show the formation of two subaerial washover fans on the back barrier side of the spit



Figure 25. August 2020 orthophotograph of Zone 2 showing overwash fans. The 2020 and 2018 OMHW shorelines are shown in orange and red, respectively.

(Fig. 25). These accumulations are low relief but remained exposed throughout the summer of 2021. From 2007-2015 the net significant change in all seven zones was $21,035 \pm 10,711 \text{ m}^3$ of deposition. From 2015-2018 the net significant change of all zones was $14,771 \pm 6,369.6 \text{ m}^3$ of erosion.

Table 12. Summary of volumetric changes measured by DoDs at each zone including deposition, erosion and net change. Thresholded volume measurements use a 95% confidence interval to isolate significant change

	Volume of Deposition (m ³)				Volume of Erosion (m ³)				Net Volume Change (m ³)			
	Raw	± Error	Thresholded	± Error	Raw	± Error	Thresholded	± Error	Raw	± Error	Thresholded	± Error
<i>2007-2015</i>												
Zone 1 North 2011-2015	1,525.4	1,586.7	649.3	227.8	-1,829.5	1,097.0	-1,308.4	359.1	-304.1	2,683.8	-659.1	586.9
Total Area	4277.0		614.0		2,957.0		968.0		7,234.0		1582.0	
Zone 2 2007-2015	2,353.1	2,463.4	660.4	240.3	-186.3	331.9	-24.6	9.9	2,166.8	2,795.3	635.8	250.2
Total Area	6,694.0		653.0		902.0		27.0		7,596.0		680.0	
Zone 3 2007-2015	22,713.0	18,289.2	15,501.3	4,772.6	-2923.6	5,644.8	-1,044.1	322.0	19,789.4	23,934.0	14,457.2	5,094.6
Total Area	49,699.0		12,969.0		15339.0		875.0		65,038.0		13,844.0	
Zone 4 2007-2015	8,946.6	8,234.0	4,131.5	1,508.1	-1450.3	2,744.0	-322.9	108.9	7,496.3	10,978.5	3,808.6	1,617.0
Total Area	22,375.0		4,098.0		7457.0		296.0		29,833.0		4,394.0	
Zone 5 2007-2015	7,293.0	5,794.9	3,712.6	1,331.1	-1,513.3	3,339.6	-18.2	8.5	5,779.7	9,134.9	3,694.4	1,339.5
Total Area	15,747.0		3,617.0		9,075.0		23.0		24,823.0		3,640.0	
Zone 6 2007-2015	4,632.6	5,431.7	1,806.8	496.1	-689.7	2,744.2	-60.7	19.9	3,942.9	7,246.7	1,746.1	515.9
Total Area	14,760.0		1,348.0		4932.0		54.0		19,692.0		1,402.0	
Zone 1 South 2011-2015	1,957.7	2,855.6	675.8	247.8	-6074.0	5,194.7	-3,483.8	952.4	-4,116.4	8,050.7	-2,808.0	1,200.2
Total Area	7,697.0		668.0		14002.0		2,657.0		21,700.0		3,335.0	
Zone 7 2011-2015	2,207.2	8,748.9	199.00	90.20	-2853.0	2,510.9	-38.7	17.1	-645.8	12,108.3	160.3	107.2
Total Area	23,582.0		243.00		6768.0		46.0		32,637.0		289.0	
<i>2015-2018</i>												
Zone 1 North 2015-2018	580.7	756.9	233.1	88.8	-2,970.4	1,883.8	-2,208.4	577.0	-2,389.7	2,640.8	-1,975.3	665.8
Total Area	2,068.0		242.1		5,147.0		1,576.5		7,215.3		1,819.0	
Zone 2 2015-2018	131.1	469.7	0.2	0.1	-2620.7	2,302.6	-1,207.3	383.7	-2489.5	2,772.3	-1,207.2	383.8
Total Area	1,283.3		0.3		6291.3		1,048.3		7574.5		1,048.5	
Zone 3 2015-2018	10,262.0	9,188.3	5,483.3	1,689.9	-13621.6	14,483.3	-9806.1	1,777.8	-3359.5	23,672.0	-4,322.9	3,467.7
Total Area	25,104.8		4,617.3		39571.8		4,857.3		64677.5		9,474.5	
Zone 4 2015-2018	855.5	2,918.1	30.9	11.5	-3719.7	7,959.9	-367.1	126.1	-2864.2	10,878.2	-336.2	137.6
Total Area	7,973.0		31.5		21,748.3		344.5		29,721.8		376.0	
Zone 5 2015-2018	825.9	2,471.9	6.4	3.0	-2381.2	6,688.7	-112.3	49.6	-1555.2	8,995.8	-105.8	52.6
Total Area	6,753.8		8.3		18275.0		135.5		24,578.8		143.8	
Zone 6 2015-2018	1,203.1	3,959.0	65.8	26.4	-1,457.7	3,236.5	-440.4	133.5	-254.6	7,195.7	-375.6	159.9
Total Area	10,817.0		72.0		8,843.0		364.8		19,660.3		436.8	
Zone 1 South 2015-2018	1,007.2	2,472.0	69.9	27.3	-8801.8	5,208.5	-6,512.5	1,453.2	-7794.5	7,680.8	-6,442.6	1,480.5
Total Area	6,754.0		74.5		14231.0		3,970.5		20,985.8		4,045.0	
Zone 7 2015-2018	2,179.5	5,599.9	20.4	8.7	-1835.0	6,323.7	-26.3	13.0	344.5	11,924.1	-5.8	21.7
Total Area	15,300.3		23.8		17278.0		35.5		32,579.5		59.3	

7.3.1 *Zone 1 North*. Zone 1 has two survey locations, one on the northern spit, and the other on the southern spit (Fig 11). The zone includes the highest relief dunes which are densely vegetated with trees and grasses landward from the primary dune crest, stabilizing the back-barrier region. The lakeward-facing dune scarp is exposed dry sand and the primary dune crest is also the foredune (Fig. 23a-b). From 2007-2020 the dune progressively retreated landward (east), even though the back of the dune remained stable, minimally accreting from 2007-2015. The greatest amount of erosion, as indicated by retreat between successive profiles, is from 2018-2020, which surpasses that of 2007-2015 and 2015-2018, both longer periods.

Volumetric change in the northern Zone 1 study site was net erosional during all intervals (Table 12). Deposition was concentrated on the back of the dune, east of the foredune crest (Fig. 26) . From 2011-2015 $1,525.4 \pm 1,586.7 \text{ m}^3$ of raw deposition and $-1,829.5 \pm 1,097.0 \text{ m}^3$ of raw erosion were measured resulting in a raw net erosional volume change of $304.1 \pm 2,647.6 \text{ m}^3$ (Fig. 26; Table 12). After applying the LoD_{min} of 0.728 m, it was evident the statistically significant change was confined to the backbarrier regions and dune face (Fig. 26). Deposition measured on the beach was not significant. During the 2015-2018 interval the area of erosion increased, and the area of deposition decreased (Fig. 26; Table 12). The volumetric change became increasingly erosional, increasing by a factor of nearly three for statistically significant net change (Table 12).

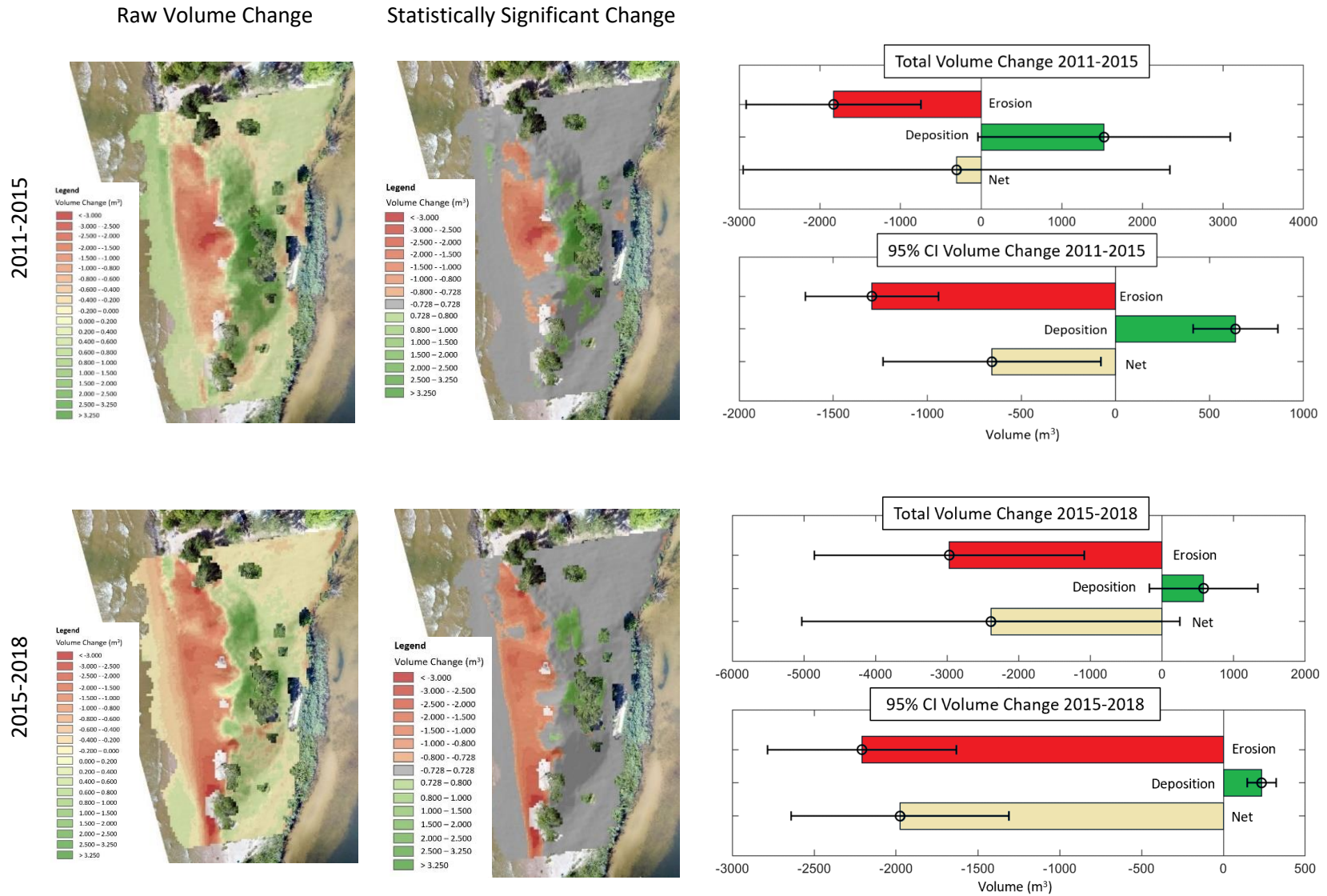


Figure 26. Zone 1 North 2011-2015 and 2015-2018 DoDs with volumetric change calculations. Volumetric change within the LOD_{min} is shaded grey and is not statistically significant. Histograms show the volume of change measured and the associated error.

7.3.2 *Zone 1 South*. To the south, a similar pattern of change exists (Fig. 23b). From 2007- 2020 the dune laterally retreated 11.5 m. The foredune crest decreased in elevation and moved slightly landward from 2011-2015 before stabilizing and increasing vertically from 2015-2018. The 2020 foredune crest was west of the previous location at the top of a small pile of riprap, placed after the high-water summer of 2017. Again, the dune toe of the 2020 profile aligned with the monthly high-water level in 2017 and 2019 (Fig. 23b).

From 2011-2015, the net significant volumetric change measured 2,808.0 \pm 1,200.9 m³ of erosion and from 2015-2018 measured 6,442.6 \pm 1,480.5 m³ of net erosion (Table 12). This region experienced the most erosion during the pre-high water event interval, measuring roughly 4.2 times more statistically significant erosion than the only other net erosional zone, Zone 1 North. Like Zone 1 North, deposition was isolated to some backbarrier regions, however most of it was not statistically significant. Most of the erosion on the slope of the dune facing the lake was concentrated to the southern part of the study area (Fig 27). Compared to the first interval, a higher magnitude of erosion was distributed along the entire lakeward facing slope of the dune from 2015-2018. There were no large areas of deposition on the back of the dune (Fig. 27).

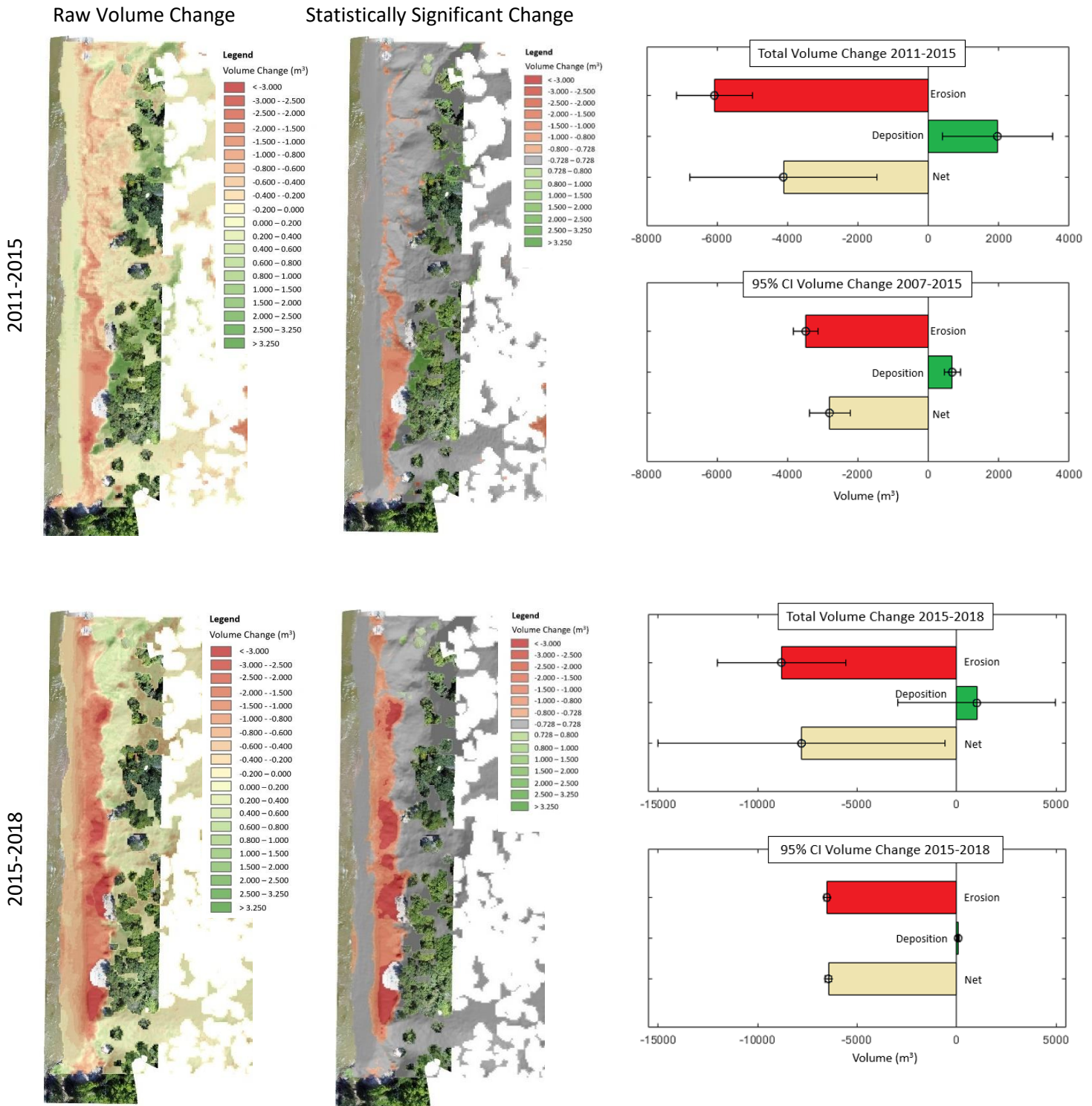


Figure 27. Zone 1 South 2011-2015 and 2015-2018 DoDs with volumetric change calculations. Volumetric change within the LOD_{min} is shaded grey and is not statistically significant. Histograms show the volume of change measured and the associated error.

7.3.3 *Zone 2.* Zone 2 is located at the narrowest and lowest relief part of the barrier most susceptible to overwash (Fig. 11). This region experienced significant changes after the high-water summer of 2019 and the November 2019 storm that struck the barrier. This zone recorded the lowest significant net deposition ($635.8 \pm 250.2 \text{ m}^3$) during the pre-high water summer interval from 2007-2015 (Table 12). Deposition was isolated to the primary dune (Fig. 28). Net significant volume change from 2015-2018 was $1,207.2 \pm 383.8 \text{ m}^3$ (Table 12). Erosion was located on the beach berm in the central part of the zone, which was low in elevation to begin with (Fig 28). Narrow channels formed in at least two locations at points of weaknesses between 2018 and 2020. Subaerial washover fans formed extending from two excavated channels and was still subaerial through the summer of 2021 (Fig 21).

7.3.4 *Zone 3.* The channel inlet, characterizing Zone 3, experiences some of the most rapid and predictable changes throughout the study period (Fig. 11). As discussed in the DSAS shoreline analysis (section 7.1), the inlet is migrating north, resulting in net deposition on the southern spit and net deposition on the northern spit (Fig. 19 and 20).

The cross-section profiles at this location vary greatly from year to year. East (landward) of the primary dune, the topography is more stable. The changes in shape to the cross-shore profile from 2007-2015 demonstrate the variable nature of the topography as a result of the close proximity to the channel in which sand bars suture to the barrier forming the recurved spits described by Mattheus et al. (2016) (Fig 23d). Prior to the high water summer of 2017 a series of small dunes formed and accreted . From 2015- May

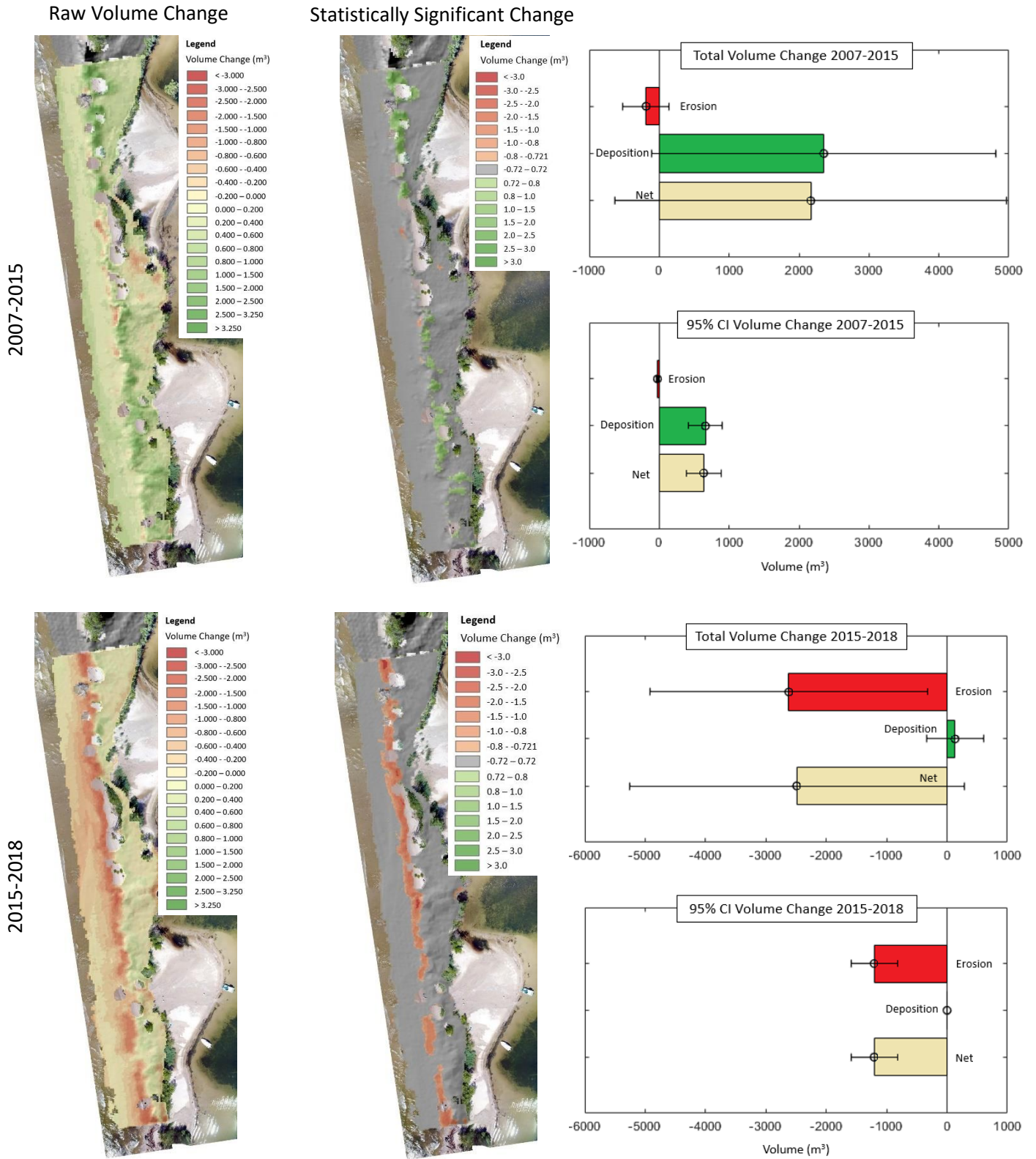


Figure 28. Zone 2 2007-2015 and 2015-2018 DoDs with volumetric change calculations. Volumetric change within the LOD_{min} is shaded grey and is not statistically significant. Histograms show the volume of change measured and the associated error.

2018 the two dunes morphed into the primary dune system; by September 2018 the two-dune system emerged again with the formation of a small lakeward foredune in front of the prior single large dune. From September 2018-2020 the foredune was reshaped and moved lakeward (Fig 23d).

This zone had the highest magnitude fluctuations in volumetric changes. From 2007-2015, the net significant volumetric change was $14,457.2 \pm 5,094.6 \text{ m}^3$ of deposition, however from 2015-2018 the same region measured $4,322.9 \pm 3,467.7 \text{ m}^3$ of erosion (Table 12; Fig. 29). Volumetric changes are for the most part, isolated to the regions closest to the lake shoreline. South of the inlet, deposition is concentrated lakeward and along the primary dune system (Fig 29). North of the channel, deposition is concentrated along the lakeward shoreline as the channel migrates north. The area of erosion increases during the 2015-2018 interval (Fig. 29). It is worth noting that this region is most susceptible to human intervention as sand is dredged from the channel semi-annually to allow boats to pass through, supporting recreation and the local economy (Table 2). During many of these projects, the dredged material was placed back onto the barrier beach and dunes.

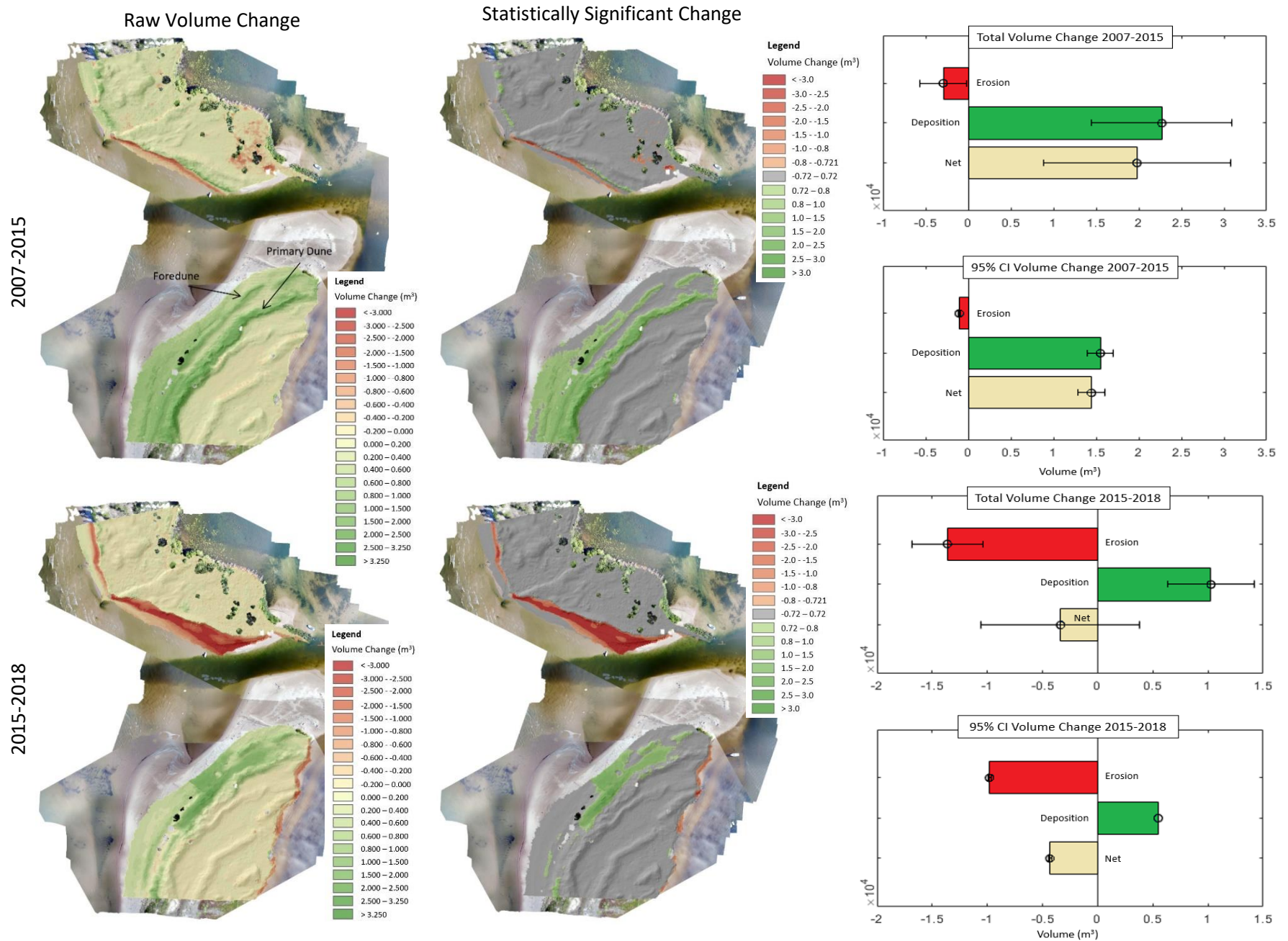


Figure 29. Zone 3 2007-2015 and 2015-2018 DoDs with volumetric change calculations. Volumetric change within the LOD_{min} is shaded grey and is not statistically significant. Histograms show the volume of change measured and the associated error.

7.3.5 Zone 4. Zone 4 is a thinner part of the spit with high enough dunes to prevent overwash. Most of the changes to the profile are on the beach, lakeward of the foredune crest (Fig. 23e). As beach aggrades, the slope of the foredune steepens. Both 2018 profiles demonstrate this steepening while maintaining the same relative position and elevation of the 2015 foredune crest. By August 2020, the foredune moved landward (east) and decreased in height.

The 2007-2015 interval measured a net change of $3,808.6 \pm 1,617.0 \text{ m}^3$ of deposition, mostly located along the foredune region (Table 12; Fig. 30). During the 2015-2018 interval a net change of $336.2 \pm 137.6 \text{ m}^3$ of erosion occurred (Table 12). The region of deposition at the foredune face during the previous interval became erosional or statistically insignificant. Again, the only major area of statistically significant change is the erosion in the northeast corner of the zone (Fig. 30).

7.3.6 Zone 5. Zone 5 is located just south of Zone 4 and is where the previous channel inlet existed, active from 1943-1960 (Mattheus et al., 2016). This part of the barrier is very similar to that at Zone 4 and has a similar cross-shore pattern of erosion and deposition (Fig. 23f). From 2007-2015, the primary dune experienced aggradation. Just to the east of the primary dune is a densely vegetated freshwater marsh, remnant from the old channel. Accretion on the beach in the northern part of the region was significant resulting in a net volumetric change of $3,694.0 \pm 1,339.5 \text{ m}^3$. From 2015-2018 the areas previously experiencing accretion, measured insignificant volume change. The region became erosive with a net change of $105.8 \pm 52.6 \text{ m}^3$ distributed in the beach face region (Fig. 31). This region experienced the least amount of volumetric change during this period.

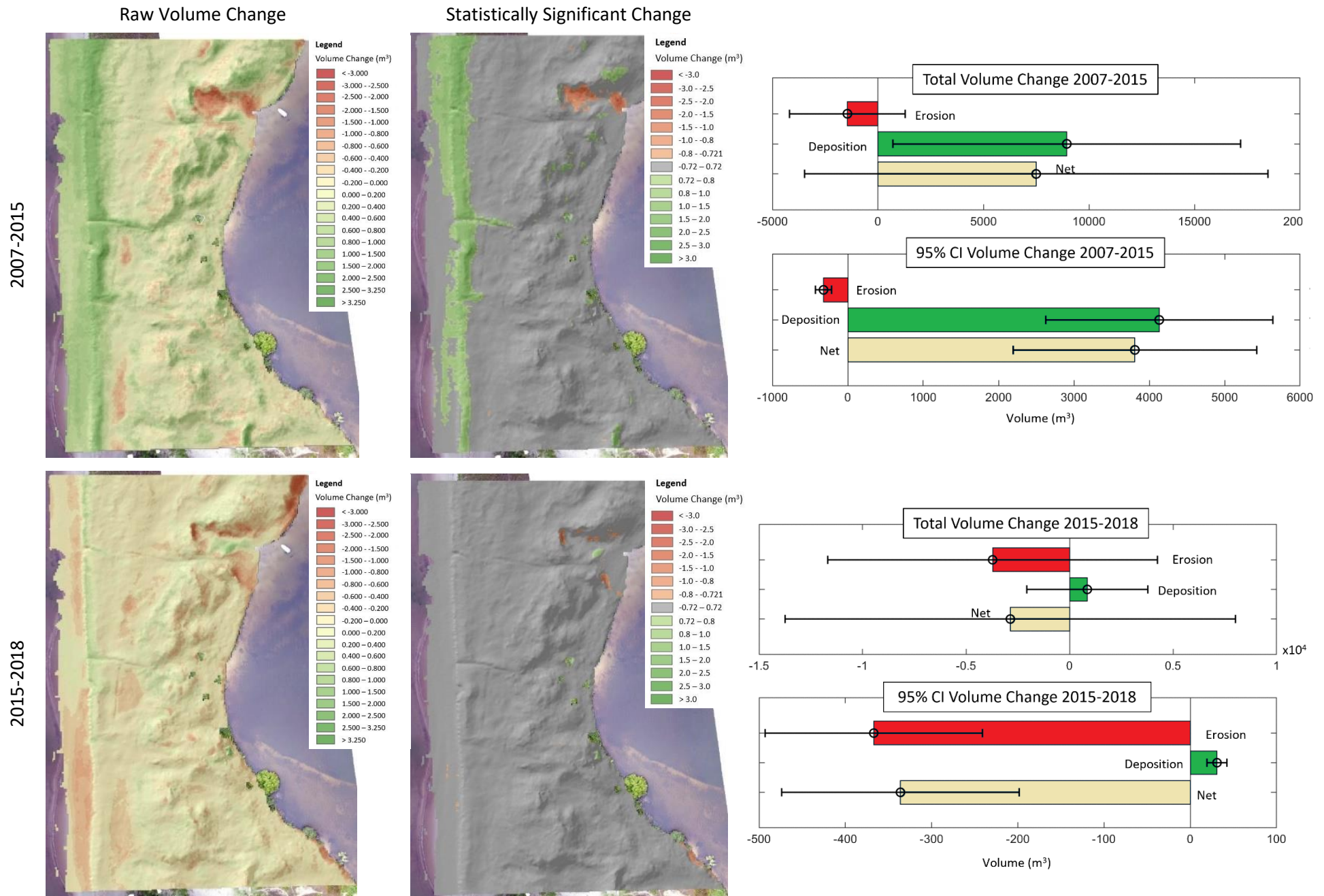


Figure 30. Zone 4 2007-2015 and 2015-2018 DoDs with volumetric change calculations. Volumetric change within the LOD_{min} is shaded grey and is not statistically significant. Histograms show the volume of change measured and the associated error.

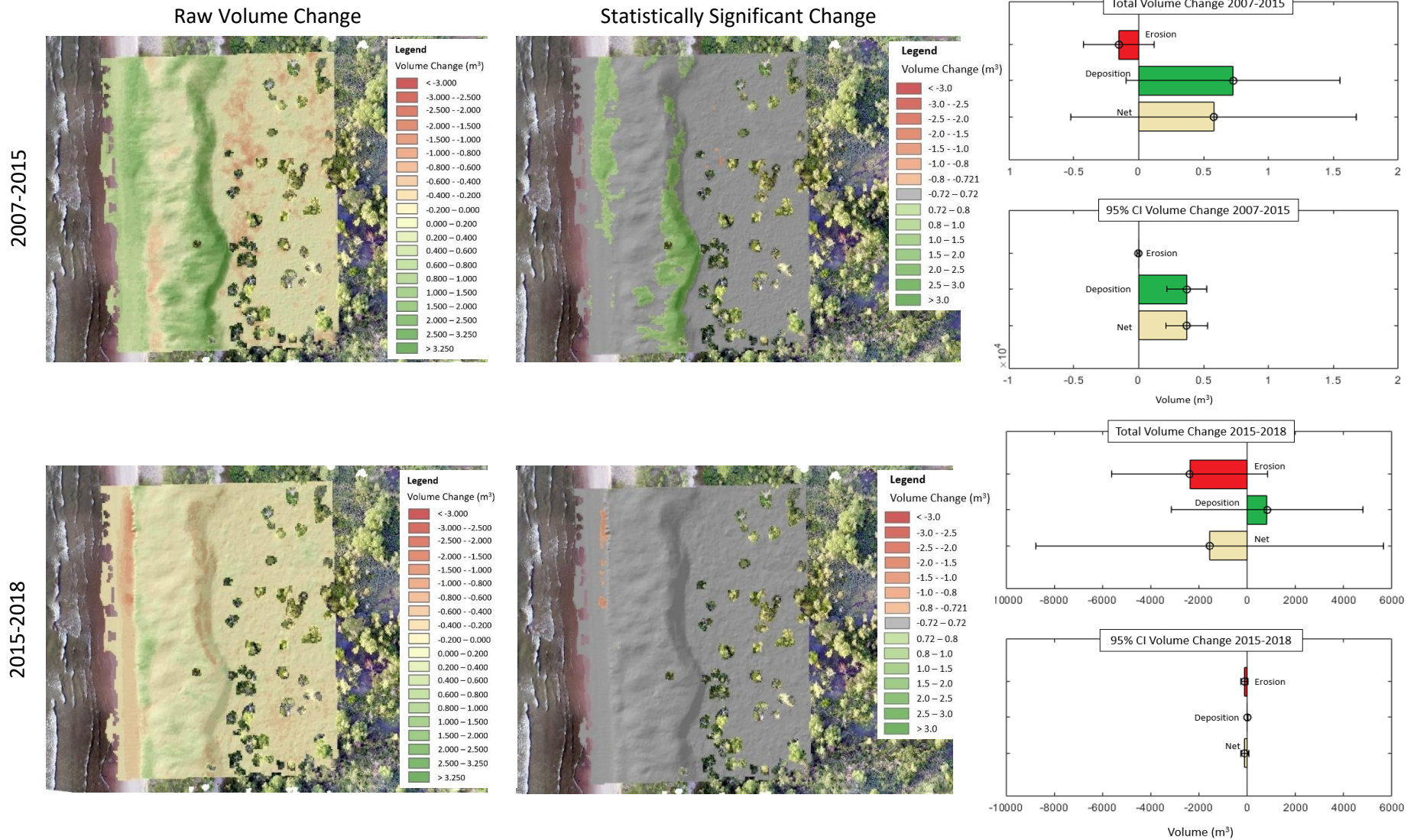
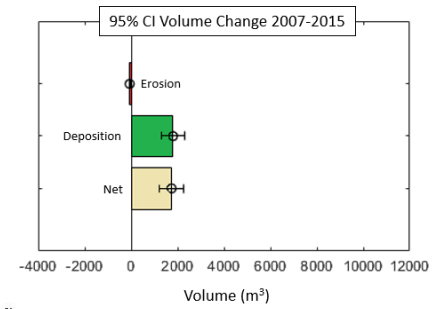
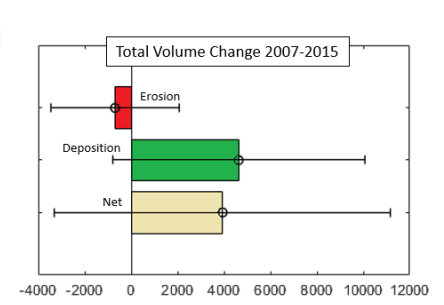
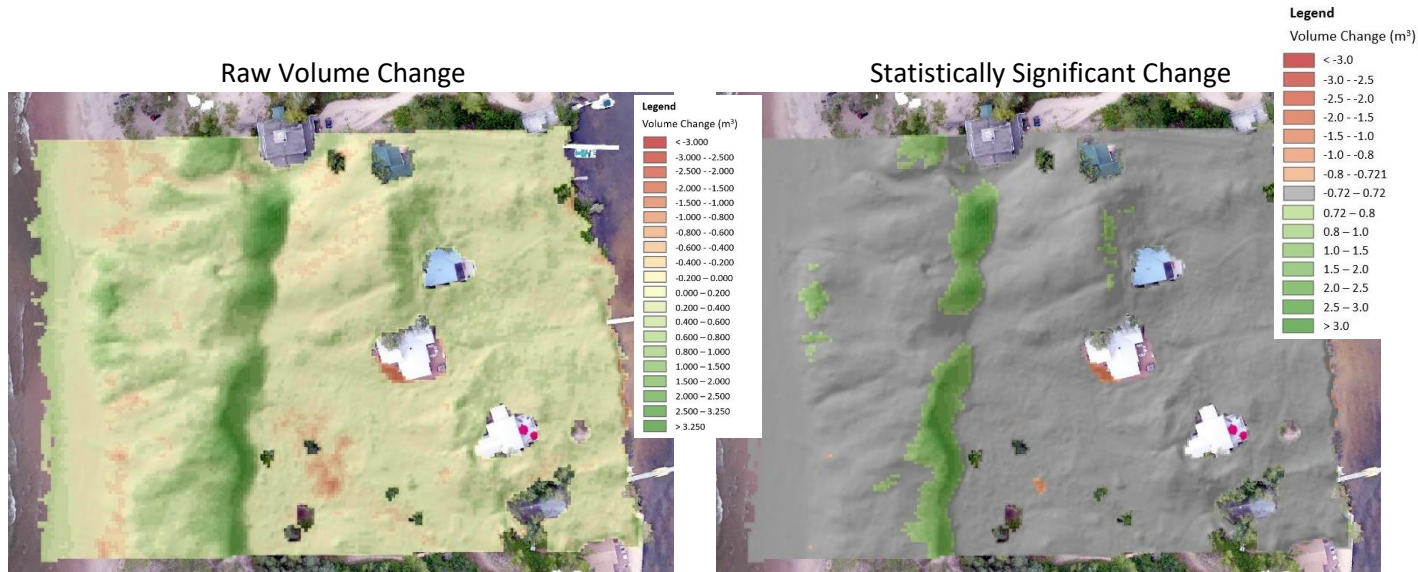


Figure 31. Zone 5 2007-2015 and 2015-2018 DoDs with volumetric change calculations. Volumetric change within the LOD_{min} is shaded grey and is not statistically significant. Histograms show the volume of change measured and the associated error.

7.3.7 Zone 6. Zone 6 is located on private beach property and is trafficked exclusively by landowners. Unlike Zone 4 and 5, this part of the barrier has two back-barrier dunes (Fig. 23g). Most of the topographic change is located on the two dunes closest to the lake (Fig. 32). The primary dune, situated just east of the foredune increased in elevation from 2007-2020, and is migrating east slightly with aggradation on the back-barrier side, and erosion on the lakeward facing side. The foredune experienced the most dramatic volumetric change (Fig 23g and 32). From 2007-2015 the region experienced widespread net deposition of $1,746.1 \pm 515.9 \text{ m}^3$ of the eastern side of the primary dune (Table 12; Fig. 32). From 2015-2018, the net volumetric change was negative equal to $-375.6 \pm 159.9 \text{ m}^3$ (Table 12). Most erosion was concentrated on the slope of the foredune and on the beach. The beach of the eastern side of the spit was additionally eroded (Fig 32).

7.3.8. Zone 7. Zone 7 has experienced little significant change from 2007-2020 (Fig. 33). This is a sparsely vegetated dune, directly adjacent to a Sandy Island State Park public beach. The cross-shore profile indicates this area has experienced little vertical and horizontal change (Fig. 23). It has had a relatively stable shape and profile. The western most dune, closest to LO progressively increased in elevation from 2007-2018 in height and width. By August 2020, it was no longer a distinct feature (Fig. 23h). From 2011-2015, $160.8 \pm 107.2 \text{ m}^3$ of statistically significant deposition was measured at the foredune and the back of the primary dune at the western side of the high elevation platform (Table 12; Fig 33). From 2015-2018, the net significant change was $5.8 \pm 21.7 \text{ m}^3$, indicating no consistent pattern of erosion or deposition (Table 12; Fig 33). Overall, this zone did not experience high fluctuations in erosion and deposition.

2007-2015



2015-2018

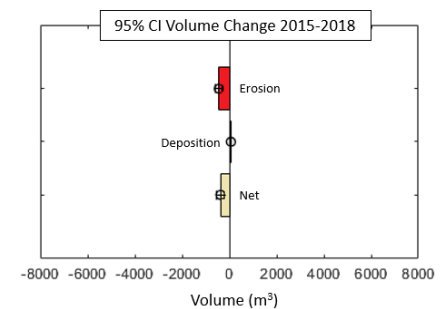
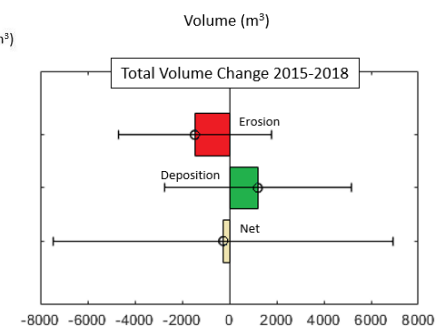
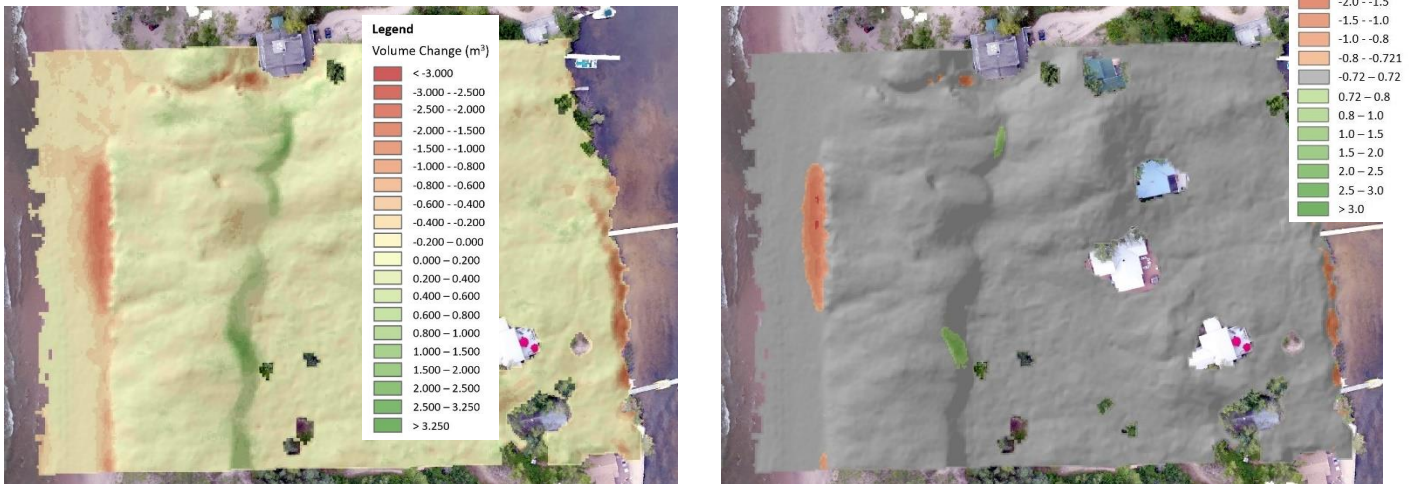
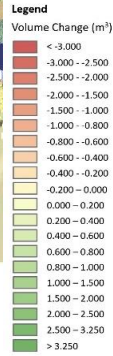


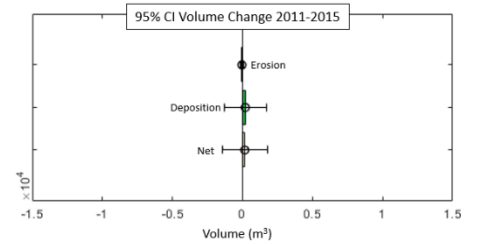
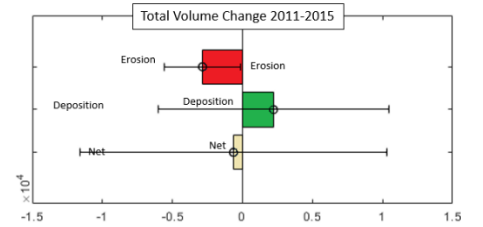
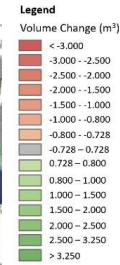
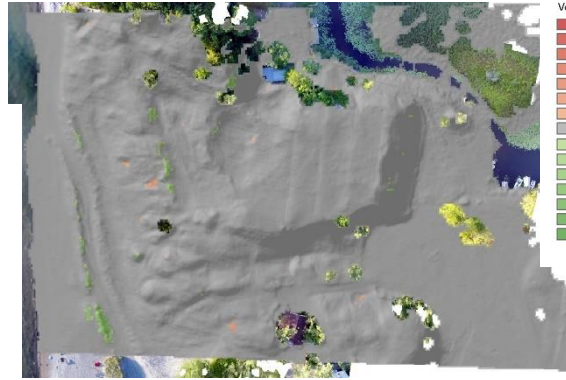
Figure 32. Zone 6 2007-2015 and 2015-2018 DoDs with volumetric change calculations. Volumetric change with in the LOD_{min} is shaded grey and is not statistically significant. Histograms show the volume of change measured and the associated error.

2011-2015

Raw Volume Change



Statistically Significant Change



2015-2018

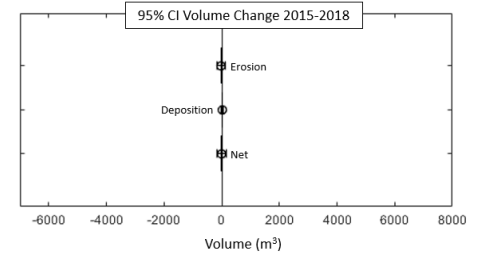
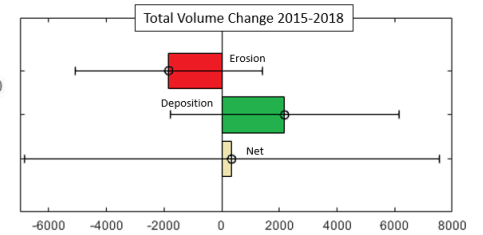
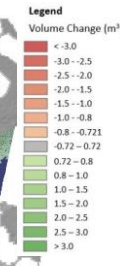
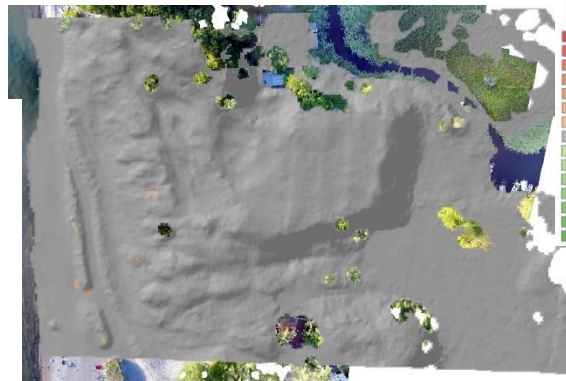
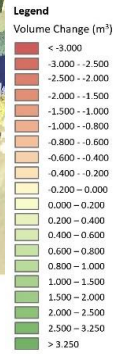
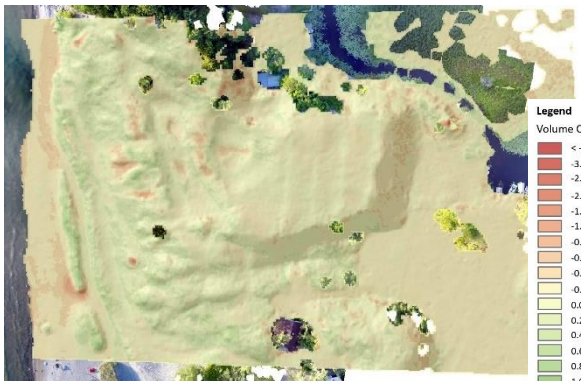


Figure 33. Zone 7 2011-2015 and 2015-2018 DoDs with volumetric change calculations. Volumetric change within the LOD_{min} is shaded grey and is not statistically significant. Histograms show the volume of change measured and the associated error.

8. Discussion

The results of this study indicate measurable geomorphic change occurred on the SPS during the three intervals studied: 2001-2015, 2015-2018, and 2018-2020. These three intervals provide useful information for describing the impact of the summers with anomalously high-water levels in 2017 and 2019. Such changes occur over sub-decadal periods indicating the SPS is sensitive to the previously described forcings of lake level, storm surges, and ice cover at shorter intervals. The following summarizes each study interval before discussing the hypothesis testing, limitations, and implications for the future of the SPS. Hypotheses explored in this study include (Table 4):

- H1.** The SPS system is transgressive.
- H2.** The rate of eastward shoreline migration increased from 2015-2020 compared to 2001-2015.
- H3.** The net change in volume of sediment of the subaerial SPS system was negative during the high-water summers; the SPS system lost a significant amount of subaerial sediment from 2015-2020.
- H4.** The volume of erosion is concentrated on the beach during high lake level summers.
- H5.** The alongshore average change in dune crest position and elevation is eastward and negative, respectively from 2007-2020.
- H6.** Lake level is the most important erosional factor impacting the SPS.

8.1 2001-2015: pre-high-water event. The earliest interval, from 2001-2015, is the longest and records the stability of the barrier-spit prior to the high-water events. During the pre-high-water intervals, the volumetric change was net depositional at all locations except at Zone 1 (Table 12; Figs. 26 and 27). At the two parts of Zone 1 the primary dune is adjacent to the shoreline. Exposed sand is sparsely vegetated and easily undercut by wave action. Thus, oversteepening and subsequent failure are likely to occur regardless of the water level conditions.

Statistically significant deposition during this interval was concentrated on the beach part of the spit, lakeward of the foredune crest (Fig. 34). This is consistent with beach build-up during swell conditions in ocean-barrier wave dominated beaches as offshore bars migrate shoreward and suture to the beach (Komar, 1998). The swell beach profile has a foredune which gently slopes into a broad berm created from the build-up and accumulation of bars migrating onto the beach gradient (Fig. 35). This profile is demonstrated at the cross-shore profiles of Zones 1-7 for the years 2007-2015 (see section 7.3). Accretion of sand on the beach additionally contributed to the net advance of the shoreline during this interval. The adjusted mean RSC is closest to zero indicating the shoreline remained stable and thus the barrier remained stable, despite experiencing eight of the top ten wave height-producing storms (Table 9; Fig. 20; Table 1).

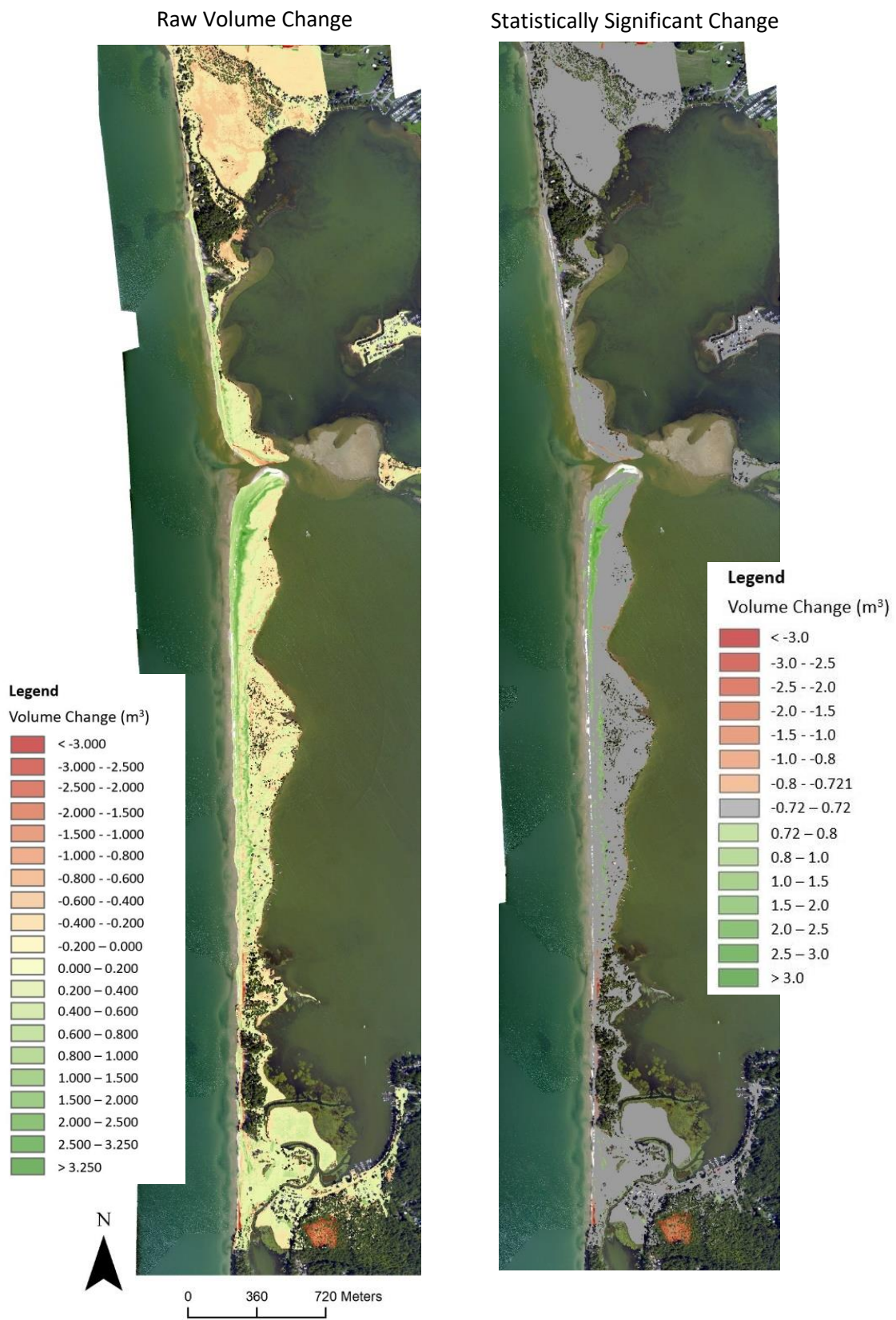


Figure 34. 2007-2015 raw and thresholded DoD across the whole study area.

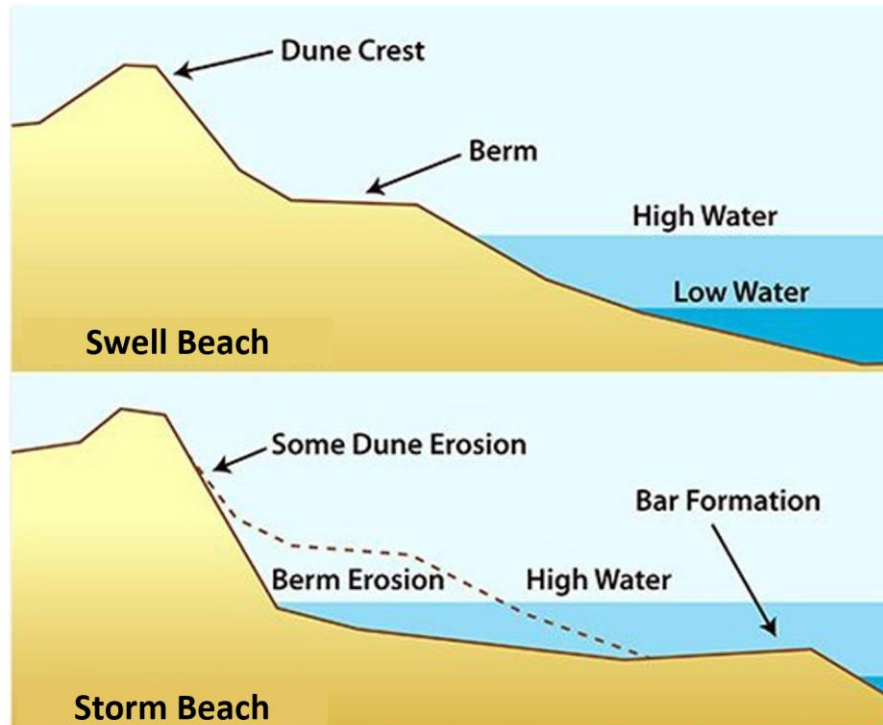


Figure 35. Schematic of typical swell and storm beach profiles (modified from Friends of IBSP, 2022).

8.2 2015-2018: Including summer 2017. The 2015-2018 interval included the high-water summer of 2017 when the water was roughly 0.5 m above the OMHW level from May to June (Fig. 5). There were no notable storm events with wave heights greater than 4.5 m (Table 1). The volumetric change at all zones studied was net erosional, with over three times more erosion in Zone 1 than measured during the previous interval (Table 12; Fig. 36). The high magnitude fluctuations in net volumetric change from the previous interval to this support water level was the major forcing that drove geomorphic change (H6; Table 12).

Cross-shore profiles and DoD analysis indicates the majority of the erosion occurred between the foredune and the shoreline (section 7.3; Fig 23; Fig. 36). Erosion on the beach was dominated by erosion of the dune toe by wave action which altered the

slope of the foredune extending to the beach. Lateral erosion of the beach was not limited to high relief dunes adjacent to the shoreline and extended across the entire barrier-spit in low relief areas like Zones 4-6 (Fig 23, 30-32). The resulting beach profile resembled the storm profile typically developed during stronger weather events (Komar, 1998; Fig. 35). Erosion at the base of the foredune caused in the greatest amount of eastward horizontal foredune migration (2.33 m) for any interval (Table 11). Increased movement of the foredune crest resulted in higher magnitude fluctuations in the elevation of the foredune as described by S1 and S2 (see section 7.2) (Fig. 21 and 22).

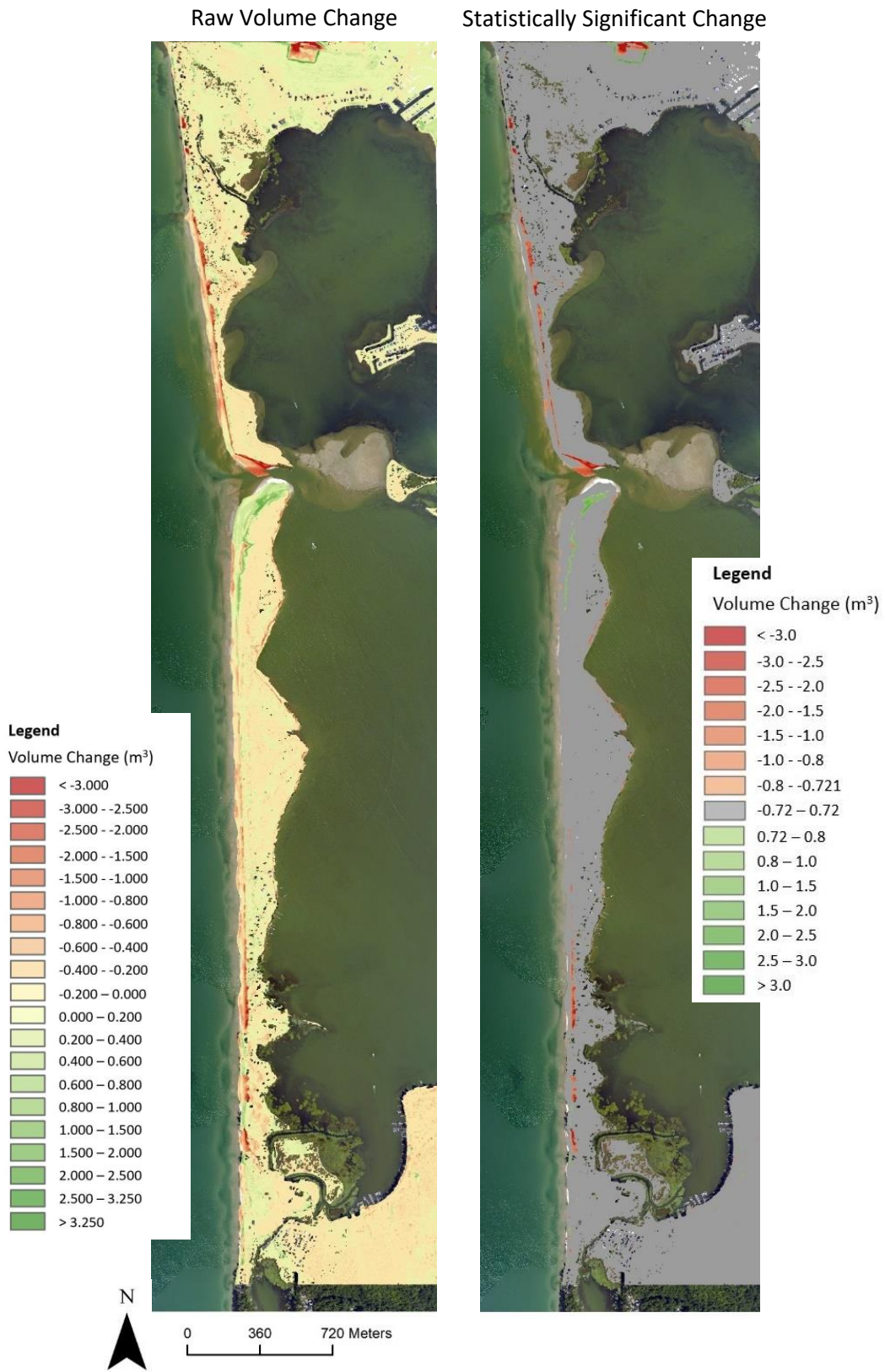


Figure 36. 2015-2018 raw and thresholded volumetric change across the whole study area.

8.3 2018-2020: Including summer 2019 and November 2019 storm. During the most recent interval from 2018-2020 the SPS again included a high-water event during the summer of 2019 (Table 1; Fig. 5). Two of the top ten wave heights in the eastern basin caused by storms were recorded during this time, the first on November 10, 2018, and the second and larger event on November 1, 2019 (Table 1). During this time, the SPS was net erosional. Although DoDs were not used to analyze this interval, erosion clearly occurred, based on the cross-shore profiles (see section 7.3; Fig 23). In some cases, there was more erosion during this interval than during the previous one (Fig. 23). Additionally, this interval recorded the highest rate of shoreline retreat at -3.27 ± 0.12 m (adjusted RSC -3.79 ± 0.12 m) (Fig.19). This value is 5.27 times greater than the rate of shoreline retreat during the 2015-2018 interval (Table 9). Although measurements during this most recent period have biases due to limited sampling size, it is clear erosion is occurring as a result of the high water summer of 2019.

The foredune crest during this period did not move laterally despite increased shoreline retreat (Table 10). It is possible the foredune crest movement that occurred from 2015-2018 resulted in a foredune position and elevation able to withstand additional wave action and stabilized after the high-water summer of 2017. The difference in maximum mean monthly lake level for 2017 and 2019 was only 0.04 m (Fig. 5).

On November 1, 2019, the eastern shore of LO was struck by a storm measuring the second highest offshore significant wave height (Table 1). The offshore eastern basin buoy measured a significant wave height of 6.17 m, and local news reports estimate waves were in excess of 5.2 m high by the time they crashed on shore (Muir, 2019). The storm was coined “The Halloween Storm” and affected much of the eastern shore of LO

(Muir, 2019). The monthly mean lake level during November 2019 was 0.17 m higher than the lake level was in the same month in 2017 and above the long-term average, likely increasing the storm's erosive power on the beach (Fig. 5). The impact of this storm cannot be uncoupled from the impact of the high lake levels of 2019. This interval thus represents the impact of strong storm events and high lake levels. It is not clear if the storm caused the higher magnitudes of erosion measured during this interval, but it is clear the water level is an important erosive force to the spit (H6).

The smaller storm event, measuring an offshore wave height of 4.59 m occurred on November 10, 2018, almost a year before “The Halloween Storm” (Muir, 2019). This storm did not generate the same attention, nor were there numerous reports of the destruction caused to the eastern LO shoreline. This storm, while smaller in wave height, did not occur under anomalously high-water conditions suggesting again, water-level is the most important forcing driving geomorphic change to the region (H6) (Table 1; Fig. 6).

8.4 Hypothesis testing. The six hypotheses motivating this study sought to answer questions, quantify, and interpret the geomorphic change during the studied intervals using the three metrics studied (Table 3). A transgressive barrier records landward movement of the barrier over time. Barriers typically transgress during sea level rise. To determine if a barrier is transgressive, shoreline position and foredune must be considered. The SPS was not transgressing from 2001-2015. During this interval, the shoreline advanced and the foredune migrated towards the lake. From 2015-2018 both shoreline retreat and foredune migration landward occurred (Table 9). During this period, the SPS was transgressive. From 2018-2020, the foredune crest did not move

significantly laterally despite increased shoreline retreat (Fig. 12). Because of the short-term fluctuations in the behavior of the shoreline and the foredune crest from 2015-2020 there is not enough conclusive information to support that the SPS is transgressive (H1). Instead, there are periods of both barrier transgression and regression.

Shoreline analysis recorded increased rate of retreat during the high-water intervals from 2015-2020 compared to prior from 2001-2015 (H2) (Fig. 19). The highest rate of shoreline retreat during the 2018-2020 interval was 13 times greater than the rate of shoreline advance measured 2001-2015. Although there are less data for the 2018-2020 interval, the rate of shoreline retreat from Zones 1-7 is used to represent the changes to the barrier at large. This supports that the shoreline retreated eastward and the rate increased during the high water summers (H2).

The calculated volume change on the SPS at the studied sites was positive from 2007-2015 and negative and increased in magnitude from 2015-2018 (H3). This supports that the SPS is losing subaerial sediment. Where this sediment is redistributed is not known. It is possible the eroded sediment is carried offshore and forms bars which may be redistributed on the subaerial barrier in the future. One location of deposition is on the western side of Carl Island, where a subaqueous shoal is forming as the pond fills with sediment carried by the LO longshore transport (Fig. 7). Deposition in the inlet region of the pond is well recorded from the dredging projects which semi-annually remove material from the channel (Table 2). For these reasons, this hypothesis is supported.

DoDs of individual zones and cross-shore profiles indicate the changes in elevation and thus changes in volume were concentrated in the region between the foredune crest and the shoreline (Figs. 23, 34 and 36). Therefore, the majority of the

volumetric change occurred on the shoreface or beach (H4). As previously mentioned, the persistent wave action on the beach due to higher water levels led to increased wave undercutting resulting in concentrated erosion in this region. Because of the pattern of erosion and the varying topography along the SPS, while the foredune crest moved eastward during the period of high-water events from 2015-2020, the elevation of the foredune crest did not necessarily decrease as well (H5) (Table 11). This partially supports H5 describing the net eastward migration of the foredune.

It is clear from the data presented from all three metrics that the lake level is one of the most important factors influencing geomorphic change on the SPS (H6). The 2015-2020 interval measured significant changes in volumetric change from the longer period of stability from 2007-2015 (Table 12). The majority of the storm events that occurred in the study period were during the 2007-2015 interval when the water level was not above average. The remaining two storms occurred during the 2018-2020 interval when increased rates of shoreline retreat and erosion on the cross-shore profiles occurred. This was likely more due to the high water than the storms. As stated earlier, the impact of the high water events and the storms could not be decoupled. Thus, it is reasonable to state based on the results of this study, that the water level had more of an impact on geomorphic change than storm waves (H6). The impact of ice cover was not assessed in this study.

8.5 Limitations. Although this study involved a thorough analysis of sub-decadal changes to the SPS over a shorter study period and at a higher resolution compared to Mattheus et al. (2016) and Hart and Steadman (2017), most of the surveys used were from the summer and fall months. This results in a biased interpretation of the

topography and does not capture the winter and spring beach profiles when strong storm events excavate sand away from the beach and ice cover protects the shore from waves. Continued analysis during all four seasons, would provide critical information to better understand geomorphic change to the SPS. Storms are most frequent in the spring and fall, and ice cover develops during the winter. The exact role of ice-cover in this region as well as storms has not yet been quantified at sub decadal intervals. However, it is clear that water level causes significant change over sub-decadal periods. Further study of ice cover and the pre- and post-winter topography would be useful for constraining the impact of ice cover on the beach.

The SfM derived DEMs were unable to filter out vegetation to produce bare earth DEMs. For this reason, visualizations of the 2018-2020 volumetric change are limited to the cross-shore profiles. To better quantify the difference between the two intervals with high-water events, it would be useful to have lidar data for 2020 or 2021.

8.6 Implications for management of the SPS. Anthropogenic impacts to the barrier cannot be ignored. Channel dredging during the study period and ongoing restoration efforts alter the topography that was measured in the DoD analysis. Historical records of the time, location, and amount of dredging indicate Zones 2 and 3 are most directly affected by dredging (Table 2; Fig 11). Dredged material in all cases was returned to the spit to fortify the eroding foredune and primary dune systems (Table 2).

A first order comparison of the net significant volumetric change during the first two intervals to the estimated volume of dredged material suggests the erosion that occurred from 2015-2018 is roughly the same as the material dredged from 2001-2021. From 2007-2015 the net significant change in all seven zones was $21,035 \pm 10,711 \text{ m}^3$ of

deposition. The estimated volume of dredged material was 31,558 m³ (Table 2). From 2015-2018 a total of 14,771 ±6,370 m³ of erosion occurred and roughly 14,480 m³ of material was dredged. It is noteworthy that the net volume change values presented here do not encompass the entire subaerial region of the SPS, just the zones studied, and should be evaluated with caution.

Dune grass plantings occurred in response to the high-water summers to anchor sand in place with the hope it would stabilize the dune and prevent future washover and blow outs. It is not clear yet if this was an effective solution to increasing the barrier's resiliency and stability, however it seems promising that fortifying this region will prevent any additional breaches. Even though the inlet region is appreciably impacted by humans and sand is redistributed semi-annually, it is clear this region was significantly impacted by the high-water events.

9. Conclusion

The work presented here provides compelling evidence lake level is a dominant forcing on the geomorphic processes shaping the SPS. The question becomes, when is the water level impacting the geomorphic structure of the SPS the most? From May to September or October to April? And how much do storms and ice cover impact the pattern and magnitude of change? How much of the water level fluctuations are controlled by human management? Storms are most frequent in the spring and fall, and ice cover develops during the winter depending on the weather conditions. The exact role of ice cover in this region as well as storms has not yet been quantified however if there

were little ice cover (conditions for the most erosion) it is likely the water level would still be driving the geomorphic change.

Still, it is clear the lake level and storm surge strength and frequency drive measurable geomorphic changes to the SPS over sub-decadal periods. The SPS endured significant erosion due to the high-water levels as a result of especially wet springs and the management of the lake level. If the SPS is subjected to more high-water events without the opportunity to recover during average or low lake level summers, the stability and resilience of the barrier will be jeopardized. Should Plan 2014 manage the lake levels to restore critical wetland and marsh habitats as it intends, it should be sure to accommodate the flux of water entering the lake to stay within the range of anticipated water levels (Table 2).

Overall, the barrier remains stable when given the necessary time to recover, as indicated by the primary dune which remains stable despite fluctuations in the height and position of the foredune, altered most by wave conditions. Locally, there is great interest in ensuring the barrier remains stable, and that the channel inlet open in its present location. Although not natural, the reestablishment of the primary dune using dredged material and dune grass plantings may prevent further overwash and increase the resilience and stability of the barrier at large. Dredging will likely continue to keep the channel open and support recreation and the economy, but the placement of the materials may change.

At the time of writing in the fall of 2022, the lake levels have remained within average and the SPS has not experience another high water summer event. This has provided the opportunity for the beach to replenish itself with sand along the beach and

smooth the gradient of the beach profile. The large extent of the beach provides more area for the beach to rebuild as winds collect sand at the beach. It would be interesting to quantify the speed and magnitude of recovery of the beach since the summer of 2019.

References

- Balaguer-Puig, M., Marques-Mateu, A., Lerma, J. L., & Ibanez-Asensio, S. (2017). Estimation of small-scale soil erosion in laboratory experiments with Structure from Motion photogrammetry. *Geomorphology*, 295, 285–296. <http://dx.doi.org/10.1016/j.geomorph.2017.04.035>
- Barrineau, P., Wernette, P., Weymer, B., Trimble, S., Hammond, B., & Houser, C. (2015). The Critical Zone of Coastal Barrier Systems. In *Principles and dynamics of the critical zone* (Vol. 19, pp. 497–522). Elsevier.
- Brantley, S. T., Bissett, S. N., Young, D. R., Wolner, C. W. V., & Moore, L., J. (2014). Barrier island morphology and sediment characteristics affect the recovery of dune building grasses following storm-induced overwash. *PLOS ONE*, 9(8). <https://doi.org/10.1371/journal.pone.0104747>
- Breederland, M. (2017, July 5). May, June storms bring higher Great Lake water levels for summer 2017. Retrieved August 9, 2022, from https://www.canr.msu.edu/news/great_lakes_levels_summer_2017_outlook_msg17_breederland17
- Brock, J., & Purkis, S. (2009). The emerging role of lidar remote sensing in coastal research and resource management. *Journal of Coastal Research*, 25(53), 1–5.
- Carter, E., & Steinschneider, S. (2018). Hydroclimatological drivers of extreme floods in Lake Ontario. *Water Resources Research*, 54, 4461–4478. <https://doi.org/10.1029/2018WR022908>
- Davis, Jr., R. A. (1983). *Depositional Systems: A genetic approach to sedimentary geology*. New Jersey: Prentice Hall.
- Democrat and Chronicle, S. (2019, June 14). Strong winds, waves prompt new flood warning for Lake Ontario shoreline Friday. Retrieved August 9, 2022, from <https://www.democratandchronicle.com/story/news/2019/05/28/lake-ontario-flooding-2019-rochester-ny/1260404001/>
- Eisemann, E. R., Wallace, D. J., Buijsman, M. C., & Pierce, T. (2018). Response of a vulnerable barrier island to multi-year storm impacts: LiDAR-data-inferred morphodynamic changes on Ship Island, Mississippi, USA. *Geomorphology*, 313, 58–71. <https://doi.org/10.1016/j.geomorph.2018.04.001>
- Friends of IBSP. (2022). Science of the Shore – A Tale of Two Beaches: Winter & Summer Beach Profiles – Friends of Island Beach State Park. Retrieved August 9, 2022, from <https://www.friendsofibsp.org/breaking-news/science-of-the-shore-a-tale-of-two-beaches-winter-summer-beach-profiles/>
- GLISA. (2017). *2017 Annual Climate Trends and Impacts Summary for the Great Lakes Basin*. Retrieved from <https://glisa.umich.edu/wp-content/uploads/2021/02/2018-Climate-Trends-and-Impacts-Summary.pdf>
- GLISA. (2019). *2019 Annual Climate Trends and Impacts Summary for the Great Lakes Basin*. Retrieved from <https://glisa.umich.edu/wp-content/uploads/2021/02/2019-Climate-Trends-and-Impacts-Summary.pdf>
- Google Earth Pro. (2022). (Version 7.3.4.8642). Google. Retrieved from <https://www.google.com/earth/versions/>

- Grieco, M. B., & DeGaetano, A. T. (2019). A climatology of extreme wave height events impacting eastern Lake Ontario shorelines. *Theoretical and Applied Climatology*, 136(1–2), 543–552. <https://doi.org/10.1007/s00704-018-2502-9>
- Great Lakes - St. Lawrence River. (2022). Retrieved August 27, 2022, from <https://www.ijc.org/en/watersheds/great-lakes>
- Hart, T., & Steadman, G. (2017). *North Pond Resiliency Project: A comprehensive analysis of shoreline change and inlet dynamics on the eastern shore of Lake Ontario*. Oswego County Soil and Water Conservation District.
- Himmelstoss, E.A., Henderson, R.E., Kratzmann, M.G., & Farris, A.S. (2018). Digital Shoreline Analysis System (DSAS) version 5.0 user guide: U.S. Geological Survey Open-File Report 2018-1179, 110 p., <https://doi.org/10.3133/ofr2018179>.
- Houser, C., Hapke, C., & Hamilton, S. (2008). Controls on coastal dune morphology, shoreline erosion and barrier island response to extreme storms. *Geomorphology*, 100, 223–240.
- Houser, C., Wernette, P., & Weymer, B. (2018). Scale-dependent behavior of the foredune: Implications for barrier island response to storms and sea-level rise. *Geomorphology*, 303, 362–374.
- IGLD 1985 (1992). *BrochureOnTheInternationalGreatLakesDatum1985.pdf*, <https://www.lre.usace.army.mil/Portals/69/docs/GreatLakesInfo/docs/IGLD/BrochureOnTheInternationalGreatLakesDatum1985.pdf> (accessed April 2020).
- International Joint Commission (IJC) (2014). Lake Ontario St. Lawrence River Plan 2014: Protecting against extreme water levels, restoring wetlands and preparing for climate change: International Joint Commission, https://legacyfiles.ijc.org/tiny_mce/uploaded/LOSLR/IJC_LOSR_EN_Web.pdf (accessed October 2019).
- Johnson, C. L., Chen, Q., & Ozdemir, C. E. (2019). Lidar time-series analysis of a rapidly transgressing low-lying mainland barrier (Caminada Headlands, Louisiana, USA). *Geomorphology*, 352. <https://doi.org/10.1016/j.geomorph.2019.106979>
- Kim, R. (2018). *Using aerial photographs to quantify the progradation rates of inlet deltas of Ossipee Lake, New Hampshire* (Geological Sciences Independent Study). Boston College, Boston.
- Komar, P. D. (1998). *Beach processes and sedimentation* (2nd ed). Upper Saddle River, N.J: Prentice Hall.
- Lake Ontario Flooding. (2019, May 23). Retrieved October 6, 2020, from <https://www.ny.gov/programs/lake-ontario-flooding>
- Lallias-Tacon, S., Liebault, F., & Piegay, H. (2014). Step by step error assessment in braided river sediment budget using airborne LiDAR data. *Geomorphology*, 214, 307–323. <http://dx.doi.org/10.1016/j.geomorph.2014.02.014>
- Le Mauff, B., Juigner, martin, Ba, A., Robin, M., Launeau, P., & Fattal, P. (2018). Coastal monitoring solutions of the geomorphological response of beach-dune systems using multi-temporal LiDAR datasets (Vendee coast, France). *Geomorphology*, 304, 121–140.
- Lentz, E. E., & Hapke, C. (2011). Geologic framework influences on the geomorphology of an anthropogenically modified barrier island: Assessment of dune/beach

- changes at Fire Island, New York. *Geomorphology*, 126, 82–96.
<https://doi.org/10.1016/j.geomorph.2010.20.032>
- Mattheus, C. R., Fowler, J. K., Diggins, T. P., & Allen, D. F. (2016). Barrier-spit geomorphology and inlet dynamics in absence of tides: evolution of the North Pond system, eastern Lake Ontario, New York State. *Earth Surface Processes and Landforms*, 41, 1386–1398. <https://doi.org/10.1002/esp.3915>
- Mitasova, H., Overton, M. F., Recalde, J. J., Bernstein, D. J., & Freeman, C. W. (2009). Raster-based analysis of coastal terrain dynamics from multitemporal lidar data. *Journal of Coastal Research*, 25(2), 507–514.
- Muir, B. (2019, November 2). Wind whips northern New York, 20-foot waves reported on Lake Ontario, power out for thousands. *NNY360*. Retrieved from https://www.nny360.com/news/jeffersoncounty/wind-whips-northern-new-york-20-foot-waves-reported-on-lake-ontario-power-out-for/article_4470b5bc-fca0-11e9-98e3-a31de213df43.html#tncms-source=login
- Nagarajan, S., Khamaru, S., & De Witt, P. (2019). UAS based 3D shoreline change detection of Jupiter Inlet Lighthouse ONA after Hurricane Irma. *International Journal of Remote Sensing*, 40(24), 9140–9158.
- NOAA. (2021a). Station Home Page - NOAA Tides & Currents. Retrieved April 27, 2020, from <https://tidesandcurrents.noaa.gov/stationhome.html?id=9052030>
- NOAA. (2021b). Station 45135 – Prince Edward Pt - National Data Buoy Center of Excellence in Marine Technology. Retrieved from https://www.ndbc.noaa.gov/station_page.php?station=45135
- NOAA. (2021c). Data Access Viewer. Retrieved from <https://coast.noaa.gov/dataviewer/#/lidar/search/>
- NYS DEC. (2020). Natural Heritage Areas Program - NYS Dept. of Environmental Conservation. Retrieved April 27, 2020, from <https://www.dec.ny.gov/animals/36987.html>
- NYS OTIS. (2019). *New York State Airborne LiDAR Processing and Accuracy Report*. NYS Office of Information Technology Services.
- Reinson, G. E. (1992). Transgressive Barrier Island and Estuarine Systems. In *Facies Models: Response to Sea Level Change* (pp. 179–194). Canada: Geological Association of Canada.
- Ritter, D. F., Kochel, R. C., & Miller, J. R. (1978). *Process Geomorphology* (3rd ed.). Boston: McGraw-Hill.
- Shervais, K., & Dietrich, J. (2016). Structure from Motion (SfM) photogrammetry data exploration and processing manual. UNAVCO.
- Sherwood, C. R., Warrick, J. A., Hill, A. D., Ritchie, A. C., Andrews, B. D., & Plant, N. G. (2018). Rapid, remote assessment of Hurricane Matthew impacts using four-dimensional Structure-from-Motion photogrammetry. *Journal of Coastal Research*, 34(6), 1303–1316. <https://doi.org/10.2112/JCOASTRES-D-18-00016.1>
- Sherwood, C. R. (2021, January 15). questions about drone imagery processing.
- SPCMA. (2022). The Sandy Pond Channel Maintenance Association [Homestead]. Retrieved August 30, 2022, from <http://spcma.homestead.com/?fbclid=IwAR1TGVTOLkPuFczom9vtVFHqZRBdEu6Sf0FqVHMmNUTngjSG6-F5dYxBXfE>

- Stockdon, H. F., Doran, K. S., & Sallenger Jr., A. H. (2009). Extraction of lidar-based dune-crest elevations for use in examining vulnerability of beaches to inundation during hurricanes. *Journal of Coastal Research*, 53, 59–65. <https://doi.org/10.2112/SI53-007.1>
- Sutton, R., Lewis, T., & Woodrow, D. (1972). Post- Iroquois Lake stages and shoreline sedimentation in eastern Ontario basin. *Journal of Geology*, 80(3), 346–356.
- Thom, B. G., & Hall, W. (1991). Behaviour of beach profiles during accretion and erosion dominated periods. *Earth Surface Processes and Landforms*, 16(2), 113–127. <https://doi.org/10.1002/esp.3290160203>
- Weir, G. (1977). Inlet formation and washover processes at North Pond, eastern Lake Ontario. *ELOSD- Geology and Sand Transport*. Retrieved from <https://seagrant.sunysb.edu/elodune/Education/EDU%20PDF/Resources/Inlet%20formation%20and%20washover%20processes%20at%20north%20pond.pdf>
- Westoby, M. J., Brasington, J., Glasser, N. F., Hambrey, M. . J., & Reynolds, J. M. (2012). “Structure-from-Motion” photogrammetry: A low-cost, effective tool for geoscience applications. *Geomorphology*, 179, 300–314. <http://dx.doi.org/10.1016/j.geomorph.2012.08.021>
- Wheaton, J. M., Brasington, J., Darby, S. E., & Sear, D. A. (2010). Accounting for uncertainty in DEMs from repeat topographic surveys: improved sediment budgets. *Earth Surface Processes and Landforms*, 35, 136–156. <https://doi.org/10.1002/esp.1886>
- Williams, R. D. (2012). DEMs of Difference. In *Geomorphological Techniques*. London, UK: British Society for Geomorphology.
- Woodrow, D., McClennen, C., & Ahrnsbrak, W. (2002). *Eastern Lake Ontario Sand Transport Study (ELOSTS): Final Report on Sediment Transport Patterns and Management Implications for Eastern Lake Ontario* (Technical Appendix). The Nature Conservancy.
- Woolard, J. W., & Colby, J. D. (2002). Spatial characterization, resolution, and volumetric change of coastal dunes using airborne LiDAR: Cape Hatteras, North Carolina. *Geomorphology*, 48, 269–287. [https://doi.org/10.1016/S0169-555X\(02\)00185-X](https://doi.org/10.1016/S0169-555X(02)00185-X)
- Zainescu, F. I., Vespremeanu-Stroe, A., & Tatui, F. (2019). The formation and closure of the Big Breach of Sacalin spit associated with extreme shoreline retreat and shoreface erosion. *Earth Surface Processes and Landforms*, 44, 2268–2284.
- Zhang, K., Whitman, D., Leatherman, S., & Robertson, W. (2005). Quantification of beach changes caused by Hurricane Floyd along Florida’s Atlantic Coast using airborne laser surveys. *Journal of Coastal Research*, 21(1), 123